EFFECT OF FREE-STREAM TURBULENCE ON TURBULENT BOUNDARY LAYERS

by

Jiho You

A dissertation submitted to The Johns Hopkins University in conformity with the requirements for the degree of Doctor of Philosophy.

Baltimore, Maryland

June, 2020

Abstract

Direct numerical simulations (DNS) are performed to study turbulent boundary layers beneath quiescent and vortical free streams. The inflow boundary layer is computed in a precursor simulation of laminar-to-turbulence transition, and the free-stream vortical forcing is obtained from DNS of homogeneous isotropic turbulence. When free-stream turbulence buffets a zero-pressure-gradient turbulent boundary layers, the skin friction coefficient is elevated relative to its value in the canonical flow configuration. The change can be explained in terms of an increase in the power input into the production of boundary-layer turbulence kinetic energy. This increase takes place deeper than the extent of penetration of the external perturbations towards the wall, and also despite the free-stream disturbances being void of any Reynolds shear stress. Conditional statistics demonstrate that the free-stream turbulence has two effects on the boundary layer: one direct and the other indirect. The low-frequency components of the free-stream turbulence penetrate the log layer. The associated wall-normal Reynolds stress acts against the mean shear to enhance the shear stress, which in turn increases turbulence production. This effect directly enlarges the scale

and enhances the energy of outer large-scale motions in the boundary layer. The second indirect effect is the influence of these newly formed large-scale structures. They modulate the near-wall shear stress and, as a result, increase the turbulence kinetic energy production in the buffer layer, which is deeper than the extent of penetration of free-stream turbulence towards the wall. Due to the enhanced Reynolds stresses by the free-stream forcing, the wall-normal heat flux is also increased, which has the dual effect of distorting the base temperature profile and enhancing the production of scalar variance; both contribute to the increase in the wall heat-transfer rate. These changes are accompanied by modification of the spectra of the thermal field in the outer region of the boundary layer, where large-scale thermal structures are formed in response to the large-scale velocity motions. In the near-wall region, the outer hydrodynamic field modulates and then strengthens not only the hydrodynamic but also thermal structures relative to the unforced flow. The configuration of the forced boundary layer on the concave curve introduces additional complications because the fluid is subjected to a centrifugal instability as well as streamwise pressure gradients. Absent free-stream disturbances, adverse pressure gradient near the onset of curvature leads to sharp decrease in skin friction, by more than 70% its initial value, and intermittent separation. Over the curve, the spanwise and wall-normal Reynolds stresses intensify and the radial distance between their peaks increases, which is indicative of growing Görtler vortex structures. The forced boundary layer is buffeted by free-stream turbulence with 10% intensity. The change in boundary-layer thickness

modifies the apparent curvature, and its near-wall distortion reduces the probability of separation. The forcing also enlarges and strengthens the Görtler vortices: The peak spanwise and wall-normal Reynolds stresses part farther, the associated shear-stress correlation increases and so does the streamwise stress. Sustained by centrifugal effects and intensified by free-stream turbulence, these large-scale structures directly influence the near-wall region: Free-stream fluid is 'seen' more often deep within the buffer layer, and large-scale, outer-flow motions strongly correlate with near-wall disturbances. Intense, persistent roll motions above the curved wall thus directly send the free-stream turbulence towards the buffer layer. Such mechanism will diminish under weaker curvature, which is consistent with flat-plate boundary layers.

Acknowledgments

First and foremost, I would like to appreciate my advisor Prof. Tamer A. Zaki, for guiding me through my studies and sharing his knowledge and experiences in fluid mechanics, numerical simulations, and many other things in life. And, I owe a debt of gratitude to Chonghwan Lee, the president of the Kwanjeong Educational Foundation, for a scholarship. I would like to acknowledge Dr. Seo Yoon Jung for providing the inflow turbulent boundary-layer data and Dr. Jin Lee for his guidance during the early stages of my research. Dr. David Buchta is also gratefully acknowledged for collaborating for my final manuscript as the coauthor. And, I would like to thank labmates who have helped along the way: Dr. Sang Jin Lee, Dr. Junho Park, Dr. Reza Jahanbakhshi, Dr. Amir Esteghamatian, Qi wang, Mengze Wang, and all the others. I have been very fortunate to work with these gifted persons.

I am also grateful to my parents and brother. I would never have made it this far without their encouragement. And, finally, I thank my wife, who was always there to congratulate, to encourage, and to motivate me. My sincerest thanks to you all.

Contents

List of Tables

List of Figures

Chapter 1

Introduction

1.1 Motivation

A boundary layer is a thin layer above the solid surface where the effect of fluid viscosity is significant. Close to the leading edge, the flow is entirely laminar, and the streamwise velocity changes uniformly with wall-normal direction. Further downstream, the laminar flow becomes unstable, and the streamwise velocity is characterized by unsteady swirling motions inside the boundary layer. This type of flow is known as *turbulent boundary layer* (TBL). Turbulent boundary layers have been extensively studied to address the dynamics of the numerous flow configuration: the efficiency of bird flight, the performance of a wind turbine, the flow around a turbomachinery blade, and the lift and drag of the submarine or aircraft.

Even though turbulence is confined to the near wall-region in most boundary-

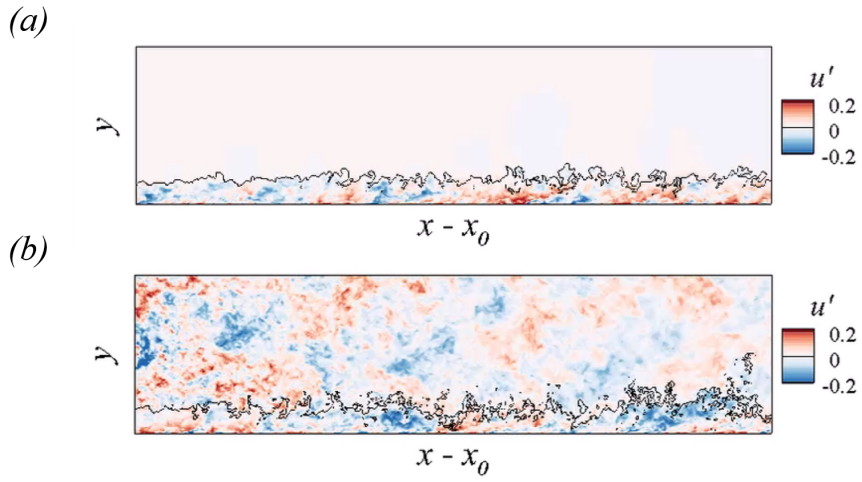

Figure 1.1: Side view of streamwise-velocity fluctuation in turbulent boundary layers beneath (a) quiescent and (b) turbulent free stream. Black line indicates the interface based on level set function (See §3.3 for details).

layer studies [1, 27, 36, 44, 57], the free stream is not often quiescent in the above examples. For instance, in industrial flows such as those in turbomachinery and wind turbine, inflow streams often contain turbulent eddies generated by upstream structures. When the free-stream disturbance is strong, it can actively interact with the underlying boundary layers (figure 1.1). It is established that the external forcing leads to an increase in drag and heat-transfer rate [11, 28, 50, 78, 80]. However, the internal mechanism of the increase has remained relatively unexplored because the forced boundary layer is a complex dynamical system. The dissertation examines the interaction of the free-stream turbulence (FST) with a zero-pressure gradient TBL using direct numerical simulations.

And, the forced boundary layer often develops over curved, complicated surfaces, in engineering flows. This configuration introduces additional complications because

the fluid is subjected to centrifugal instability as well as streamwise pressure gradients. Owing to the complicated flow phenomena, the effect of the external disturbances on the curved-wall boundary layer has hardly studied. Thus, the thesis also investigates the combined effect of the concave curvature and FST on the boundary layer.

1.2 Wall-bounded turbulent flows

The canonical turbulent boundary layers have the boundaries between turbulent and non-turbulent regions. The turbulent boundary layers are characterized as highly anisotropic flows due to the mean shear near the wall. Turbulent structures inside this wall-bounded turbulent flow have coherent patterns.

Hama et al. [27] observed elongated streaky structures in the near-wall region of TBL. Notably, the near-wall structures are associated with 'sweeps' and 'ejections' that were considered the primary source of turbulence production. Wallace et al. [84] carried out a quadrant analysis and showed that ejections and sweeps play an active role in enhancing turbulence, which also feeds back into the governing equation for the mean flow and thus influences the mean-shear profile.

In a recent decade, many researchers have focussed on the outer region, which is populated by large-scale structures. The large-scale motions have been believed to be created by the vortex packets, which are consist of multiple hairpin structures [44]. The hairpin vortices within the packet align in the streamwise direction and

induce regions of low-streamwise momentum between their legs [1, 36]. The energetic footprint of the large-scale motions is evident as large-wavelength peaks in the pre-multiplied energy spectra of the streamwise velocity fluctuations, which have a streamwise extent of approximately 6δ [35, 44]. To clearly see the emergence of the outer peak, the friction Reynolds number, Re_τ should be higher than 2000 [35].

Hutchins and Marusic [35] and Mathis et al. [57] examined the interaction between the large and small scales in boundary layers. They showed that the large-scale motions in the logarithmic and outer layer have a strong influence on the behavior of the near-wall turbulence. Mathis et al. [57] demonstrated that the hairpin packets are attached to the wall, and the motions likely have a crucial role in modulating the near-wall cycles.

1.3 Turbulent boundary layers exposed to external disturbances

Then, what happens when external disturbances buffet the turbulent boundary layer? In this case, the common trends for the canonical boundary layers are not observed. For instance, the wall-shear stress and heat-transfer rate are enhanced, but the boundary-layer thickness increases. The external forcing can be classified based on whether it has a mean shear (*e.g.*, wakes) or not (*e.g.*, homogeneous isotropic turbulence).

When the wake is above the boundary layer, the underlying flow will be significantly affected because of the velocity deficit associated with the wake profile. Previous works have mainly focussed on the effect of wakes on laminar boundary layers, notably their transition to turbulence [56, 85, 86]. They showed that hairpin structures resulting from the wake appreciably alter dynamics inside a boundary layer and thus trigger the transition.

Even without the added complication of mean-flow unsteadiness, the homogeneous isotropic turbulence (HIT) in the free stream significantly influence the boundary layer. The FST has been often characterized as the turbulent intensity relative to the free-stream velocity and outer lengthscales, such as dissipation lengthscale. Earlier works have experimentally studied the effect of grid-generated HIT in the wind tunnel and tried to find correlations between the change of drag and heat-transfer rate and the FST properties [11, 15, 28, 29]. Particularly, when the boundary-layer thickness and the outer lengthscale of the FST are comparable to one another, their interaction significantly alters the mean profile and hence increases the drag and heat-transfer rate [11, 28].

The turbulent intensity of the studies based on the grid-generated HIT was mostly less than 7%. Later a series of studies have been subsequently carried out to investigate the high-intensity FST, mostly higher than 10%, using gas turbine combustors [2] and high-velocity cross jets [55, 80, 81]. These high levels of forcing led to an even more substantial increase in skin friction and heat-transfer rate compared to

grid-generated HIT. Thole and Bogard [81] provided evidence that the strong FST penetrates the boundary layer very close to the wall using the spectral analysis.

The large-scale coherent motions induced by FST have a clear signature in the pre-multiplied energy spectra. The two distinct peaks have been observed when the large-scale FST buffets the boundary layer [20, 50, 77] despite the low Reynolds number relative to that of the canonical boundary layer required to see the peak separation. Particularly, Dogan et al. [20] decomposed the lengthscales of FST and showed that the large-scale signal deeply penetrates and modulates the near-wall region.

1.4 Turbulent boundary layers over curved surfaces

Besides the external forcing, the curved surface significantly affects the turbulent structures as well as the flow statistics inside the boundary layer. And, the curvature effect is of considerable engineering interest since the boundary layer mostly develops on the curved wall in the realistic flow fields.

A curved-wall boundary layer is subjected to an extra rate of strain [13, 33, 58] in addition to a simple shear, velocity gradient in the wall-normal direction. The additional rate of strain is associated with the curvature of the mean streamlines, which is equal to $-U/r$ where U and r are the streamwise velocity and the streamline

radius of curvature, respectively. The radius is positive for convex and negative for concave flows. Thus, the streamline curve produces surprisingly significant changes in the turbulence structures of shear layers. The curvature effect is characterized as the ratio of the boundary-layer thickness and the radius of the curved wall: mild ($\delta/R < 0.01$), moderate ($\delta/R \sim 0.1$) and strong curvature ($\delta/R \sim 1$) [67].

The effects of convex and concave curvatures are opposite to one another. Patel [66] pointed out the similarity between the flow on the curve and that subjected to pressure gradient: the effect of convex curvature is similar to that of an adverse pressure gradient while that of concave curve resembles the impact of a favorable pressure gradient.

On the convex curvature, the flow becomes stable, and turbulence is damped [25, 58, 79]. In this case, the dissipation rate increases, and thus the turbulent kinetic energy and the shear stress all decrease. When the turbulence is suppressed, there is less mean momentum transport from the outer region to the wall. Due to the uncoupling between inner and outer layers, stress-producing motions are damped in the inner layer. Consequently, the convex curvature attenuates the existing turbulent structures in the outer region.

On the contrary, the concave curvature destabilizes the flow and thus enhances the turbulence [5, 6, 33]. In addition to the modification of flow statistics, the concave curvature may significantly alter the turbulent structure. It is well-known that Görtler vortices arise in the laminar boundary layer on the concave curvature if the boundary-

layer thickness is comparable to the radius of curvature. The development of these vortices, caused by centrifugal instability results in the significant spanwise variations. However, these structures have not been relatively well defined in the turbulent flow. Patel and Sotiropoulos [67] questioned the emergence of the longitudinal streamwise vortices in turbulent boundary layers on the concave wall since the structures are distributed randomly in space and time, which makes the existence of Görtler vortices undefined. Hoffmann et al. [33] and Barlow and Johnston [6] deliberately locked the pattern of large-scale roll cells using vortex generators and showed that upwash enhances the turbulence.

1.5 Objective

Previous works have tried to quantify the increase in drag and heat-transfer rate when the flat-plate boundary layer is exposed to FST, and how its intensity and lengthscale are related to the rise. But the internal mechanism that leads to the enhancement of the skin friction and heat-transfer rate is undefined. Even though numerical simulations may be able to provide a more precise analysis and novel techniques to explore the mechanism, there are few studies [50, 68] due to the difficulty of the simulation setup. Since the system becomes more complicated to additionally consider the curvature effect, the influence of FST on the curved-wall boundary layer has been less studied even in the experimental works [43].

Thus, the purpose of this study is to elucidate mechanisms of how the free-stream forcing statistically and dynamically influences the boundary layers not only over the flat plate but also the curved surface. By comparing the cases of the canonical turbulent boundary layer and the flow forced by external disturbance, this study sheds light on each influence of FST and concave curvature on turbulent boundary layers and their combined effects.

This dissertation is organized in 6 chapters, as follows. The first chapter describes the background and objective of the current study. Chapter 2 presents the numerical method of direct numerical simulation (DNS) and generating inflow conditions. Chapter 3 demonstrates the effect of FST on the turbulent boundary layer on the flat plate in terms of the increase in skin friction. In this chapter, a level set approach is employed for conditional sampling, measuring the FST contribution to the overall statistics. Chapter 4 focuses on the heat-transfer enhancement induced by FST. Chapter 5 addresses the effect of FST on TBL over concave curvature. Finally, the conclusion of this study is presented in the last chapter.

Chapter 2

Numerical details

2.1 Direct numerical simulations

The continuity and Navier-Stokes equations for incompressible flow are

$$\frac{\partial u_j}{\partial x_j} = 0 \tag{2.1}$$

$$\frac{\partial u_i}{\partial t} + \frac{\partial u_i u_j}{\partial x_j} = -\frac{\partial p}{\partial x_i} + \frac{1}{Re_{\theta_{in}}} \frac{\partial^2 u_i}{\partial x_j^2}. \tag{2.2}$$

Terms are non-dimensionalized using the free-stream velocity U^*_∞ and the inlet momentum thickness θ^*_{in}, where star indicates dimensional quantities. The momentum thickness Reynolds number in equation (2.2) is defined as $Re_{\theta_{in}} \equiv U^*_\infty \theta^*_{in}/\nu^* = 1200$, where ν^* is the kinematic viscosity. The velocity components in the streamwise (x), wall-normal (y) and spanwise (z) directions are u, v and w, respectively, and the pressure is p. Hereafter, bar refers to a spanwise and time average, and the prime

indicates fluctuating quantities according to Reynolds' decomposition, for example $u = \overline{u} + u'$.

The flow equations were solved using a fractional step algorithm on a staggered grid with a local volume-flux formulation [72]. The viscous terms were integrated in time implicitly using the Crank-Nicolson method, and the convective terms were treated explicitly using the Adams-Bashforth scheme. When the domain configuration is a flat plate (§3 and §4), the pressure equation is solved by performing Fourier transform in the span, cosine transform in the streamwise direction and a tridiagonal direct solve in the wall-normal coordinate. The algorithm has been used extensively in previous studies of transitional [62] and fully turbulent wall-bounded flows [39, 49]. In the curved-wall case (§5), a multigrid method is adopted for solving the pressure equation.

In DNS of turbulent thermal boundary layers, the temperature has been considered as a passive scalar advected by fluid motion. Then, the governing equation for the temperature is the energy equation, shown below:

$$\frac{\partial T}{\partial t} + u_j \frac{\partial T}{\partial x_j} = \frac{1}{Pe} \frac{\partial^2 T}{\partial x_j \partial x_j}. \tag{2.3}$$

The Péclet number is the product of the Reynolds and Prandtl numbers, $Pe \equiv Re_{\theta_{in}} Pr$, where $Pr \equiv \nu^*/\alpha^* = 0.7$ and α^* is the thermal diffusivity. The non-dimensional temperature is defined as $T \equiv (T^*_\infty - T^*) / (T^*_\infty - T^*_w)$, where subscripts w and ∞ denote values at the wall and in the free stream, respectively. The non-dimensional temperature is therefore unity at the wall $T_w = 1$ and vanishes in the free

stream $T_\infty = 0$; and the non-dimensional temperature deficit is $\Theta \equiv (T^* - T_w^*)/(T_\infty^* - T_w^*) = 1 - T$.

For this energy equation, similar temporal discretization as adopted for the Navier-Stokes equations was employed; the spatial discretization was also similar, except for the advection term which was discretized using a fifth-order upstream central scheme [63] in order to resolve the sharp gradients in temperature. The algorithm has been used extensively in previous studies of thermal boundary layers [47, 48].

2.2 Generating inflow conditions

2.2.1 Inflow turbulent boundary layer

In order to generate a realistic inflow turbulent boundary layer for the main computations, a precursor simulation of a transitional boundary layer was performed. A spatially and temporally resolved cross-flow plane was stored in the fully turbulent regime and used as inflow in the main simulation. A similar approach was adopted by Lee et al. [47] and Lee et al. [49]. The inflow condition in the auxiliary transitional computation is a Blasius boundary layer and a superposition of vortical perturbations which were prescribed inside the mean shear only, such that the transitional boundary layer develops below a quiescent free stream (in contrast of bypass transition). The domain length spanned $106 < Re_\theta < 1500$ which overlaps with the main simulation domain. Instantaneous TBL data were extracted in the precursor simulation at

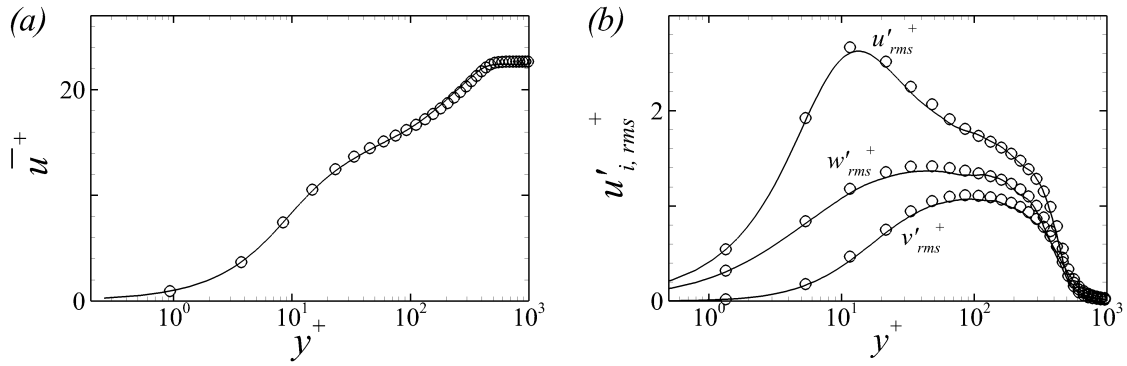

Figure 2.1: Validation of inflow turbulent boundary layer. (a) Mean streamwise velocity and (b) root-mean-square fluctuations in inner scaling; (—) inflow TBL in main simulation and (◯) data by Schlatter and Örlü [74] at $Re_\theta = 1410$.

$Re_\theta = 1200$. The time series was subsequently applied at the inlet in the main simulation. Even though the inflow Reynolds number is lower than the recommendation by Schlatter and Örlü [75], the streamwise extent of the domain ensures that their criterion is satisfied where results are examined. In addition, the accuracy of this inflow condition was extensively validated. Figure 2.1 compares the mean streamwise velocity profile and velocity fluctuations in inner scaling with the data from Schlatter and Örlü [74]. The mean streamwise velocity $\overline{u}$ and the root-mean-square fluctuations $u'_{i,rms}$ are scaled by the friction velocity $u_\tau \equiv \sqrt{\nu \frac{\partial \overline{u}}{\partial y}|_{y=0}}$ where $y^+ \equiv \frac{y u_\tau}{\nu}$.

2.2.2 Inflow free-stream turbulence

In addition to the inflow boundary layer, free-stream vortical perturbations are needed at the inlet. Decaying, homogeneous isotropic turbulence (HIT) was simulated in a rectangular box with dimensions $\{L_x, L_y, L_z\}_{HIT} = \{80, 80, 160\}\,\theta_{in}$ using a

pseudo-spectral algorithm, with periodic boundary conditions in all three coordinate directions. Both x and y were discretized using 640 Fourier modes, and 1280 modes were used in the spanwise direction. Figure 2.2 shows the time history of the turbulent intensity, skewness of the velocity derivative, integral length scale and Taylor microscale,

$$Tu \equiv \sqrt{\frac{u'^2 + v'^2 + w'^2}{3}}, \quad S'(u') \equiv \frac{\overline{(\partial u'/\partial t)^3}}{\left(\overline{(\partial u'/\partial t)^2}\right)^{3/2}}, \quad L_k \equiv \frac{k^{3/2}}{\epsilon}, \quad \lambda \equiv \sqrt{\frac{15\nu\overline{u'^2}}{\epsilon}}.$$

In the above expressions, k is the turbulence kinetic energy and ϵ is the dissipation rate. The time instant when the data is extracted is identified by a dashed-dot line in the figure ($Tu = 0.1$ and $L_k \approx 10.8\theta_{in}$). Note that S' is approaching its asymptotic value [7]. At the time when the data are extracted, the Reynolds number based on the Taylor microscale is $Re_\lambda \equiv u'_{rms}\lambda/\nu = 105$.

The turbulence intensity follows the decay law $Tu \propto t^{-5/7}$, and the lengthscale shows a consistent power-law dependence $L_k \propto t^{2/7}$. The grid turbulence in this thesis is of the Batchelor type since it satisfies $Tu^2 L_k^5 \approx$ constant (as opposed to Saffman turbulence which satisfies $Tu^2 L_k^3 \approx$ constant [38]). In experiments [e.g. 8], the decay of turbulence downstream of the grid can be described by

$$Tu \propto \left(\frac{x - x_g}{M}\right)^{b/2}$$

where $x - x_g$ is the distance from the virtual origin of the screen and M is the mesh width. Using Taylor hypothesis, the decay can then be related to the power-law behaviour in our temporal simulations, $Tu \propto t^{-5/7}$, and hence $b = -10/7 \approx -1.43$.

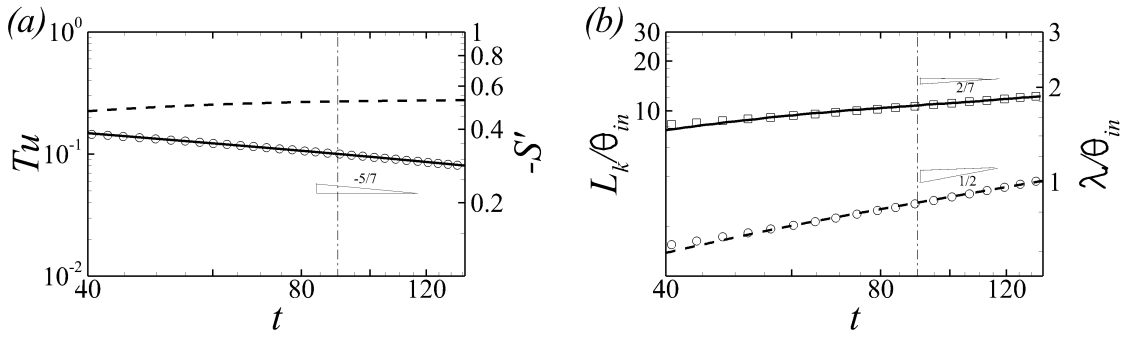

Figure 2.2: Evolution of homogeneous isotropic turbulence in time. The dashed-dotted line marks the time instant when data are extracted to apply as inflow condition in the main simulation. (a) (—) Tu, (◯) $Tu \propto t^{-5/7}$ and (- - -) $-S'$; (b) (—) L_k, (□) $L_k \propto t^{2/7}$, (- - -) λ and (∘) $\lambda \propto t^{0.5}$

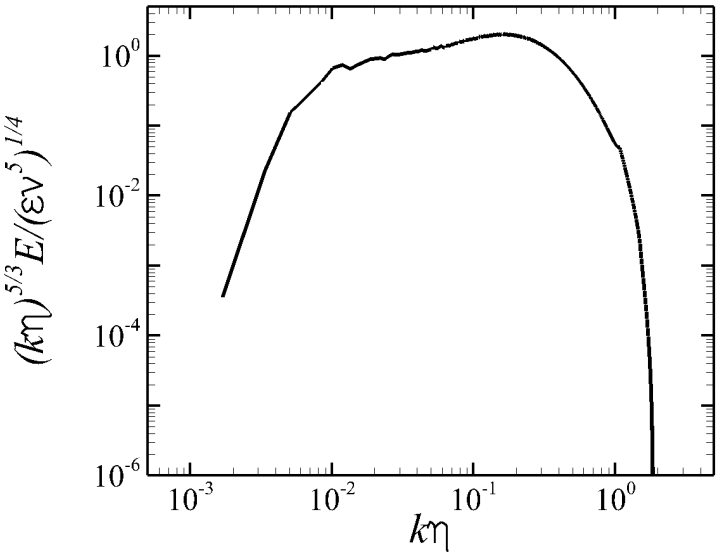

Figure 2.3: Three-dimensional energy spectra of the inflow HIT.

This value is consistent with the experimental results by Kurian and Fransson [46], where $-1.6 < b < -1.2$.

The three-dimensional energy spectra for the inflow FST is provided in figure 2.3.

The height of the plateau in $E(\kappa\eta)$, or the Kolmogorov constant C_k, is approximately 1.96. The spatial resolution of a spectral simulation is adequate since $\kappa_{max}\eta > 1$, where κ_{max} is the maximum wavenumber and η is the Kolmogorov scale.

The free-stream disturbances at the inflow of the main simulations are extracted from the HIT data using Taylor's hypothesis, where space is converted to time using the free-stream velocity of the boundary layer, (U_∞, V_∞) at $Re_{\theta,in} = 1200$.

The generated TBL and FST were introduced at the inlet in the main simulations of §3, §4 and §5. Note that periodicity of the free-stream forcing is not a concern because the underlying boundary layer is time dependent and not periodic. We have also exploited isotropy of the free stream and rotated the HIT volume about its z-axis by $\xi = 7.829°$. In this manner, every $L_{x,HIT}/\left(U_\infty \cos\xi\right)$ time units, the HIT plane prescribed as inflow to the DNS is shifted vertically by $L_{x,HIT}\tan\left(\xi\right) = 11\theta_{in}$, which is of the same order as the integral lengthscale. Thus, the unsteady interaction between TBL and FST makes the flow configuration more realistic.

Chapter 3

Turbulent boundary layer buffeted by free-stream disturbances over flat plate

3.1 Introduction

In numerous applications, turbulent boundary layers (TBL) are exposed to, and interact with free-stream vortical perturbations. For example, in industrial flows such as turbomachinery and heat exchangers, the incoming stream can include free-stream perturbations that buffet the turbulent boundary layer developing on the wall. The present work examines this interaction using direct numerical simulations. A zero-pressure-gradient TBL is simulated beneath quiescent and vortical free streams, and

the two conditions are contrasted.

Earlier studies have experimentally investigated the effect of grid-generated free-stream turbulence (FST) with intensities mostly less than 7% [15, 28, 29, 78]. These studies showed that FST mainly influences the wake region of the mean-velocity profile. The FST depresses the wake region, or reduces U_∞/u_τ, where U_∞ and u_τ are the free-stream and friction velocities, respectively. Simonich and Bradshaw [78] reported that the increase in skin friction and heat transfer are nearly proportional to the turbulent intensity only. In their study, skin friction and heat transfer increased by 2% and 5%, respectively, for 1% increase in the free-stream turbulence intensity. Hancock and Bradshaw [28] tried to capture the effects of FST with a single parameter $\beta = \frac{Tu/U_\infty}{(L_u/\delta)+2}$ where Tu, L_u and δ are the turbulence intensity and dissipation length scale and the boundary-layer thickness; the mean skin friction was shown to increase with the parameter β. Blair [11] and Castro [15] suggested a modification to the parameter in order to take account the low-Reynolds-number effect ($Re_\theta < 2000$) whereby the FST becomes less effective at increasing drag.

Hancock and Bradshaw [29] performed conditional sampling to investigate the contribution of FST to flow statistics. In their study, the boundary-layer fluid was thermally identified by heating the plate. They reported the conditional contributions of the free-stream and boundary-layer fluids to the Reynolds-stress profiles and triple products. In their study, the conditional perturbation statistics were evaluated relative to the conventional time average (or unconditional) mean. They showed that

shear-stress correlation coefficient ($-\overline{u'v'}/u'_{rms}v'_{rms}$) is reduced because the isotropic FST effectively destroys the coherence of the perturbations inside the boundary layer.

Further studies were performed with high turbulence intensities, greater than 10%, generated by gas turbine combustors [2] or high-velocity cross jets [80, 81]. Ames and Moffat [2] proposed a new parameter which considers the momentum-thickness Reynolds number, Re_θ, in addition to L_u and Tu for predicting skin-friction enhancement. But Thole and Bogard [80] demonstrated that the increase in skin friction with the Hancock parameter, β, is sufficiently accurate up to $Tu = 28\%$. Based on simulations of forced temporal boundary layers, Kozul et al. [45] reported that another relevant parameter is the ratio of eddy-turnover timescales of the free-stream turbulence and boundary layer. Too small a value leads to weak interactions since the external turbulence decays quickly and cannot influence of the boundary layer. Thole and Bogard [81] found that even the highest levels of FST considered mostly influence the outer region of the boundary layer, and have negligible effects on the logarithmic region. However, they provided evidence that the strong FST penetrates into the boundary layer very close to the wall, by performing hot-wire measurements of the streamwise velocity fluctuations: The energy spectra of the near-wall region was similar to that of the free-stream turbulence. While the above studies examined the influence of FST on TBL experimentally, Péneau et al. [68] performed large-eddy simulations (LES) to examine the effect of strong FST up to $Tu = 21\%$. They used random Oseen vortices for generating inflow FST, which was

therefore neither homogeneous nor isotropic. They reported that the increase in skin friction is almost unchanged irrespective of the FST intensity for $7\% < Tu < 21\%$, but their domain size was too short ($Re_\theta \approx$ 1200-1500) to observe the interactions between FST and TBL at higher Reynolds number.

The influence of the free-stream turbulence lengthscale on the changes within the boundary layer can be gleaned by contrasting results from different studies. Sharp et al. [77] examined the effect of large-scale FST, and showed that the Reynolds stresses normalized by the friction velocity increase relative to their values in canonical boundary layers. They also reported the emergence of an outer peak in the pre-multiplied energy spectra when the boundary layer is subjected to the free-stream turbulence. Such peak is known to occur in unforced boundary layers, although at appreciably higher Reynolds numbers Hutchins and Marusic [35], and is associated with large-scale motions that reach many boundary-layer thicknesses in streamwise extent and modulate the near-wall structures [37, 57]. In contrast to the work by Sharp et al. [77], Nagata et al. [60] considered small-scale FST ($L_u/\delta \ll 1$) with relatively low turbulent intensity ($Tu < 2.4\%$). They demonstrated that the skin friction still increases, even though the rate of production of turbulence kinetic energy is reduced along with the Reynolds normal and shear stresses, normalized by the friction velocity. In addition, the outer peak in the pre-multiplied energy spectra was not observed in the experiments by Nagata et al. [60]. These results are unique since most other efforts have focused on larger free-stream turbulence lengthscales.

The outer peak in the energy spectra was also reported by Li et al. [50] who performed large-eddy simulations of boundary layers beneath free-stream turbulence at Reynolds numbers in the range $Re_\theta \approx$ 100-1000. Their result is curious because their boundary layer was initially transitional and had not reached an equilibrium state. Recently, Dogan et al. [20] experimentally evaluated the effect of large-scale FST on the near-wall region. They reported an increase in the near-wall streamwise velocity fluctuations with FST intensity. Using a scale-decomposition, they separated the small- and large-scale contributions, and attributed the increase to the latter. Dogan et al. [21] showed a close correlation between the large-scale velocity signals in the buffer and log layers by performing multipoint measurements. Subsequently, Hearst et al. [31] identified within the spectrogram zones that are affected by the free-stream spectrum and a universal small-scale inner peak. Since the later was unchanged by the forcing, they concluded that only the large-scale components of the free-stream turbulence penetrate down to the near-wall region.

Previous experiments and simulations have quantified the increase in drag when boundary layers are exposed to free-stream forcing, and how this effect depends on the intensity and lengthscale of free-stream turbulence. The exact mechanism that leads to the increase in skin friction is, however, less clear. The objective of the current study is to investigate how the free-stream fluid statistically and dynamically causes this increase. Therefore, an important consideration is to objectively distinguish the free-stream fluid and its contribution to flow statistics — a requirement that is difficult

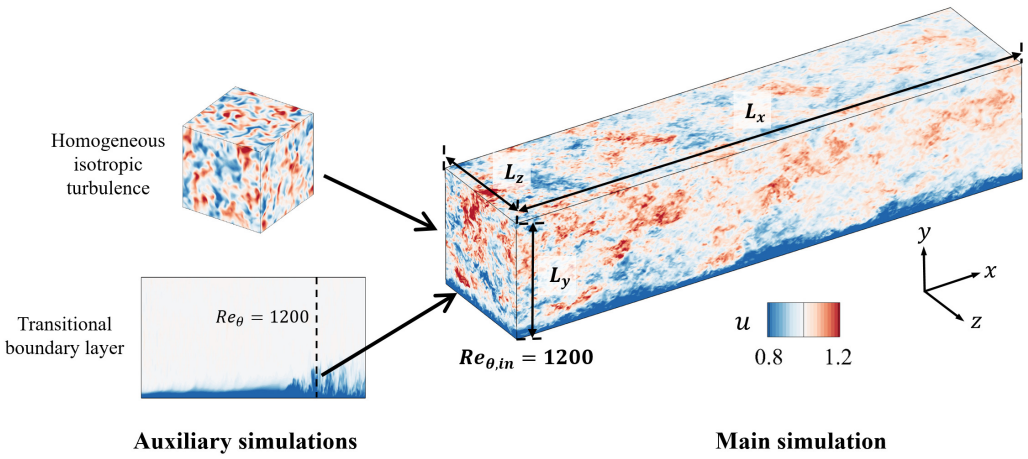

Figure 3.1: Schematic of the flow configuration showing the precursor transitional boundary layer and homogeneous isotropic turbulence, and the fully turbulent flow downstream.

to achieve experimentally and that has not been performed numerically to date. We adopted a similar method to the work by Hancock and Bradshaw [29]. They heated the boundary-layer fluid, although the finite Prandtl number, Pr, in the experiments reduces the accuracy of separating the two streams. In our simulations, we have the advantage that we employ a level set approach which represents an infinite Pr and thus maintains a sharp virtual interface between the boundary-layer and free-stream fluids. Using conditional sampling, we examine how the FST modifies the boundary layer statistics and flow structures, and leads to drag increase.

Two main simulations are performed, the first of a canonical turbulent boundary layer and the second additionally includes HIT with 10% intensity in the free stream. Comparing the downstream evolutions of the two flows highlights the impact of the newly introduced free-stream forcing on the boundary layer. The configuration thus

differs from experiments where both the boundary layer and free-stream turbulence evolve together from the leading edge. The domain lengths ensure that the momentum thickness Reynolds numbers exceeds $Re_\theta = 3000$ before the exit plane, and hence our simulations go beyond the Reynolds numbers in previous numerical studies.

The chapter is organized into seven sections. A description of the numerical method and the inflow condition is provided in Section 2. Section 3 includes the conditional sampling approach, and a quantitative comparison of conditional statistics based on the level set and the vorticity magnitude for conventional boundary layer. Section 4 demonstrates the influence of FST on the skin friction and reports the conditional statistics of the forced flow. Section 5 discusses the effect of FST on the turbulent flow structures. Section 6 examines the effect of smaller lengthscale FST, and conclusions are summarized in the last section.

3.2 Simulation details

3.2.1 Computational setup

A schematic of the flow configuration is shown in figure 3.1. The dimensions of the computational domains, the number of grid points and resolutions are provided in table 3.1. At the entrance, realistic inflow TBL and FST are introduced (§2.2). The generated inflow FST has the turbulent intensity $Tu = 0.1$ and integral length scale $L_k \approx 10.8\theta_{in}$. Two simulations are contrasted: one of a conventional turbulent

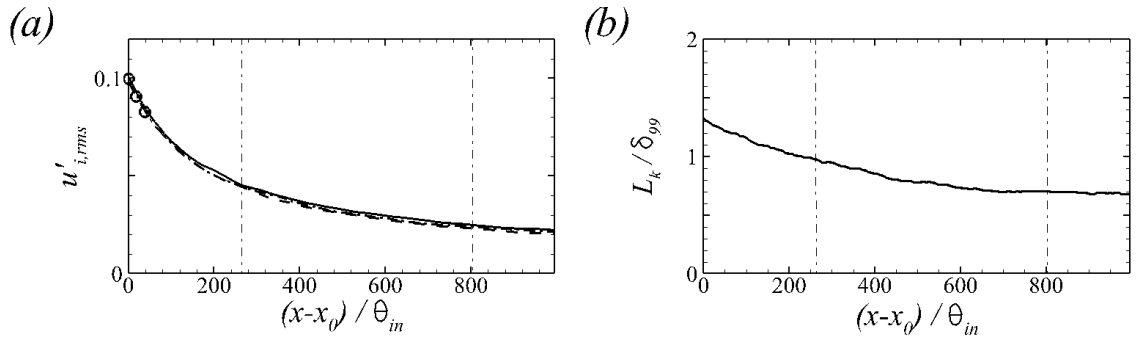

Figure 3.2: (a) Comparison of downstream evolution of free-stream turbulence in the main simulation, (—) u'_{rms}, (- - -) v'_{rms}, (- · -) w'_{rms}, and (◯) Tu of the decaying turbulence (reproduced from figure 2.2(a)). (b) Downstream evolution of the integral lengthscale, L_k/δ_{99}. Thin dashed-dotted lines mark streamwise positions where $Re_\theta = \{1900, 3000\}$ in FST computation.

boundary layer beneath a quiescent free stream and a second case with free-stream vortical forcing. They are designated the reference (REF) and forced (FRC) cases (an additional forced case with smaller scale HIT is reported in §3.6). In the forced configuration, the free-stream turbulence decays with downstream distance, and figures 3.2a and b show the evolution of its normal stresses and length scale. The Reynolds normal stresses are isotropic, and their decay in space in the main simulation matches the temporal evolution of Tu shown in figure 2.2(a), and reproduced in figure 3.2a (circle symbols). The lengthscale of FST is now redefined as $L_k \equiv -k^{3/2}/U_\infty\,(dk/dx)$, and remains on the order of the 99% boundary-layer thickness, δ_{99} (figure 3.2b). This choice is motivated by our understanding of the interaction of vortical perturbations with mean shear: Disturbances with spanwise and wall-normal lengthscales on the order of the boundary layer thickness, and elongated in the streamwise direction, are most effective at permeating the mean shear and inducing an energetic response

Designation	Simulation	Domain size (θ_{in})	No. of Grid points	Resolution
		$L_x \times L_y \times L_z$	$N_x \times N_y \times N_z$	$\Delta x^+, \Delta y^+, \Delta z^+, \Delta t^+$
REF	TBL	$1200 \times 80 \times 80$	$6912 \times 768 \times 768$	9.3, 0.28-7.7, 5.6, 0.048
FRC	TBL+HIT	$1000 \times 80 \times 160$	$5760 \times 768 \times 1536$	9.3, 0.28-7.7, 5.6, 0.043

Table 3.1: Summary of simulation parameters, and the spatial and temporal resolutions.

[88, 89]. For the present free-stream turbulence, the first two criteria are satisfied and the low-frequency components of the streamwise wavenumbers satisfy the third one.

Both the REF and FRC boundary-layer simulations start at the same stramwise position, $Re_{\theta,in} = 1200$. The differences in lengths and widths of the domains were guided by results from preliminary simulations. The domain of the 'FRC' case is slightly shorter in the streamwise direction, which is partially compensated by a faster increase in the momentum thickness Reynolds number (see figure 3.3). Its larger spanwise extent is required to accommodate the formation of wider structures. In both cases, the grid is uniformly spaced in the streamwise and spanwise directions whereas a non-uniform grid distribution is used in the wall-normal direction. The grid spacings reported in table 3.1 in wall units are normalized by the friction velocity at the inlet to the simulation domain.

The convective outflow condition $\partial u_i/\partial t + c\partial u_i/\partial x = 0$ is applied at the outlet of the simulation domain, where c is the local bulk velocity. The no-slip condition is imposed at the bottom wall. Periodic boundary conditions are applied in the spanwise

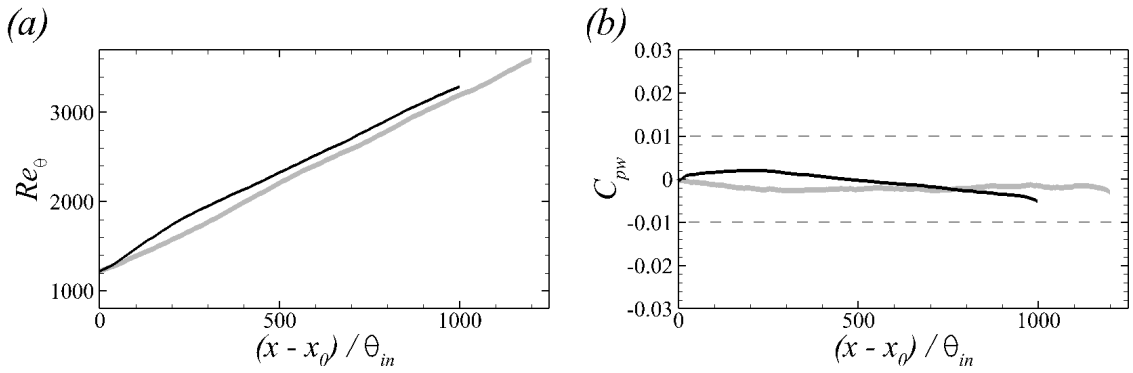

Figure 3.3: Downstream dependence of (a) momentum thickness Reynolds number $Re_\theta \equiv U_\infty \theta/\nu$, and ($b$) mean pressure coefficient at the wall C_{pw}. (Gray) Reference simulation and (black) forced case.

direction. At the top boundary, appropriate treatment is required to maintain zero-pressure gradient (ZPG) boundary layer, even in presence of high levels of FST.

3.2.2 Top boundary condition

A distribution of suction velocity is applied at the top boundary in order to maintain zero pressure-gradient in the streamwise direction. The suction velocity is evaluated using an active controller. First, a measure of the streamwise free-stream velocity is evaluated and used as a sensor,

$$u_s(x;t) = \frac{1}{\tau}\int_{t-\tau}^{t} \frac{\int_0^{L_y}\int_0^{L_z}(1-\Gamma(\mathbf{x},t))\,u(\mathbf{x},t)\;dz\;dy}{\int_0^{L_y}\int_0^{L_z}(1-\Gamma(\mathbf{x},t))\;\;dz\;dy}\;dt \tag{3.1}$$

where τ is an averaging timescale for the controller, and Γ is an indicator function which is zero in the free stream and unity in the boundary layer. The method for defining Γ is covered in the next section. The averaged streamwise velocity u_τ during

τ is

$$u_\tau(x,y;t) = \frac{1}{\tau}\frac{1}{L_z}\int_{t-\tau}^{t}\int_0^{L_z} u(\mathbf{x},t)\; dz\; dt. \tag{3.2}$$

The suction velocity at the top boundary is computed as a superposition of continuity constraint over time τ and the action of the controller,

$$v_{top}(x;t) = -\frac{d}{dx}\int_0^{L_y} u_\tau(x,y;t)\; dy + \sigma\frac{V_\infty}{U_\infty}\left(u_s(x;t) - u_T(x)\right), \tag{3.3}$$

where u_T is the target streamwise free-stream velocity which is unity in ZPG. The control factor is σ, and V_∞/U_∞ is a reference rate of free-stream vertical to streamwise velocities for the canonical mean boundary layer profile. The boundary conditions on the other directions are $u_{top} = 1$ and $(\partial w/\partial y)_{top} = 0$. In the present study, the timescale τ is comparable to the integral time scale of FST, $t_k = L_k/U_\infty$.

The downstream dependence of pressure coefficient at the wall,

$$C_{pw} \equiv \frac{\overline{p}_{(x,y=0)} - \overline{p}_{(x_0,y=0)}}{\frac{1}{2}\rho U_\infty^2}$$

is shown in figure 3.3. It remains well within the range $-0.005 < C_{pw} < 0.002$, which satisfies the condition for ZPG.

3.2.3 Conditional sampling

The starting point for conditional sampling is to define an indicator function, $\Gamma(\mathbf{x},t)$, which is unity in the boundary layer and zero in the free stream. Its spanwise

and time average is the intermittency,

$$\gamma = \frac{1}{L_z \Delta T} \int_{T_0}^{T_0+\Delta T} \int_0^{L_z} \Gamma(\mathbf{x}, t)\ dz\ dt, \tag{3.4}$$

which is the probability that the fluid is part of the boundary-layer flow. A general quantity ϕ can then be separated into its boundary-layer ϕ^B and free-stream ϕ^F constituents,

$$\phi^B = \Gamma(\mathbf{x}, t)\phi(\mathbf{x}, t) \tag{3.5}$$

$$\phi^F = (1 - \Gamma(\mathbf{x}, t))\phi(\mathbf{x}, t). \tag{3.6}$$

Using this decomposition, the conventional and conditional means are,

$$\overline{\phi} = \frac{1}{L_z \Delta T} \int_{T_0}^{T_0+\Delta T} \int_0^{L_z} \phi(\mathbf{x}, t)\ dz\ dt \tag{3.7}$$

$$\overline{\phi}^B = \frac{\int_{T_0}^{T_0+\Delta T} \int_0^{L_z} \phi(\mathbf{x}, t)\Gamma(\mathbf{x}, t)\ dz\ dt}{\int_{T_0}^{T_0+\Delta T} \int_0^{L_z} \Gamma(\mathbf{x}, t)\ dz\ dt} \tag{3.8}$$

$$\overline{\phi}^F = \frac{\int_{T_0}^{T_0+\Delta T} \int_0^{L_z} \phi(\mathbf{x}, t)(1 - \Gamma(\mathbf{x}, t))\ dz\ dt}{\int_{T_0}^{T_0+\Delta T} \int_0^{L_z} (1 - \Gamma(\mathbf{x}, t))\ dz\ dt}, \tag{3.9}$$

where superscripts B and F identify boundary-layer and free-stream quantities. The conventional mean can be related to boundary-layer and free-stream components, weighted by the local intermittency factor,

$$\overline{\phi} = \gamma \overline{\phi}^B + (1 - \gamma)\overline{\phi}^F. \tag{3.10}$$

Reynolds decomposition can be performed relative to each of the three averages,

$$\phi = \overline{\phi} + \phi' \tag{3.11}$$

$$\phi^B = \overline{\phi}^B + \phi^* \quad \text{for boundary-layer flow,} \tag{3.12}$$

$$\phi^F = \overline{\phi}^F + \phi'' \quad \text{for free-stream flow.} \tag{3.13}$$

Analysis of the perturbations relative to the conditional means is intended to examine the turbulence dynamics within each region of the flow, separately. In contrast, Hancock and Bradshaw [29] evaluated conditional statistics of perturbation quantities relative to the conventional mean, in order to measure the contribution from each fluid to overall statistics.

Unlike the intermittency weighted average (3.10), higher-order statistics evaluated relative to conditional and conventional means are related by more elaborate expressions. For example, the Reynolds stresses is given by,

$$\overline{u_i' u_j'} = \gamma\ \overline{u_i^* u_j^*}^B + (1-\gamma)\overline{u_i'' u_j''}^F + \gamma(1-\gamma)\left(\overline{u_i}^F - \overline{u_i}^B\right)\left(\overline{u_j}^F - \overline{u_j}^B\right). \tag{3.14}$$

Also, commutation of conditional averaging and the derivative operator is not always possible, for example,

$$\overline{\frac{\partial \overline{\phi}^B}{\partial x_i}}^B = \frac{\partial \overline{\phi}^B}{\partial x_i} \quad ; \quad \overline{\frac{\partial \phi}{\partial x_i}}^B = \frac{\partial \overline{\phi}^B}{\partial x_i} + \overline{\frac{\partial \phi^*}{\partial x_i}}^B \neq \frac{\partial \overline{\phi}^B}{\partial x_i}, \tag{3.15}$$

and similarly for F. This affects various terms in the turbulence kinetic energy budget

(see Appendix A), for example the pseudo-dissipation,

$$\begin{aligned}\frac{1}{Re}\overline{\frac{\partial u_i'}{\partial x_k}\frac{\partial u_i'}{\partial x_k}} &= \frac{1}{Re}\left\{\gamma\,\overline{\frac{\partial u_i^*}{\partial x_k}\frac{\partial u_i^*}{\partial x_k}}^{B} + (1-\gamma)\overline{\frac{\partial u_i''}{\partial x_k}\frac{\partial u_i''}{\partial x_k}}^{F}\right. \\ &+\gamma\left(2\frac{\partial \overline{u_i}^B}{\partial x_k}\overline{\frac{\partial u_i}{\partial x_k}}^{B} - \frac{\partial \overline{u_i}^B}{\partial x_k}\frac{\partial \overline{u_i}^B}{\partial x_k}\right) + (1-\gamma)\left(2\frac{\partial \overline{u_i}^F}{\partial x_k}\overline{\frac{\partial u_i}{\partial x_k}}^{F} - \frac{\partial \overline{u_i}^F}{\partial x_k}\frac{\partial \overline{u_i}^F}{\partial x_k}\right) \\ &\left.-\frac{\partial \gamma\overline{u_i}^B}{\partial x_k}\frac{\partial \gamma\overline{u_i}^B}{\partial x_k} - \frac{\partial (1-\gamma)\overline{u_i}^F}{\partial x_k}\frac{\partial (1-\gamma)\overline{u_i}^F}{\partial x_k} - 2\left(\frac{\partial \gamma\overline{u_i}^B}{\partial x_k}\frac{\partial (1-\gamma)\overline{u_i}^F}{\partial x_k}\right)\right\}.\end{aligned} \tag{3.16}$$

The averaging durations in the present simulations are $\Delta T = 1200\theta_{in}/U_\infty$ and $810\theta_{in}/U_\infty$ for the reference and forced cases, respectively. Since the forced configuration is twice as wide in the homogeneous spanwise direction, the shorter averaging time is sufficient for statistical convergence.

3.3 The interface between the boundary layer and the free stream

Numerous recent studies have examined the turbulent/non-turbulent interface (TNTI) in free and wall-bounded shear flows [e.g. 10, 12, 18, 40, 49]. An effective approach is to define the interface as an iso-surface of vorticity magnitude which, if appropriate normalized, becomes independent of Reynolds number in spatially developing flows. Borrell. and Jiménez [12] proposed the following normalization,

$$|\omega|^* = \frac{|\omega|}{u_\tau^2/\nu}\sqrt{\delta_{99}^+}. \tag{3.17}$$

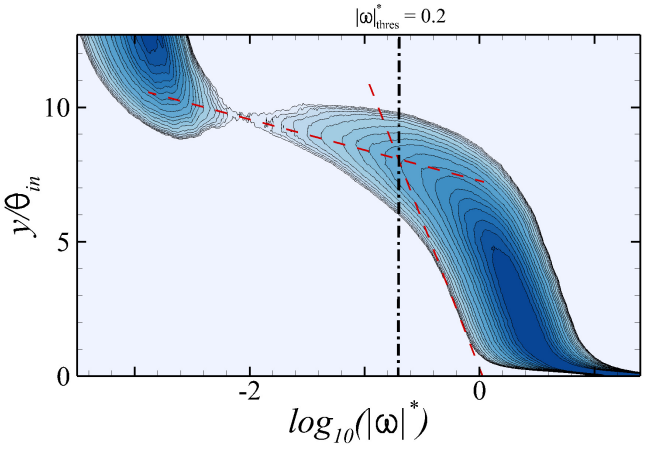

Figure 3.4: Probability density function (p.d.f.) of $\log_{10}|\omega|^*$ at inlet ($Re_\theta \approx 1200$). Dashed lines identify the wake regime of the boundary layer and the geometric center of outer intermittent flow regime.

The threshold level, $|\omega|^*_{\text{thres}}$, is then determined from the probability density function of the logarithm of $|\omega|^*$, which is plotted in figure 3.4 for the inlet boundary layer. The two dashed lines in the figure were proposed by Lee et al. [49], and mark the wake regime and the geometric center of the outer intermittent regime. Their intersection is the normalized vorticity threshold, here $|\omega|^*_{\text{thres}} = 0.2$, and the associated wall-normal height is $y/\delta_{99} \sim 1.0$. In conventional boundary layers below a quiescent free stream, the TNTI separates vortical ($|\omega|^* > |\omega|^*_{\text{thres}}$) and irrotational flow ($|\omega|^* < |\omega|^*_{\text{thres}}$). The method can be adopted in reference simulation where the turbulent boundary layer is beneath a quiescent free stream, but is not applicable when the free stream is itself turbulent.

Another approach to differentiate the boundary layer and free stream is inspired by experiments in high Prandtl number fluids, where one stream is heated [29]. In

the simulations, a scalar marker can be set to unity in the boundary layer and zero in the free stream at the inflow plane. In the case of a conventional boundary layer, diffusion of the scalar is effective within the boundary layer only, and a value of zero guarantees that the scalar is associated with the free stream. But when the free stream is turbulent, diffusion becomes appreciable on both sides of the interface, and it once again becomes difficult to separate the boundary-layer and free-stream fluids. In order to remedy this effect, in numerical simulations, we eliminate diffusion all together and adopt a levelset approach for capturing the interface [41].

In the original work by Osher and Sethian [64], the interface is an iso-level of the function φ that is tracked by solving,

$$\frac{\partial \varphi}{\partial t} + \frac{\partial u_j \varphi}{\partial x_j} = 0. \tag{3.18}$$

The value of φ is the unit distance from the interface, which is marked by $\varphi = 0$. Since mass conservation is difficult to maintain in the original formulation, [19] proposed a conservative levelset method. Instead of solving for the evolution of φ, their approach utilizes a hyperbolic tangent function,

$$\psi = \frac{1}{2}\left(\tanh\left(\frac{\varphi}{2\epsilon}\right) + 1\right) \tag{3.19}$$

where $\psi = 0.5$ marks the interface location, and $\epsilon \equiv 0.5 \min(\Delta x, \Delta y, \Delta z)$ determines its thickness. The evolution of ψ is given by,

$$\frac{\partial \psi}{\partial t} + \frac{\partial u_j \psi}{\partial x_j} = 0. \tag{3.20}$$

In order to maintain a smooth ψ field, without spurious oscillations, a re-initialization equation is required,

$$\frac{\partial \psi}{\partial \tau} + \nabla \cdot (\psi (1 - \psi) \mathbf{n}) = \nabla \cdot (\epsilon (\nabla \psi \cdot \mathbf{n}) \mathbf{n}), \tag{3.21}$$

where τ is a pseudo-timestep and $\mathbf{n} \equiv \nabla\psi/|\nabla\psi|$ is the interface normal vector. Note that $\mathbf{n}$ is computed from φ. When the reinitialization equation is invoked, it is solved to a steady state in pseudo-time, which requires 3 to 4 iterations in our simulations.

Time integration of (3.20) and (3.21) was performed using the third-order total variation diminishing Runge-Kutta scheme. The advection term in (3.20) was discretized in space using a fifth-order upstream central scheme, while second-order central differencing was adopted for the compression and diffusion terms in (3.21). In order to accelerate the computation, the levelset equations are solved in a narrow-band around the interface only [69]. Extensive validation of the interface tracking algorithm was reported by [41], who computed the evolution of the Zalesak's disk ([90]) and the evolution of linear and nonlinear instability waves in two-fluid flows [16, 17].

At the inflow plane, the value of ψ is set to unity in the boundary layer and zero in the free stream, and is a hyperbolic tangent profile within 5 computational cells that straddle the interface. The instantaneous location of the interface, within the inlet boundary-layer data, is identified using the vorticity threshold $|\omega|^*_{\text{thres}} = 0.2$, and is assigned the value $\psi = 0.5$. Downstream, a sharp interface is maintained by virtue of the reinitialization equation. The indicator function, used in the conditional sampling,

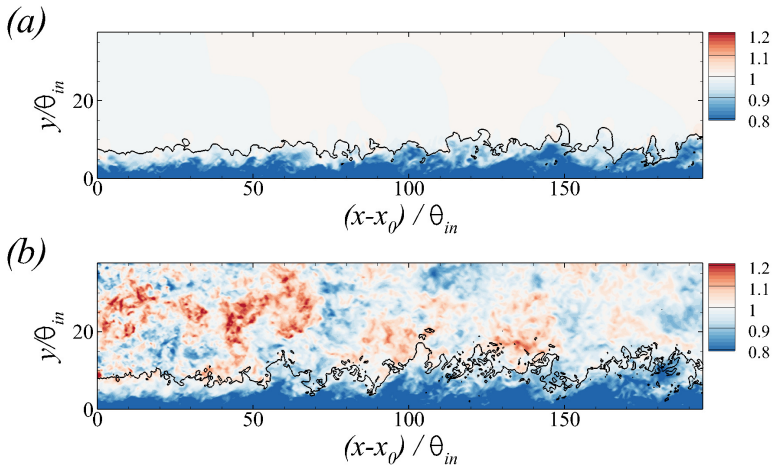

Figure 3.5: Contours of streamwise velocity u, and the line identifies the levelset $\psi = 0.5$, in turbulent boundary layer (top) without and (bottom) with free-stream turbulence.

is thus defined as $\Gamma = 1$ when $\psi \geq 0.5$ in the boundary-layer fluid, and $\Gamma = 0$ when $\psi < 0.5$ in the free stream. A sample result is shown in figure 3.5, where the interface $\psi = 0.5$ is plotted along with contours of the streamwise velocity. Using $\psi = 0.5$, we can unambiguously differentiate the boundary-layer and free-stream turbulence and perform conditional sampling.

3.3.1 Comparison of conditional sampling using $|\omega|^*_{\text{thres}}$ and ψ

The vorticity threshold and the levelset approaches identify two different interfaces. The former marks the outer diffusive edge of the boundary layer, while the latter marks the material fluid that belongs to the boundary layer at the inlet. Previous studies of conventional boundary layers, with quiescent free streams, have used

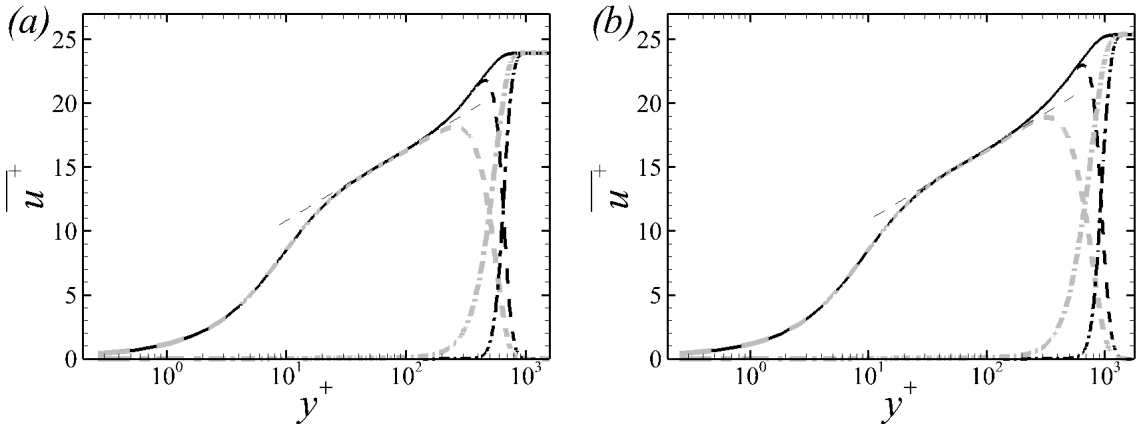

Figure 3.6: Mean streamwise velocity profiles in inner scaling at (*a*) $Re_\theta = 1900$ and (*b*) $Re_\theta = 3000$ in 'REF' case. (—) Conventional mean; (- - -) boundary-layer contribution; (- · -) free-stream contribution. Conditional statistics are evaluated using (black) vorticity threshold $|\omega|$ and (gray) level set function ψ. The thin dashed line is given by $\overline{u}^+ = 2.44\ \ln(y^+) + 5.2$.

the vorticity threshold. Since it is not applicable in presence of free-stream turbulence, we will adopt the levelset method throughout this work. A comparison of both techniques is, nonetheless, possible in the reference case without free-stream turbulence.

Figure 3.6 shows the mean velocity profiles at two different streamwise locations in the reference simulation. In addition to the conventional mean, the figures also show the conditional averages in the boundary layer, $\gamma\overline{u}^{+B}$, and in the free stream, $(1-\gamma)\overline{u}^{+F}$. The conditional curves are plotted twice, using the vorticity threshold (black) and the levelset approach (gray). Considering the free-stream contribution, it decays faster into the boundary layer when evaluated using the vorticity threshold relative to the levelset approach. In the former case, free-stream fluid that becomes part of the boundary layer as it diffuses only contributes to the boundary-layer statistics.

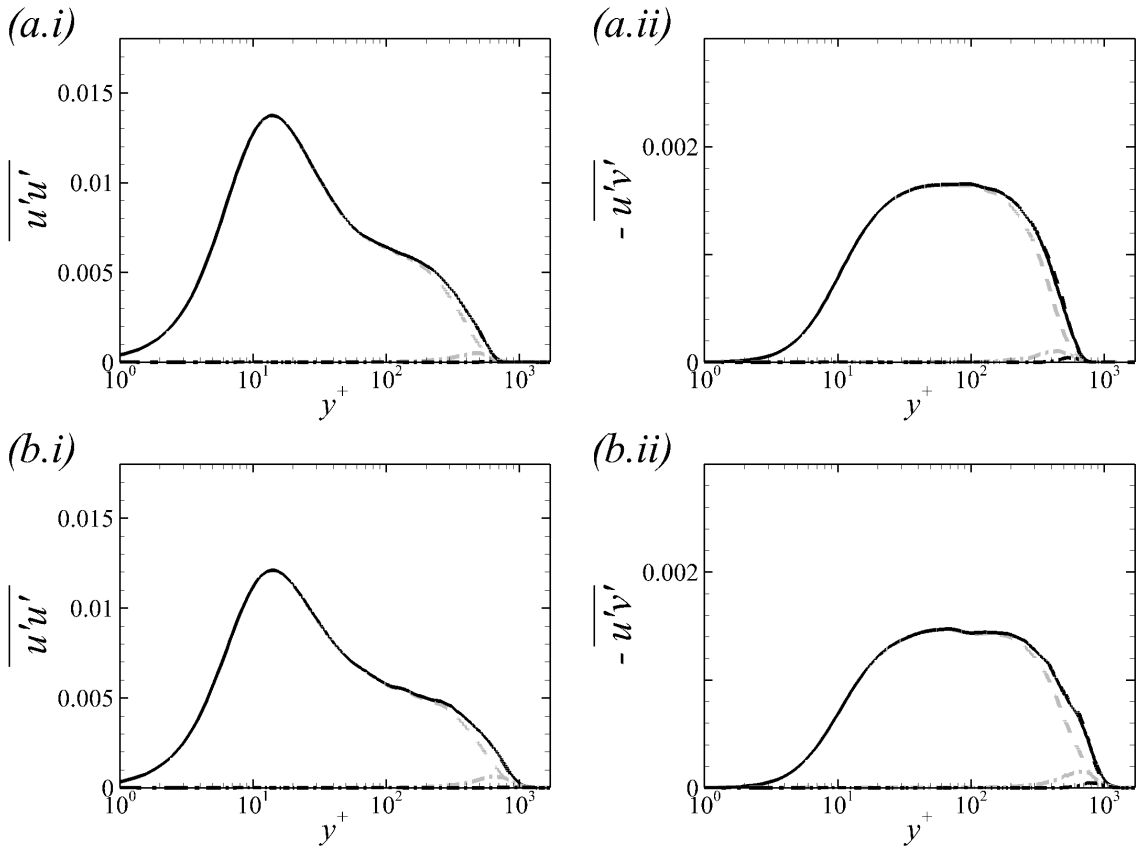

Figure 3.7: Reynolds stresses profiles at (a) $Re_\theta = 1900$ and (b) $Re_\theta = 3000$ in 'REF' case; (i) $\overline{u'u'}$ and (ii) $-\overline{u'v'}$, both normalized by U_∞^2. Other details as in figure 3.6.

In the levelset case, however, fluid that is assigned to the free stream at the inlet continues to contribute to the free-stream statistics even if it became part of the turbulent boundary layer. It is important to note that, at both downstream locations considered, the log-law region is fully captured by the boundary-layer conditional average, independent of the sampling technique.

The boundary-layer and free-stream contributions to the Reynolds stresses, evaluated using both the vorticity threshold and the levelset approach, are plotted in figure 3.7. The boundary-layer term $\gamma\overline{u_i^* u_j^*}$ traces the conventional average from the wall through the inner peak and the log-law region. When $|\omega|^*_{\text{thres}}$ is used for conditional averaging, the free-stream contribution $(1-\gamma)\overline{u_i'' u_j''}$ is essentially negligible even in the wake region. When ψ is used, the free-stream contribution is small, and increases slightly downstream as more outer fluid becomes turbulent. Throughout the rest of this study, the levelset method will be adopted to evaluate conditional statistics, since it is equally applicable when the boundary layer is beneath a quiescent or turbulent free stream.

3.3.2 Statistics of the interface

The interface between the boundary layer and the free stream is defined as $y_I \equiv y\,(\psi = 0.5)$. Iso-surfaces of this quantity are plotted in figure 3.8, coloured by distance from the wall over a limited streamwise range. The figure qualitatively shows that the presence of the free-stream turbulence significantly enhances the undulation of

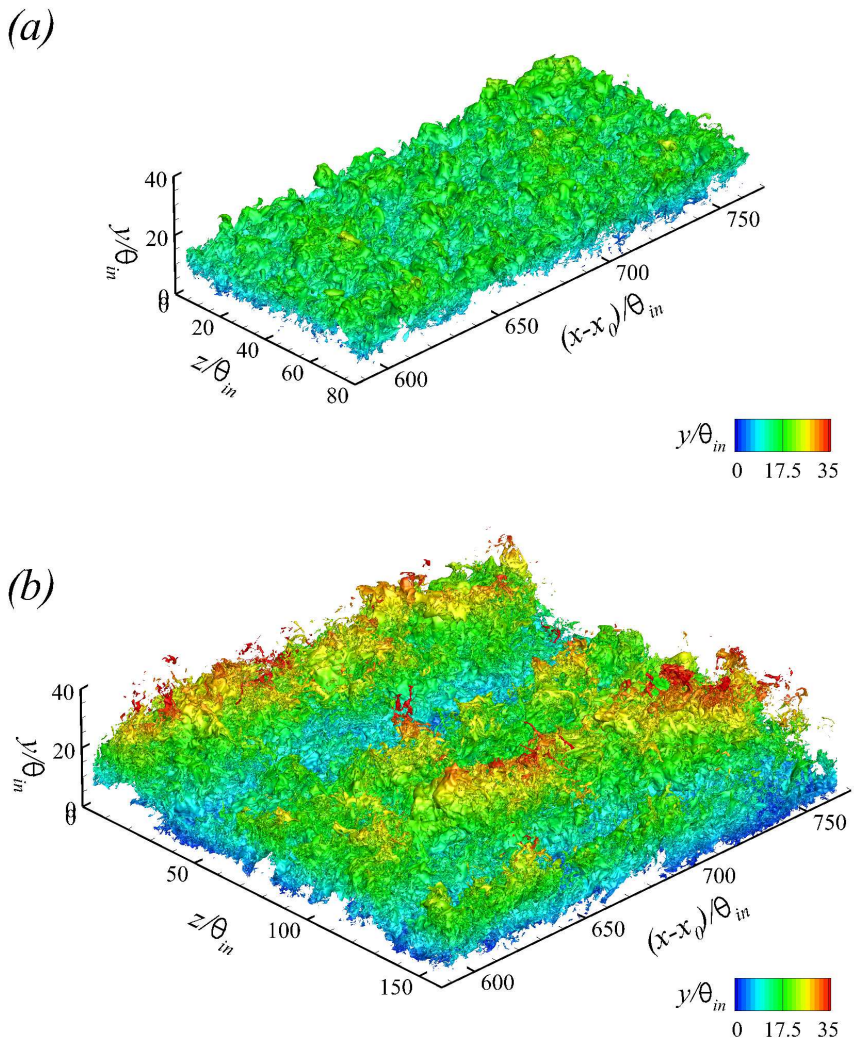

Figure 3.8: Iso-surfaces of y_I coloured by wall-normal height y/θ_{in}. (a) REF case and (b) FRC case.

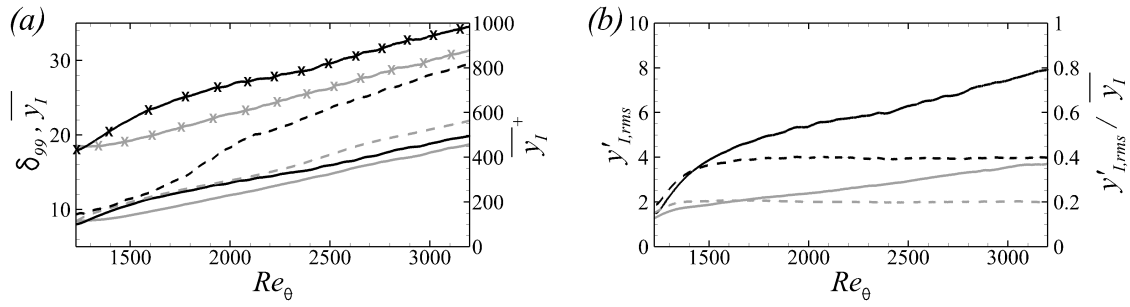

Figure 3.9: (a) Downstream evolution of (—) $\overline{y_I}$, (–×–) $\overline{y_I}^+$, and (- - -) δ_{99}. (b) Evolution of (—) $y'_{I,rms}$ and (- - -) $y_{I,rms}/\overline{y_I}$. (Gray) REF; (black) FRC.

the interface, relative to a canonical boundary layer.

Figure 3.9(a) contrasts the downstream development of the mean height of the interface, $\overline{y_I}$, and the 99% thickness of the boundary layer, δ_{99}. By construction, both quantities start at the same height at the inlet plane since $\psi = 0.5$ was instantaneously assigned based on the vorticity threshold $|\omega|^*_{\text{thres}} = 0.2$ (see figure 3.4). For the reference boundary layer (gray lines), both $\overline{y_I}$ and δ_{99} grow at similar rates, although the latter is slightly higher because the growing boundary layer entrains free-stream fluid. The results for the forced case show a steeper increase in δ_{99}, which was noted in previous studies [29]. Note, however, that δ_{99} bears no physical significance, and is sensitive to the details of the mean velocity profile. On the other hand, $\overline{y_I}$ is the mean height of the material line separating the boundary layer from the free stream at the inlet. This quantity has a much smoother evolution with downstream distance, and shows only a moderate increase relative to the reference case.

The excursions of the interface relative to the mean location are measured by the

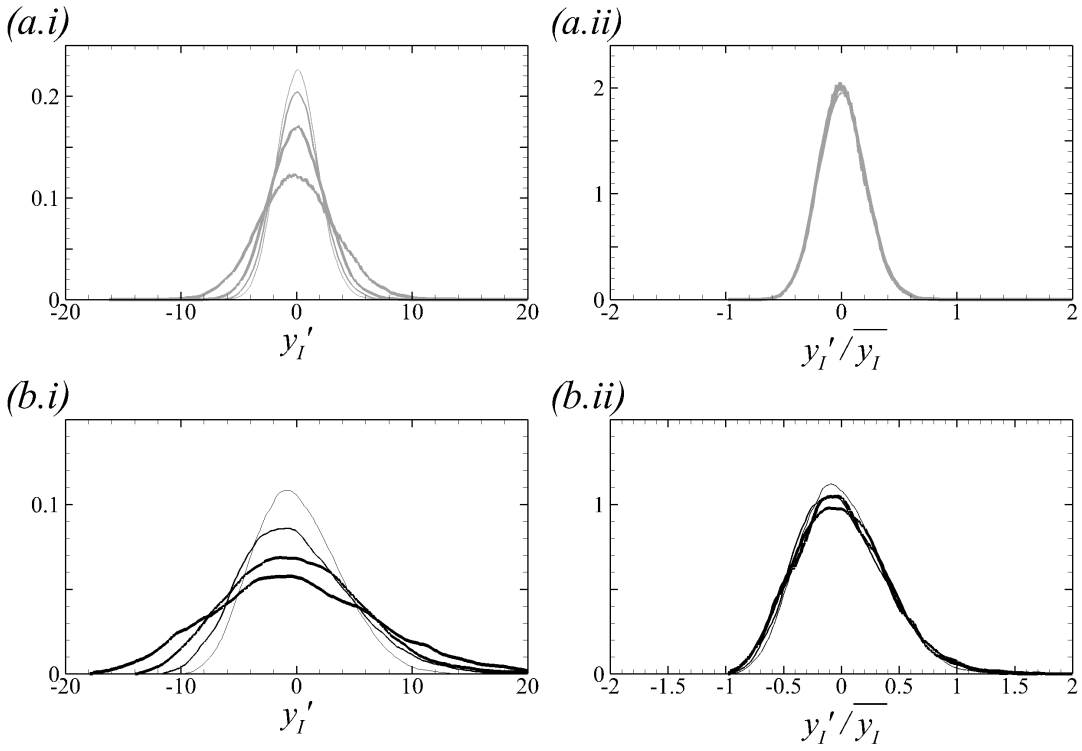

Figure 3.10: P.D.F. of (i) y_I' and (ii) $y_I'/\overline{y_I}$ for (a) REF and (b) FRC. Thin to thick lines correspond to the streamwise position, $(x - x_0)/\theta_{in} = \{100, 200, 400, 800\}$.

root-mean-square of the fluctuations in its height, $y'_{I,rms}$, in figure 3.9(b). Lee et al. [49] showed that $y'_{I,rms}$ increases with downstream distance, and is nearly linearly proportional to $\overline{y_I}$ in turbulent boundary layers. The same trend is observed in the reference flow, where $y'_{I,rms}/\overline{y_I}$ is nearly flat in figure 3.9(b). When the boundary layer is forced by free-stream turbulence, the root-mean-square of the interface excursions increases significantly. When normalized by $\overline{y_I}$, it still shows an initial increase before it plateaus. The larger excursions in the interface height correspond to enhanced transport at the interface.

The probability density function (p.d.f.) of the interface excursions is plotted in

figure 3.10. The distributions for each flow nearly collapse when normalized by the mean value, $y_I'/\overline{y_I}$. In the reference boundary-layer simulation, the p.d.f. is practically symmetric, and its skewness at the shown locations is in the range $[0.12, 0.15]$. In presence of free-stream forcing, the normalized p.d.f. curves are wider, and is more positively skewed in the direction of the free stream. Quantitatively, the skewness increases by as much as three folds, and is in the range $[0.35, 0.5]$. Since $\overline{y_I}$ is larger in the forced case, the spread in the p.d.f. of y' is even more pronounced than in the reference case.

Due to the larger undulation of the interface height in the forced case, the intermittency γ spreads more rapidly as shown in the left panel of figure 3.11. In the middle panels, wall-normal profiles for two streamwise positions are plotted versus $y/\overline{y_I}$, and show good collapse in this outer scaling. When the boundary layer is buffeted by external disturbances, the profiles of γ clearly show its spread both towards the free stream and the wall. The free-stream turbulence is thus expected to influence the flow deep inside the mean shear. The extent of its penetration should, however, be viewed in inner scaling as shown in the rightmost panels. In the reference simulation, the contribution of the outer flow, or $(1 - \gamma)$, vanishes in the log layer; In the forced case, while the contribution of the free stream remains finite in the log layer, it is vanishingly small in the buffer layer.

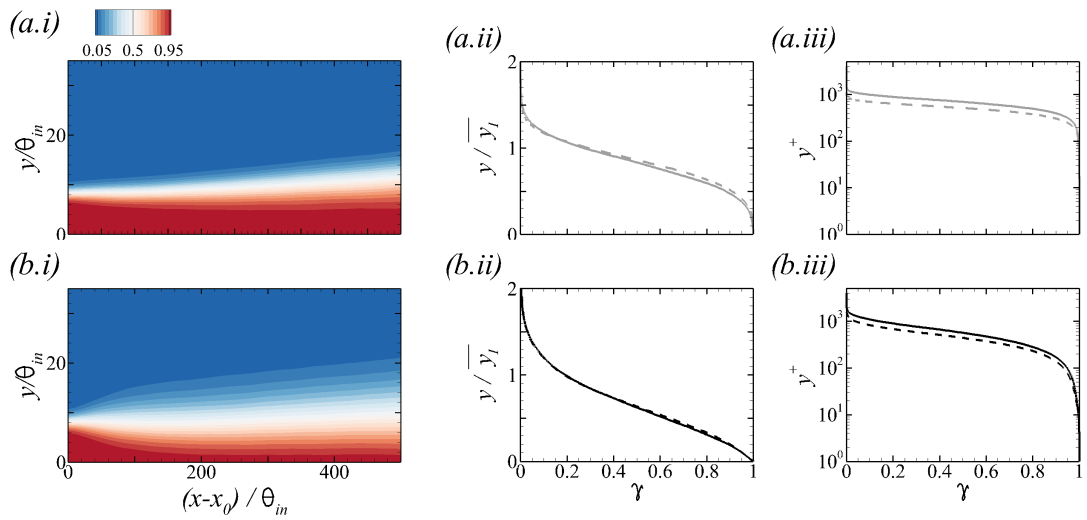

Figure 3.11: (i) Contours of intermittency γ near the inlet of the simulation domain. Profiles of γ (ii) in outer scaling and (iii) in inner scaling at (- - -) $Re_\theta = 1900$ and (—) $Re_\theta = 3000$. (a) REF and (b) FRC.

3.4 Modification of BL statistics due to free-stream turbulence

3.4.1 The skin friction

When turbulent boundary layers are exposed to free-stream vortical forcing, the wall shear stress is enhanced. This effect is shown in figure 3.12(a) where the downstream evolution of the skin-friction coefficient, $C_f \equiv \tau_w/(0.5\rho U_\infty^2)$, is plotted versus the momentum-thickness Reynolds number. The coefficient increases by approximately 15% at $Re_\theta = 1900$. Many of the subsequent discussions will be supported by results at this location and also $Re_\theta = 3000$ farther downstream. Note that these Reynolds numbers do not correspond to the same streamwise positions in the reference

and forced boundary layers (c.f. figure 3.3). Matching Re_θ is, however, the appropriate choice for comparing the two flows. Hereafter, gray and black lines always indicate the profile of the reference and forced turbulent boundary layers, respectively.

In figure 3.12a, the C_f curve is shifted upwards in presence of free-stream forcing, and retains its dependence on Re_θ. Similar to Esteban et al. [22], the correlation $C_f = 2\left[\log(Re_\theta)/0.384 + C\right]^{-2}$ is used to match the data by adjusting C. For the reference flow, $C = 4.127$ is anticipated [61] and yields good agreement for the present data. The constant must be adjusted to $C = 2.77$ in order to accurately capture the dependence of C_f on Re_θ in presence of free-stream turbulence.

An interpretation of the skin friction in terms of three physical phenomena was recently proposed by Renard and Deck [71]. In a frame moving with the free stream speed U_∞, the flat plate is pulled to the left at $-U_\infty$. In that setting, the skin-friction coefficient can be interpreted as of the average normalized power imparted by the wall motion onto the fluid, and is the sum of three contributions,

$$\begin{aligned} C_{f,RD} \;=\; & \underbrace{\frac{2}{U_\infty^3}\int_0^\infty \nu\left(\frac{\partial \overline{u}}{\partial y}\right)^2 dy}_{C_{f,a}} + \underbrace{\frac{2}{U_\infty^3}\int_0^\infty -\overline{u'v'}\frac{\partial \overline{u}}{\partial y}\, dy}_{C_{f,b}} \\ & + \underbrace{\frac{2}{U_\infty^3}\int_0^\infty (\overline{u}-U_\infty)\left(\overline{u}\frac{\partial \overline{u}}{\partial x} + \overline{v}\frac{\partial \overline{u}}{\partial y}\right) dy}_{C_{f,c}}, \end{aligned} \tag{3.22}$$

where $\overline{\tau}/\rho$ is the total shear stress. The term $C_{f,a}$ is the rate of dissipation of mean streamwise kinetic energy into heat, $C_{f,b}$ is the rate of production of turbulence kinetic energy, and $C_{f,c}$ is the rate of change in the streamwise kinetic energy in the mean flow. The symbols in figure 3.12(a) show the reconstruction of the right-hand side of

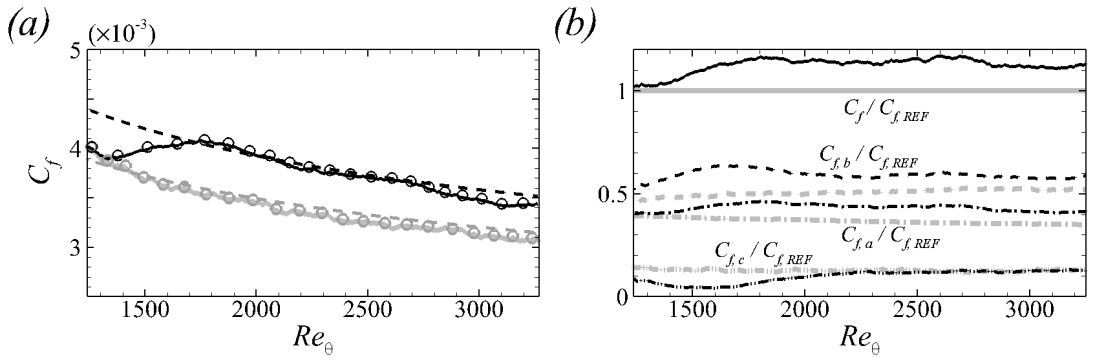

Figure 3.12: (a) Skin-friction coefficients computed from (—) the wall-shear stress $C_f = \tau_w / \frac{1}{2}\rho U_\infty^2$ and ($\circ$) the decomposition (3.22). Dashed lines are the correlation $C_f = 2\left[\log(Re_\theta)/0.384 + C\right]^{-2}$, where $C = 4.127$ for REF and $C = 2.77$ for FRC. (b) Contributions to the skin-friction coefficient normalized by $C_{f,REF}$; (—) C_f, (- · -) $C_{f,a}$, (- - -) $C_{f,b}$ and (- · · -) $C_{f,c}$. (Gray) REF; (black) FRC.

equation 3.22, which agrees with the direct evaluation of the skin friction from the gradient at the wall.

All the terms in the decomposition 3.22 are plotted in figure 3.12(b), normalized by the total friction coefficient from the reference boundary-layer simulation, $C_{f,REF}(Re_\theta)$. The term $C_{f,c}$, which accounts for the streamwise energy in the mean flow, is the smallest contributor to the friction and is initially reduced in response to the free-stream turbulence but subsequently recovers. The overall increase in the friction coefficient is therefore due to the augmentations of $C_{f,a}$ and $C_{f,b}$, namely the dissipation in the mean profile and the production of turbulence kinetic energy. Both involve $-\overline{u'v'}$, although indirectly in the first term through the mean-flow distortion by the stress.

The integral in $C_{f,a}$ converges to 95% of its total below $y^+ = 20$ and to 99% by $y^+ = 100$. Within the region $y^+ < 100$, the change in $\partial\overline{u}/\partial y$ from its wall

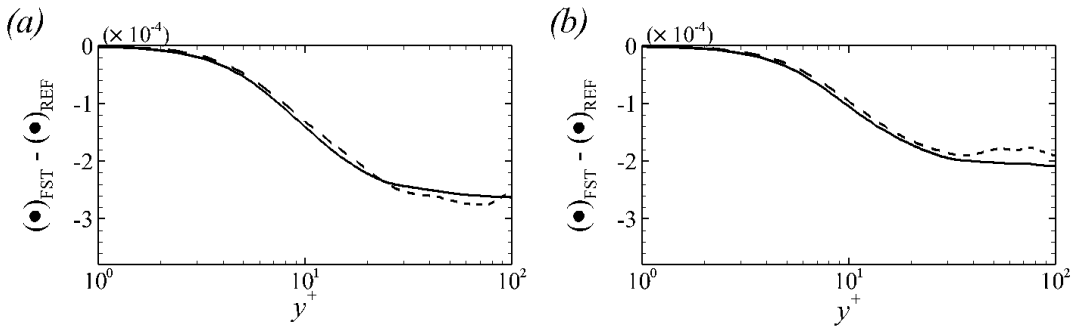

Figure 3.13: The differences in (—) $\frac{1}{Re}\left(\frac{\partial\overline{u}}{\partial y} - \frac{\partial\overline{u}}{\partial y}\Big|_{y=0}\right)$ and in (- - -) $\overline{u'v'}$ in the reference and forced boundary layers. (a) $Re_\theta = 1900$; (b) $Re_\theta = 3000$.

value is nearly equal to the Reynolds shear stress, and therefore the increase in $C_{f,a}$ when the boundary layer is forced is related to the increase in $\overline{-u'v'}$. This relation is demonstrated by integrating the mean-momentum equation for a ZPG boundary layer from the wall to a height y,

$$\frac{1}{Re}\left\{\frac{\partial\overline{u}}{\partial y} - \left[\frac{\partial\overline{u}}{\partial y}\right]_{y=0}\right\} = \int_y \frac{\partial(\overline{u}\ \overline{u})}{\partial x}\ dy + \overline{u}\ \overline{v} + \overline{u'v'}. \tag{3.23}$$

The above expression was evaluated for both the reference and forced flows, and the difference $(\bullet)_{REF} - (\bullet)_{FRC}$ is plotted in figure 3.13, at $Re_\theta = 1900$ and 3000. The results demonstrate how changes in $\overline{-u'v'}$ indirectly impact the dissipation in the mean-velocity profile, $C_{f,a}$.

The shear stress appears directly in $C_{f,b}$ whose increase signals a potential change in the energetics of the wall turbulence. Consider the kinetic energy budget,

$$\underbrace{\overline{u}_j\frac{\partial k}{\partial x_j}}_{\mathcal{A}} = -\underbrace{\overline{\frac{\partial u_i' p'}{\partial x_i}}}_{\mathcal{R}} \underbrace{-\frac{1}{2}\frac{\partial\overline{u_j' u_i' u_i'}}{\partial x_j}}_{\mathcal{T}} \underbrace{-\overline{u_i' u_j'}\frac{\partial\overline{u_i}}{\partial x_j}}_{\mathcal{P}} \underbrace{-\frac{1}{Re}\overline{\frac{\partial u_i'}{\partial x_j}\frac{\partial u_i'}{\partial x_j}}}_{\varepsilon} + \underbrace{\frac{1}{Re}\frac{\partial^2 k}{\partial x_j \partial x_j}}_{\mathcal{D}}, \tag{3.24}$$

where $k \equiv \frac{1}{2}\overline{u_i' u_i'}$ is the turbulence kinetic energy (TKE) per unit mass. In the above

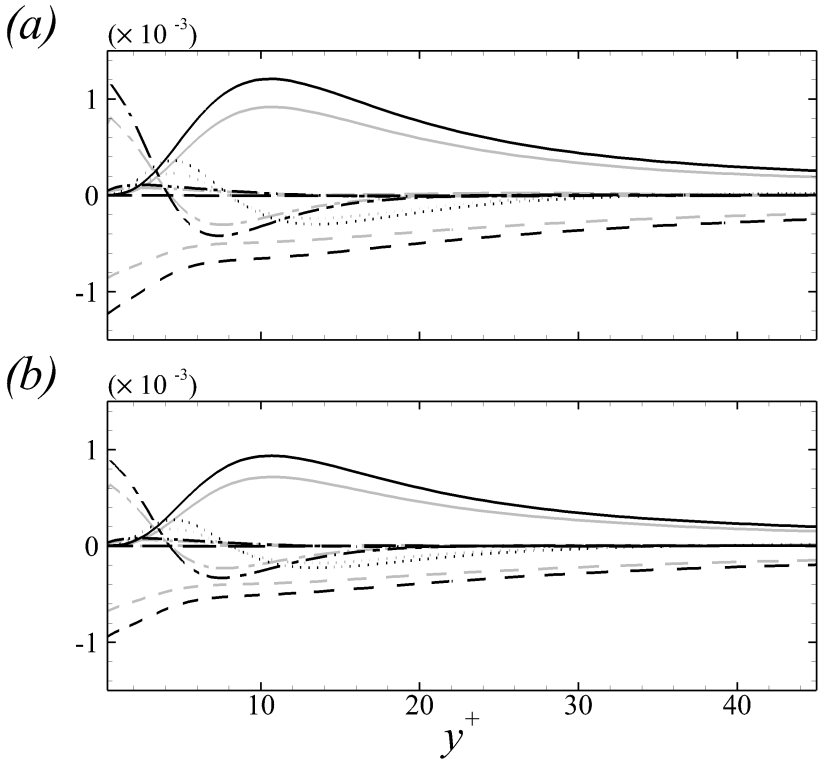

Figure 3.14: Wall-normal distributions of TKE-budget terms normalized by U_∞^3/θ_{in} at (a) $Re_\theta = 1900$ and (b) $Re_\theta = 3000$; (——) production $\mathcal{P}$, (- - -) dissipation $-\varepsilon$, (- · -) viscous diffusion $\mathcal{D}$, (· · · ·) turbulent advection $\mathcal{T}$, (- · · · -) pressure diffusion $\mathcal{R}$ and (– –) mean advection $\mathcal{A}$. (Gray) REF; (black) FRC.

expression, $\mathcal{A}$ is mean advection, $\mathcal{R}$ is pressure-diffusion, $\mathcal{T}$ is turbulent advection, $\mathcal{P}$ is rate of production, ε is the pseudo-dissipation, and $\mathcal{D}$ is viscous diffusion. These terms are plotted in the near-wall region in figure 3.14, and compared in the reference and forced boundary layers. The magnitude of every term is increased in the forced flow, especially the rate of dissipation and viscous diffusion at the wall. The production term is also appreciably increased in the buffer layer, which is consistent with the results by Péneau et al. [68]. Based on the analysis by Renard and Deck [71], in a frame moving with the free-stream speed U_∞, an increase of $\overline{u'v'}\partial\overline{u}/\partial y$, and hence $\mathcal{P}$, requires additional power input from the moving wall. This leads to an increase in wall shear stress, or drag. Further evidence of the connection between $\overline{u'v'}\partial\overline{u}/\partial y$ and drag is provided in figure 3.15. The wall-normal peak of the former term is plotted versus downstream Reynolds number, and its trend matches the change in the skin friction very well.

A number of interesting lines of query arise from the above results: Firstly, the enhanced production in the buffer layer can be ascribed to either a change in the mean-flow profile or the Reynolds shear stresses. The two are not independent of one another, and which has a more pronounced effect is of interest. Secondly, the most pronounced change in the production term takes place in the buffer layer. Whether the free-stream turbulence penetrates this deep into the boundary layer or the near-wall turbulence dynamics are modified should be assessed. If the former, an increase in the shear stress is curious because the free-stream turbulence is isotropic; and

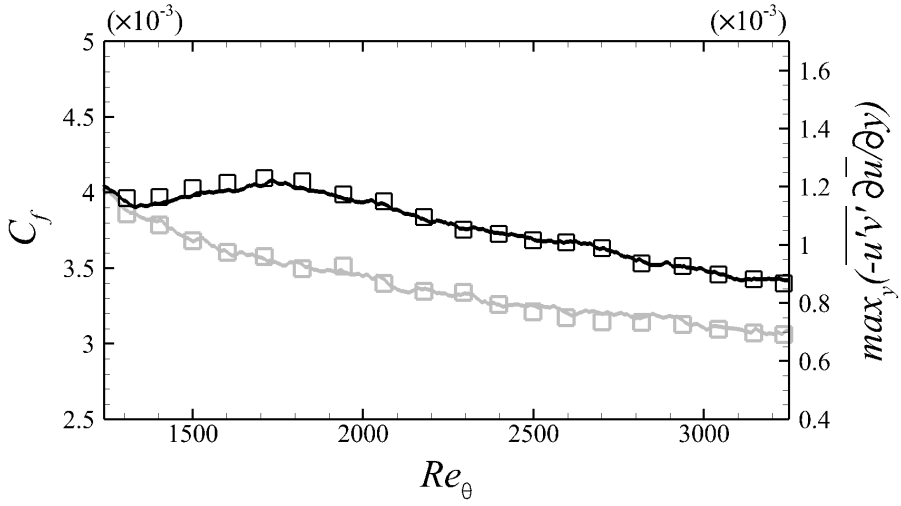

Figure 3.15: Evolutions of (—) C_f and (□) a peak value of $-\overline{u'v'}\frac{\partial \overline{u}}{\partial y}$. (Gray) REF; (black) FRC.

the latter case would also warrant an explanation. These factors are examined by evaluating the contributions of the boundary-layer and free-stream fluids to the flow statistics.

3.4.2 Conditional statistics

The mean streamwise velocity profiles are plotted in outer and inner scalings in figure 3.16, at $Re_\theta = 1900$ and 3000. Note that the adopted outer lengthscale is $\overline{y_I}$ (left panels), and not δ_{99} which does not bear a clear physical significance. The mean-velocity profiles are fuller in the FRC case, which is indicative of the enhanced mixing that was remarked by Hancock and Bradshaw [29]. It is also consistent with the increase in $C_{f,a}$ (equation 3.22), which is the integral of $(\partial\overline{u}/\partial y)^2$ in the wall-normal direction, or dissipation of mean streamwise kinetic energy. The left panels

also show the conditional velocity profiles in the boundary layer, $\overline{u}^B$, and in the free stream, $\overline{u}^F$. These profiles, when weighted by their probabilities, make up the unconditional mean (equation 3.10). Therefore they lie on either side of the mean, and agree with it near the wall and in the free stream, respectively. The free-stream conditional profile, $\overline{u}^F$, is larger in the forced flow than in the reference case, but seems to only impact the mean profile near the outer edge of the boundary layer. It appears, at least based on outer scaling, that changes in the overall mean track the changes in the boundary-layer curve.

The middle panels of figure 3.16 show the same profiles in viscous scaling. Both the unforced and forced boundary layers have a logarithmic region, $\overline{u}^+ = 2.44\ln(y^+)+5.2$, at both Reynolds numbers. In presence of free-stream turbulence, a significant depression of the boundary-layer profile occurs in the wake region, which is consistent with the increase in drag; The logarithmic, buffer and viscous regions are hardly affected. The unconditional mean profiles are thus consistent with earlier experiments [28, 77] and simulations [50]. The conditional profiles, $\overline{u}^{+B}$ and $\overline{u}^{+F}$, are interesting. In both the reference and forced computations, $\overline{u}^{+B}$ faithfully follows the conventional mean up to the edge of the log layer, and are lower in the intermittent wake region. Conversely, the free-stream curves reproduce the outer uniform flow, retain a higher velocity than the conventional mean inside the boundary layer, and collapse in viscous scaling. A deeper reach of $\overline{u}^{+F}$ towards the wall in the forced flow is evident in the figure. When weighted by their probabilities (right panels), the conditional

averages yield the contributions to the mean by the boundary layer, $\gamma\overline{u}^{+B}$, and the free stream, $(1-\gamma)\overline{u}^{+F}$. In the unforced flow, the boundary-layer contributions still show a log-layer behaviour and decay sharply in the wake region due to the intermittency weighting. In contrast, when free-stream turbulence forcing is present, the boundary-layer contribution no longer traces the log law, although the logarithmic behaviour is re-established once the free-stream contribution is added to recover the conventional mean. In order to explain the 'universality', or robustness, of the log law in forced boundary layers, Hancock and Bradshaw [29] verified that the departure from equilibrium is inappreciable, and that the rates of production and dissipation of turbulence-kinetic-energy are dominant and nearly balance in that region. The same dominant balance was verified in the present FRC case.

Wall-normal profiles of Reynolds stresses are presented in figure 3.17. In general, all the stresses are enhanced when the boundary layer is subjected to free-stream turbulence and, outside the mean shear, all the normal stresses match the outer turbulence levels and the shear stress in nearly zero. Two key observation are important to note, related to the stresses in the log and buffer layers respectively. Firstly, the increase in $\overline{u'u'}$ in the log layer exceeds the free-stream value, and is therefore not a mere upward shift of the curve. Partial evidence of enhanced local production of $\overline{u'u'}$ is available from the Reynolds shear stress, $\overline{u'v'}$, which is increased in the log layer. This trend is curious, and can not be directly ascribed to the free-stream turbulence since it is itself void of $\overline{u'v'}$. Instead, the increase in normal stresses $\overline{v'v'}$ due to the

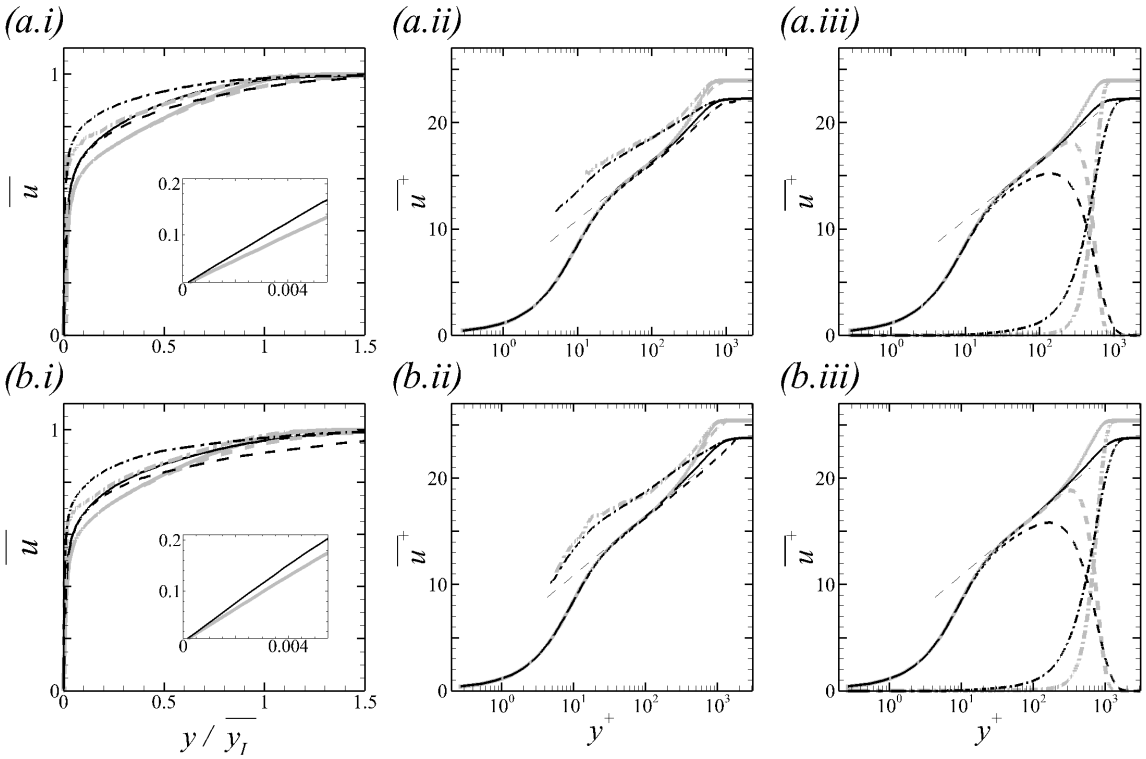

Figure 3.16: Profiles of mean streamwise velocity at (*a*) $Re_\theta = 1900$ and (*b*) $Re_\theta = 3000$, normalized by (*i*) U_∞ and (ii-iii) u_τ. (i-ii) (- - -) Boundary-layer velocity $\overline{u}^B$; (- · -) free-stream velocity $\overline{u}^F$. (iii) (- - -) Boundary-layer contribution $\gamma\overline{u}^B$; (- · -) free-stream contribution $(1-\gamma)\,\overline{u}^F$. The thin dashed line: $\overline{u}^+ = 2.44\,\ln(y^+) + 5.2$. (Gray) REF; (black) FRC.

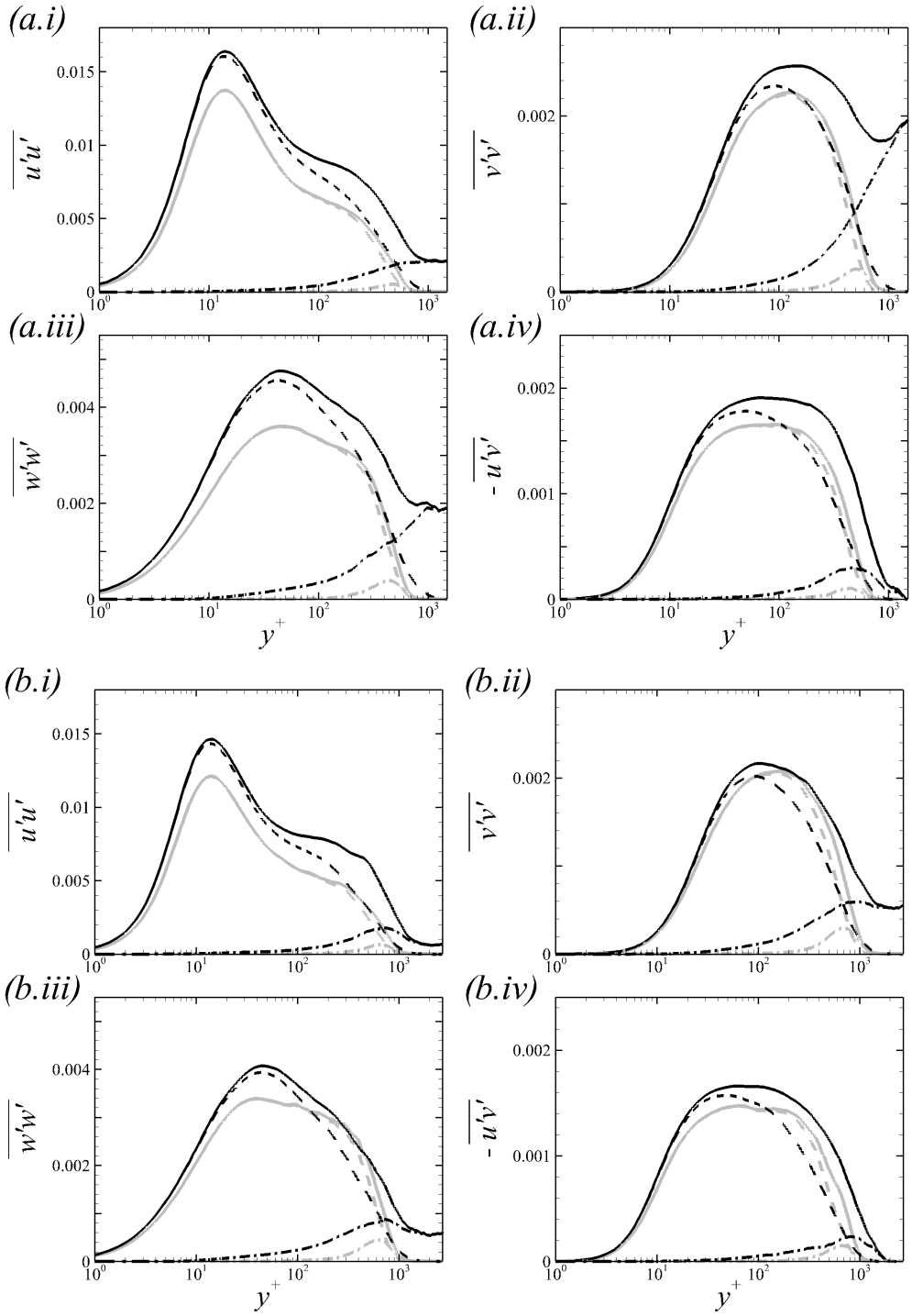

Figure 3.17: Reynolds stresses profiles at (a) $Re_\theta = 1900$ and at (b) $Re_\theta = 3000$. (i) $\overline{u'u'}$; (ii) $\overline{v'v'}$; (iii) $\overline{w'w'}$; (iv) $-\overline{u'v'}$, all normalized by U_∞^2. (—) Conventional statistics; (- - -) boundary-layer contribution; (- · -) free-stream contribution. (Gray) REF; (black) FRC.

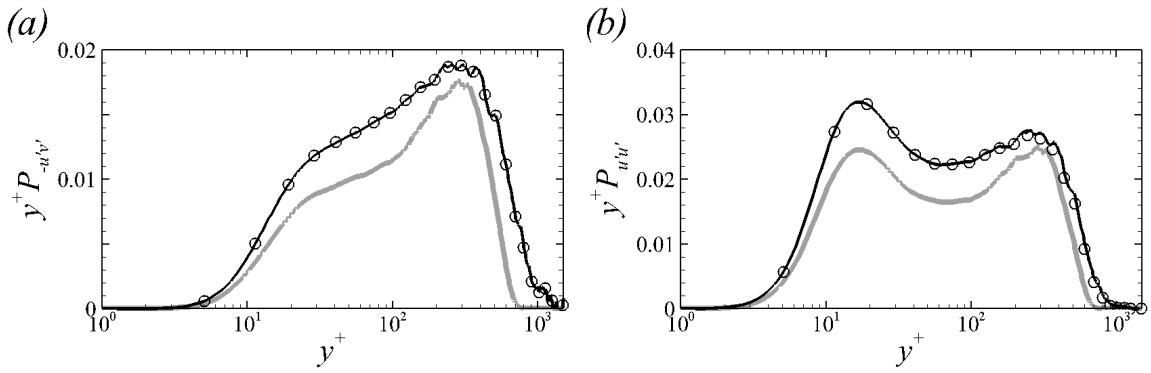

Figure 3.18: Profiles of production of Reynolds shear and streamwise-normal stresses at $Re_\theta = 1900$. (a) $y^+\mathcal{P}_{-u'v'}$; (b) $y^+\mathcal{P}_{u'u'}$. Symbols mark the leading contributions: (a) $y^+\overline{v'v'}\partial\overline{u}/\partial y$; (b) $-2y^+\overline{u'v'}\partial\overline{u}/\partial y$. Production terms are normalized by U_∞^3/θ_{in}. (Gray) REF; (black) FRC.

ingested free-stream turbulence acts against the mean shear to produce Reynolds shear stress that, in turn, enhances the production of $\overline{u'u'}$. Profiles of the relevant production terms, $\mathcal{P}_{u_i'u_j'} \equiv -\overline{u_j'u_k'}\partial\overline{u_i}/\partial x_k - \overline{u_i'u_k'}\partial\overline{u_j}/\partial x_k$, are provided in figure 3.18, pre-multiplied by y^+. In this form, the area under the curve corresponds to the integral of production, which is clearly enhanced in the log layer. The symbols identify the dominant contributions, and confirm that $\overline{v'v'}$ leads to an increase in production of the shear stress and, in turn, production of $\overline{u'u'}$ in the outer layer.

The second observation from figure 3.17 concerns the depth towards the wall over which the Reynolds stress profiles are altered in presence of free-stream turbulence. The increase in $\overline{v'v'}$ diminishes as we approach the wall and nearly vanishes within the buffer layer, which is consistent with the extent of penetration of free-stream turbulence into the boundary layer and the decay of the intermittency curves (see figure 3.11). In contrast, the increases in the other stresses preserve their magnitudes

deeper into the boundary layer, beyond the decay of the intermittency curves. For example, the increases in the streamwise and spanwise normal stresses are evident below the locations of their respective peaks, and even deeper than the buffer layer. Therefore, these changes can not be caused by the free-stream turbulence directly, and the explanation for enhanced production in the log layer does not carry over to the buffer region. This point is further supported by the conditional free-stream contributions, $(1-\gamma)\overline{u_i'' u_j''}^F$, which vanish farther away from the wall than the increase in the stresses. In summary, while the free-stream turbulence has a direct contribution to the normal stresses in the outer intermittent region and enhances production of $\overline{u'v'}$ and $\overline{u'u'}$ in the log layer, it also indirectly modifies the turbulence deeper towards the wall in a manner that warrants further examination — a matter that we address in §3.5.

The increase in production is connected to the changes in Reynolds shear stress within the boundary layer. The cross-correlation coefficient, $\overline{u'v'}/(u'_{rms}v'_{rms})$, is reduced in presence of external forcing because the isotropy of the free-stream turbulence destroys the coherence of the boundary-layer turbulence [29]. Nonetheless, the magnitude of Reynolds shear stress $\overline{u'v'}$ increases in the boundary layer as shown in figure 3.17, and as reported by others [68]. This increase is curious because the free-stream forcing is free of any mean shear stress, and because the extent of its penetration into the mean shear, towards the wall, is shallower than the region of increase in kinetic energy and production which persist deeper towards the wall.

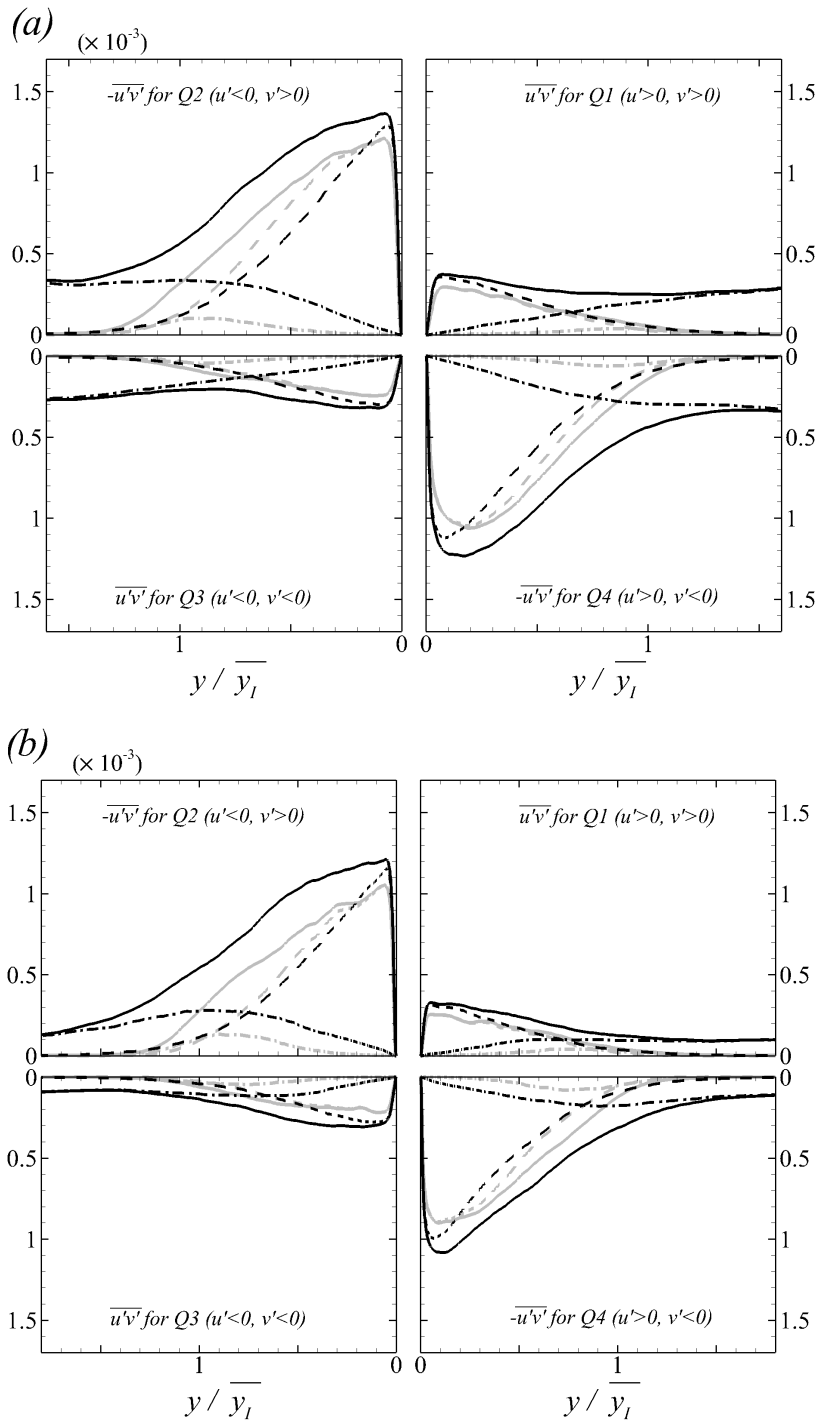

Figure 3.19: Contributions to Reynolds shear stress, $-\overline{u'v'}$ normalized by U_∞^2, from each quadrant at (*a*) $Re_\theta = 1900$ and (*b*) $Re_\theta = 3000$. (——) Conventional statistics; (- - -) boundary-layer contribution; (- · -) free-stream contribution. (Gray) REF; (black) FRC.

A more detailed account of the increase in the Reynolds shear stress can be obtained from quadrant analysis [83]. The analysis was performed for both the reference and forced flows, and is shown in figure 3.19 at the two downstream locations, $Re_\theta = 1900$ and 3000. In the reference flow, ejection (Q2: $u' < 0$ and $v' > 0$) and sweep (Q4: $u' > 0$ and $v' < 0$) events are dominant (figure 3.19). In the forced case, the isotropy of FST leads to finite, nearly equal contribution to all four quadrants at, and beyond the free-stream edge of the boundary layer, thus enhancing mixing in that region. Inside the boundary layer, the increases in Q2 and Q4 events far exceed those in the other two components. In addition, while the free-stream contribution decays within the boundary layer, a significant increase in the unconditional Q2 and Q4 events is observed near their respective peaks close to the wall. The peak of the boundary-layer contribution, which resides close to the wall, increases in magnitude but its location does not shift. The more pronounced ejections and sweeps are consistent with the higher rate of production, $P_{-u'v'}$, in the forced case (figure 3.18a).

Figure 3.20 highlights the change in the near-wall turbulence kinetic energy production and dissipation rates and their conditional contributions, all plotted in logarithmic scale. The relationship between the conventional and conditional terms is provided in Appendix A. In the reference simulation, the total dissipation is zero in the free stream, and its high level near the wall is entirely due to the boundary-layer contribution. In the forced case, the dissipation is enhanced throughout the extent of the boundary layer and is finite, albeit small, in the free stream where it is entirely

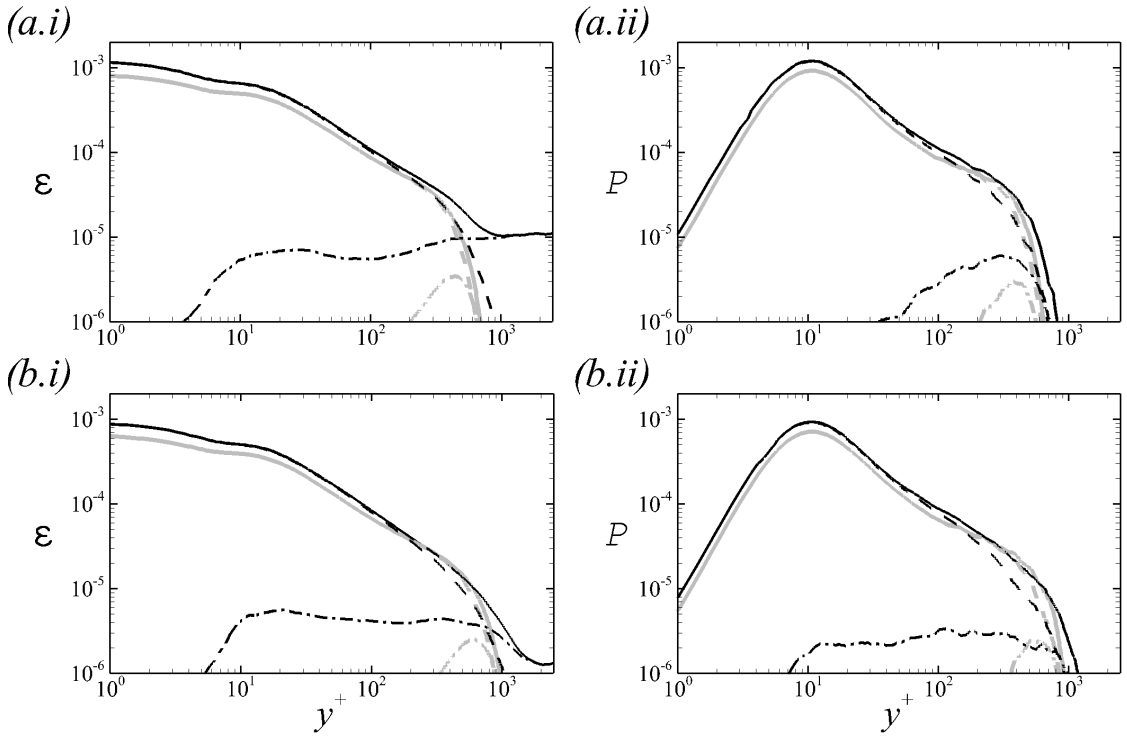

Figure 3.20: Profiles of (i) pseudo-dissipation ε and (ii) production $\mathcal{P}$ terms, both normalized by U_∞^3/θ_{in}. (a) $Re_\theta = 1900$; (b) $Re_\theta = 3000$. (—) Conventional statistics; (- - -) boundary-layer contribution; (- · -) free-stream contribution. (Gray) REF; (black) FRC.

due to the contribution of the outer fluid. The free-stream conditional average decays inside the boundary layer and is more than two orders of magnitude smaller than the boundary-layer counterpart. Similar observations are applicable to the production terms. In this case, however, the free-stream contribution vanishes outside the mean shear in both the reference and forced configurations. While it is enhanced inside the boundary layer when the flow is forced, that contribution remains more than two orders of magnitude smaller than the peak value of the total production. The increase in production near the wall ($y^+ \simeq 10$) in the forced flow is essentially entirely due to the boundary-layer contribution. These results are consistent with the notion that the increase in the peak Reynolds stresses (figure 3.17), especially $\overline{u'u'}$, is not an additive effect of injection of FST into the near-wall region. Instead, the turbulence kinetic energy and its production rate are enhanced near the wall, below the extent of penetration of free-stream perturbations. The associated changes in the structures and spectra of the wall-turbulence are examined in §3.5.

3.4.3 Discussion

The arguments set forth so far in order to explain the increase in the boundary-layer TKE in the forced flow have focused on changes in the near-wall dynamics. Another potential factor is an influx of turbulence from the free stream. This effect was considered by Hancock and Bradshaw [29], who evaluated the conditionally sampled turbulent fluxes. They concluded that the net flux is into the boundary

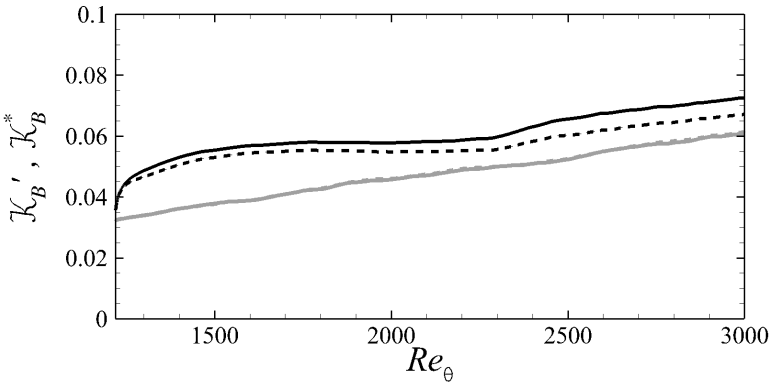

Figure 3.21: Average of the integrated perturbation kinetic energy inside the boundary layer. (—): $\mathcal{K}'_B = \overline{\int_0^\infty \frac{\Gamma}{2} u'_i u'_i dy}$; (- - -): $\mathcal{K}^*_B = \overline{\int_0^\infty \frac{\Gamma}{2} u^*_i u^*_i dy}$. (Gray) REF; (black) FRC.

layer, but their conditional sampling method relied on a diffusive scalar and they computed the perturbations relative to the unconditional mean. The present configuration is different, as we illustrate by considering the the instantaneous total kinetic energy, $K \equiv \frac{1}{2} u_i u_i$. The instantaneous flux of K relative to the interface is given by $\int_{S_I} K\,(u_j - v_j) n_j dS_I$, where S_I is the surface of the interface, and v_j and n_j are its velocity and outward unit-normal vectors. The instantaneous flux term is identically zero because the interface is a material line, $v_j = u_j$. In other words, free-stream energy is not advected across the interface — a condition that is unique to our configuration because the interface is a material line — and energy flux does not contribute to the reported changes in boundary-layer turbulence.

Another point to note is the contribution of intermittency to the change in the total turbulence kinetic energy within the boundary layer. Figure 3.21 compares $\mathcal{K}'_B = \overline{\int_0^\infty \frac{\Gamma}{2} u'_i u'_i dy}$ and $\mathcal{K}^*_B = \overline{\int_0^\infty \frac{\Gamma}{2} u^*_i u^*_i dy}$. Both quantities are evaluated within the

boundary-layer fluid only, before averaging. The first term features the kinetic energy of perturbations relative to the conventional mean and the second is relative to the conditional mean. Their near perfect agreement for the reference simulation (figure 3.21) demonstrates that the conventional and conditional means are similar within the boundary-layer fluid, over the wall-normal extent where turbulence is energetic and makes up the majority of the integral. The two quantities deviate in the forced flow, because the intermittency profiles spread deeper towards the wall, but nonetheless their relative difference remains small, 4.9% at $Re_\theta = 1900$ and 7.5% at $Re_\theta = 3000$. Therefore, the direct contribution of intermittency is small in regions within the boundary layer where the Reynolds normal stresses are increased appreciably.

Based on the present discussion, the choice of the interface as a material line precludes flux of energy from the free stream into the boundary layer. In addition, the overall increase in the turbulence kinetic energy within the boundary layer takes place largely below the region influenced by intermittency. Both points provide support to the notion that the increase in the turbulence kinetic energy inside the boundary layer is due to a change in the dynamics of the wall flow. The corresponding changes in turbulence spectra and structures are the focus of the next section §3.5.

3.5 Turbulence structures

The increases in the Reynolds streamwise stress in the log layer and the near-wall region are the outcome of changes in the turbulence structures when the boundary layer is forced by free-stream turbulence. A realization of the large-scale motions in the log layer is shown in figure 3.22, visualized using iso-surfaces of the Gaussian filtered streamwise velocity perturbations [see 49, for details of the structure identification procedures]. The figure empirically suggests that the large-scale motions are wider in the span and more elongated in the streamwise direction when the flow is forced. The enhanced coherence of the energetic structures is interesting, in particular since the free-stream turbulence is isotropic. In this section, we will quantify the change in the size of these large-scale structures, their spectral signature, and their impact on the near-wall turbulence.

In order to quantify the change in the size of the energetic large-scale structures, the two-point correlation coefficient for streamwise velocity fluctuations is computed,

$$R_{u'u'(\Delta x,y,\Delta z)} = \frac{\overline{u'_{(x,y_{ref},z,t)} u'_{(x+\Delta x,y,z+\Delta z,t)}}}{u'_{rms(x,y_{ref})}\, u'_{rms(x,y)}} \tag{3.25}$$

where y_{ref} is the reference wall-normal location. Contours of $R_{u'u'}$ are plotted in figure 3.23; line contours correspond to the reference flow and the flood contours correspond to the forced case. The figure also shows the correlation in the 45° and 135° inclined planes. In all three views, the correlation coefficient is appreciably wider in the forced flow, which demonstrates that the u-perturbation structures in the log-

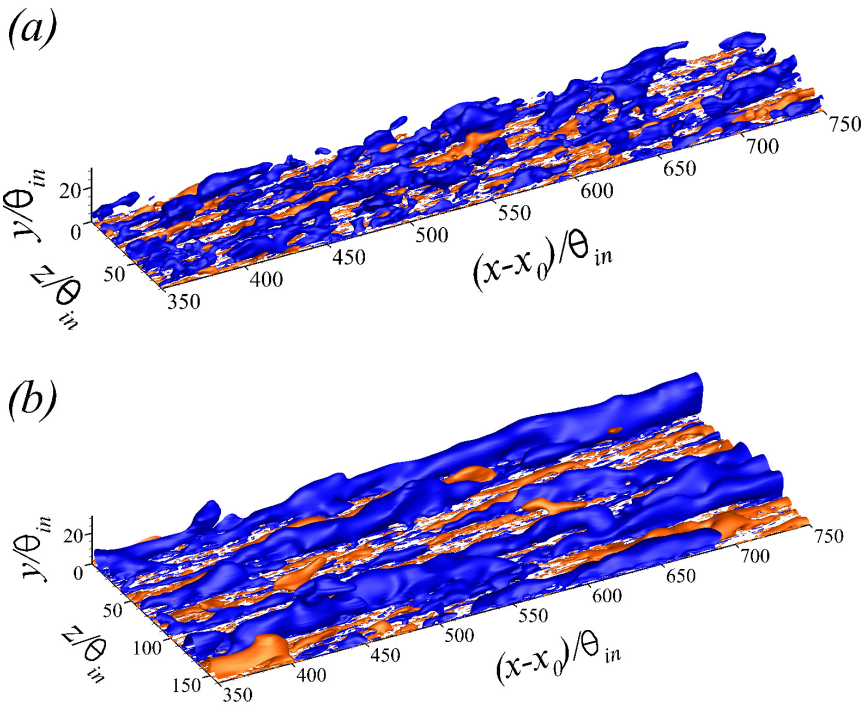

Figure 3.22: Iso-surfaces of the Gaussian-filtered flow field $\hat{u}'$. (a) REF and (b) FRC. (Blue) $\hat{u}' = -0.06$ and (red) $\hat{u}' = 0.06$.

layer are larger in streamwise, spanwise and wall-normal extent. Two characteristic lengthscales, l_{45° and l_{135°, are evaluated from the inclined planes, and are defined as the distance to $R_{u'u'} = 0.5$. Their ratio in the reference case is $l_{45^\circ}/l_{135^\circ} = 1.2$, which agrees with the value reported by Ganapathisubramani et al. [24]. Those authors attributed the fact that l_{45° is greater than l_{135° to the existence of hairpin packets. In the forced flow, the ratio increases to $l_{45^\circ}/l_{135^\circ} = 1.27$, which is consistent with enhanced hairpin activity. Geometrically, the increase in $l_{45^\circ}/l_{135^\circ}$ can arise due to a steeper inclination angle, α, or larger aspect ratio of the structures, $AR = l_{long}/l_{short}$ where l_{long} and l_{short} are the longest and shortest lengths in the x-y plane. Both quantities are plotted in figure 3.24 as a function of the threshold level of the correlation coefficient, R_{thres}, that is adopted to define the size of the structure. The inclination angle is similar in both cases, and hence does not explain the change in $l_{45^\circ}/l_{135^\circ}$. Instead, the increase in $l_{45^\circ}/l_{135^\circ}$ is due to the elongation, and hence increase in the aspect ratio, of the structures, e.g. $AR \approx 2.8$ and 3.4 for the reference and forced flow at $R_{thres} = 0.5$.

The streamwise and spanwise sizes of the structures are compared in figure 3.25, where contours of $R_{u'u'(\Delta x,\Delta z)}$ are plotted at two wall-normal positions: $y^+ \approx 100$ which is in the log layer, and $y/\overline{y_I} \approx 0.55$ which will be later identified as an important location in the spanwise energy spectra (c.f. figure 3.28). At both heights, the length of the large-scale motions is longer in the forced flow than in the reference case, e.g. it is nearly double at $y^+ \approx 100$. At $y/\overline{y_I} \approx 0.55$, the streamwise extent of the structures

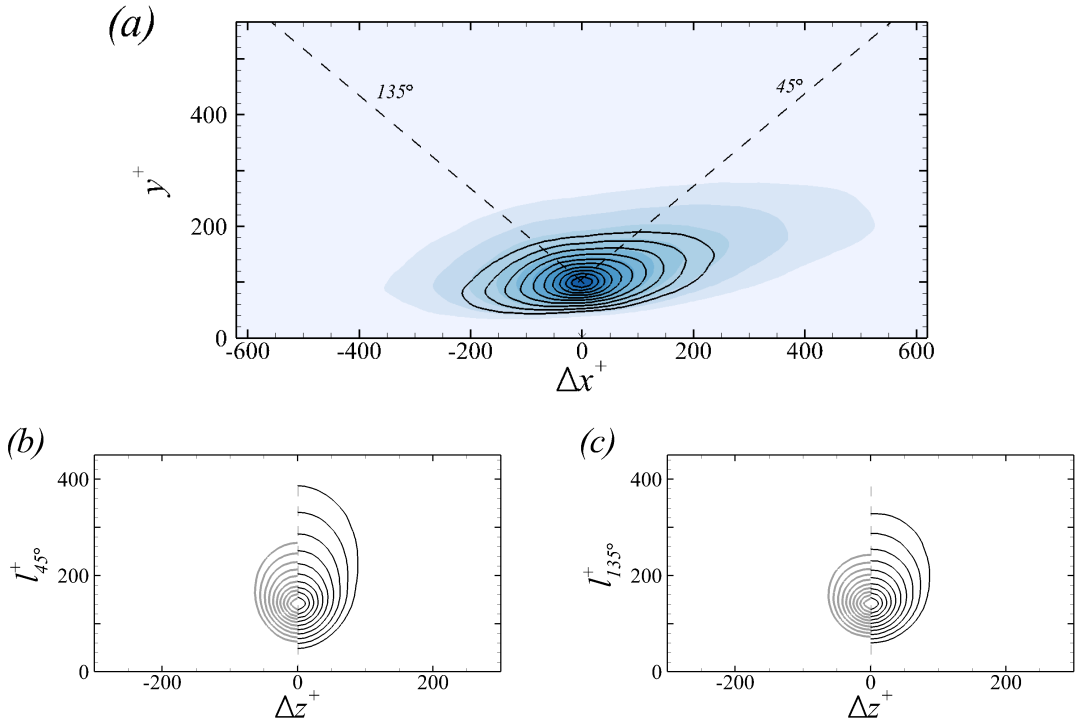

Figure 3.23: Two-point correlation, $R_{u'u'}$ at $y^+_{ref} = 100$ and $Re_\theta = 3000$. (a) $R_{u'u'}$ in the x-y plane for the (lines) REF and (flood) FRC. Correlations in the inclined planes at (b) 45° and (c) 135°. The contour levels span the range $0.5 \leq R_{u'u'} \leq 0.95$ in increments of 0.05. In (b) and (c), the left and right sides correspond to REF and FRC, respectively.

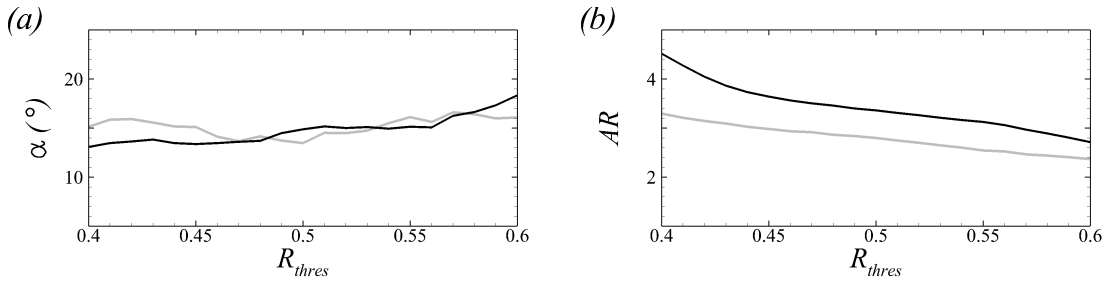

Figure 3.24: (a) Inclination angle $\alpha(^\circ)$ and (b) aspect ratio $AR \equiv l_{long}/l_{short}$ as a function of threshold level of the correlation coefficient, R_{thres}. The quantities l_{long} and l_{short} are the longest and shortest length scales in the x-y plane. (Gray) REF; (black) FRC.

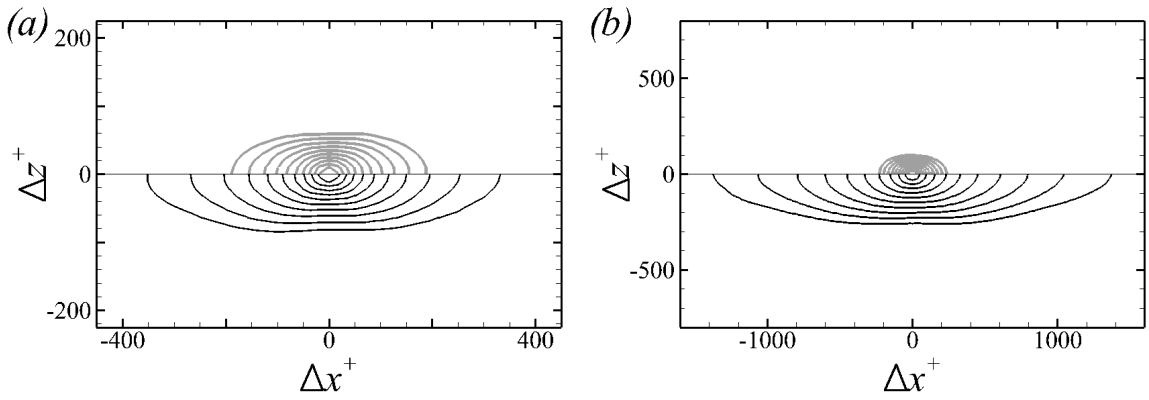

Figure 3.25: Two-point correlation $R_{u'u'(\Delta x,\Delta z)}$ at (a) $y^+ \approx 100$ and (b) $y/\overline{y_I} \approx 0.55$. Contour levels correspond to $0.5 \leq R_{u'u'} \leq 0.95$ in increments of 0.05. In (a) and (b), the top side corresponds to REF and the bottom to FRC.

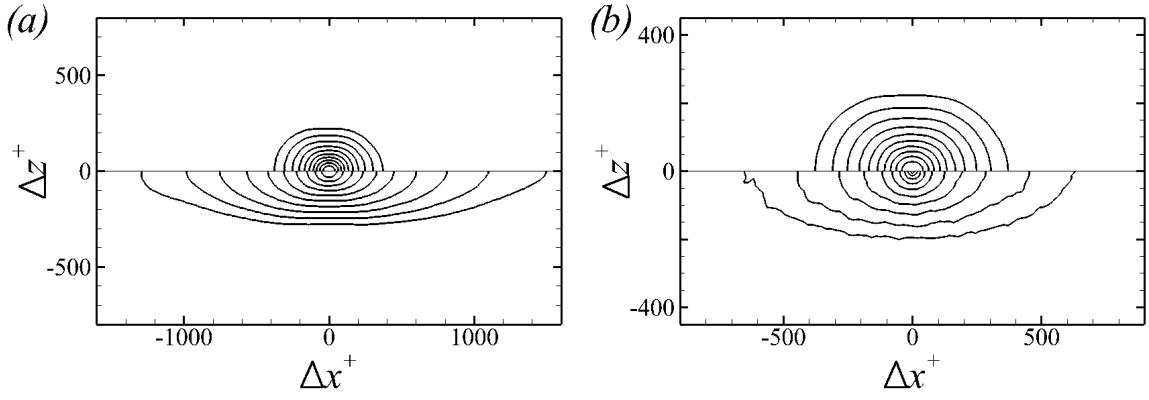

Figure 3.26: Contours of (a) $R_{u'u'(\Delta x,\Delta z)}$ and (b) $R_{u''u''(\Delta x,\Delta z)}$ in FRC. In (a) and (b), the top side corresponds to $y/\overline{y_I} \approx 3$, and the bottom is at $y/\overline{y_I} \approx 0.55$.

is further elongated by the forcing, and the width of the structures is also significantly increased. At that location, the ratio of l_x in the forced and reference flows is 5.8, and that of l_z is 2.3. The relatively larger increase in the streamwise size of boundary-layer outer motions indicates that free-stream isotropic turbulence enhances the anisotropy of wall turbulence. The interpretation based on flow structures is consistent with the statistical trends presented here (figure 3.17) and by Brzek et al. [14] over rough walls.

The correlation coefficients of the free-stream turbulence ($y/\overline{y_I} \approx 3$) and of the outer structures ($y/\overline{y_I} \approx 0.55$) are compared in figure 3.26(a). As anticipated for homogeneous isotropic free-stream turbulence, the streamwise extent of the correlation is larger than its width [70]. At $y/\overline{y_I} \approx 0.55$, the width of the correlation remains of similar order. That the spanwise scale of the outer turbulence is commensurate with the preferred size of the large-scale structures indicates that the forcing is effective at generating a boundary-layer response. On the other hand, the streamwise extent of the boundary-layer structures is appreciably longer. These observations are consistent with the notion of shear sheltering and amplification: Only low-frequency free-stream vortical perturbations can permeate the boundary layer [34, 89]. Further evidence of the filtering effect are provided by plotting the conditional correlation coefficient, $R_{u''u''}$, at the same two locations (figure 3.26(b)). The weaker streamwise decay at $y/\overline{y_I} \approx 0.55$ demonstrates that only lower frequency components of the free-stream vortical spectrum have a signature inside the boundary layer.

The contributions of the boundary-layer and free-stream fluids to the correlation

coefficient can be separated. The starting point is the decomposition of the velocity perturbation,

$$u' = \Gamma u^* + \Gamma\left(\overline{u}^B - \overline{u}\right) + (1-\Gamma)u'' + (1-\Gamma)\left(\overline{u}^F - \overline{u}\right). \tag{3.26}$$

The overall correlation coefficient can then be expressed as,

$$\begin{aligned} R_{u'u'}(\Delta x, \Delta z) &= \underbrace{\mathcal{C}_{u^*u^*} + \mathcal{C}_{(\overline{u}^B-\overline{u})(\overline{u}^B-\overline{u})} + 2\mathcal{C}_{u^*(\overline{u}^B-\overline{u})}}_{\text{boundary-layer contribution}} \\ &+ \underbrace{\mathcal{C}_{u''u''} + \mathcal{C}_{(\overline{u}^F-\overline{u})(\overline{u}^F-\overline{u})} + 2\mathcal{C}_{u''(\overline{u}^F-\overline{u})}}_{\text{free-stream contribution}} \\ &+ 2\mathcal{C}_{u^*u''} + 2\mathcal{C}_{(\overline{u}^B-\overline{u})(\overline{u}^F-\overline{u})} + 2\mathcal{C}_{u^*(\overline{u}^F-\overline{u})} + 2\mathcal{C}_{u''(\overline{u}^B-\overline{u})}, \end{aligned} \tag{3.27}$$

where $\mathcal{C}_{AB}$ is the conditional covariance between $A(x,y,z,t)$ and $B(x+\Delta x, y, z+\Delta z, t)$ normalized by $\overline{u'u'}$. Note that the terms involving the mean velocities, $\mathcal{C}_{(\overline{u}^B-\overline{u})(\overline{u}^B-\overline{u})}$, $\mathcal{C}^F_{(\overline{u}^F-\overline{u})(\overline{u}^F-\overline{u})}$ and $\mathcal{C}_{(\overline{u}^B-\overline{u})(\overline{u}^F-\overline{u})}$, do not contribute to the spanwise correlation since the mean flow is two dimensional. The correlation in the streamwise direction is plotted in figure 3.27(a), which compares the reference and forced cases at $y/\overline{y_I} \approx 0.55$. It also shows displays part of the contributions by the boundary-layer and free-stream fluctuations, $\mathcal{C}_{u^*u^*}$ and $\mathcal{C}_{u''u''}$ respectively. In addition to the general elongation of $R_{u'u'}$ in presence of forcing, the following observations are noteworthy: In the reference flow, $\mathcal{C}_{u^*u^*}$ makes up the majority of the correlation coefficient, and the free-stream term is relatively negligible. In presence of free-stream turbulence, $\mathcal{C}_{u^*u^*}$ and $\mathcal{C}_{u''u''}$ make commensurate contributions, and have similar streamwise lengths. Similar trends are observed along the spanwise direction in figure 3.27(b).

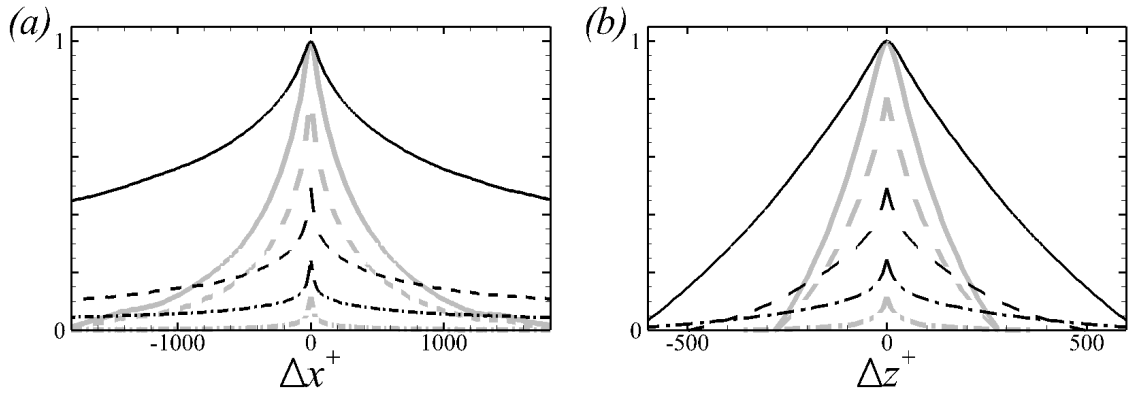

Figure 3.27: Two-point correlation at $y/\overline{y_I} \approx 0.55$. ($a$) $R_{u'u'(\Delta x,\Delta z=0)}$ and (b) $R_{u'u'(\Delta x=0,\Delta z)}$. (—) $R_{u'u'}$, (- - -) $\mathcal{C}_{u^*u^*}$ and (- · -) $\mathcal{C}_{u''u''}$. (Gray) REF; (black) FRC.

The large-scale coherent motions in the outer part of the boundary layer have a clear signature in the pre-multiplied energy spectra,

$$\kappa_z \Phi_{u'u'}(\lambda_z) = \kappa_z \int_{-\infty}^{\infty} \overline{u'(z)u'(z+\zeta)} e^{-i\kappa_z \zeta} \, d\zeta, \tag{3.28}$$

where κ_z and λ_z are the spanwise wavenumber and wavelength, respectively. Figure 3.28 compares $\kappa_z \Phi_{u'u'}(\lambda_z)$ in the reference and forced flows. In the former, a near-wall peak in the spectra is clearly visible. Only a faint trace of an outer peak is discernible in the logarithmic region, which is consistent with earlier simulations of canonical boundary layers [e.g. 76] and with the expectation that the outer peak only emerges at higher Reynolds numbers, $Re_\tau \geq 2000$ [35, 57]. When the boundary layer is subjected to free-stream vortical forcing, contours of the pre-multiplied spectra in the near-wall region and at small spanwise scales are largely unchanged; the minor shift towards smaller spanwise wavelengths is consonant with enhanced dissipation (c.f. figure 3.14). The contours, however, expand towards much larger spanwise wavelengths, which

motivated use of the wider simulation domain for this case. In addition, an outer peak in the spectra becomes clearly visible in figure 3.28. The associated contours span the logarithmic layer, starting from $y^+ = 100$ and extending to larger wall-normal positions in the boundary layer. The peak value is recorded at $y/\overline{y_I} \approx 0.55$, or $y/\delta_{99} \approx 0.4$ which is consistent with Hearst et al. [31]. The corresponding disturbances have a spanwise wavelength $\lambda_z/\overline{y_I} \approx 3.0$.

Note that previous experiments reported the outer-peak in the pre-multiplied *streamwise* spectra, at wavelengths in the range from $\lambda_x/\delta_{99} = 6$ to 19 [31, 77]. In order to verify our findings, we evaluated the pre-multiplied frequency spectra (not shown) which requires a long time series for convergence. Taylor's hypothesis was subsequently invoked using the local advection velocity to convert the frequency into streamwise wavelength, and an outer peak was observed at $\lambda_x/\delta_{99} \approx 10$.

The present findings complement the work by Hearst et al. [31], who analyzed the pre-multiplied spectral map in boundary layers beneath free-stream forcing. They too observed that the inner smaller-scale spectral peak is not altered by the forcing, while the large scales are dependent on the free stream. They argued that only the low-frequency portion of the free-stream turbulence can permeate the boundary layer towards the wall. Spectra, however, involve contributions from both the direct penetration of free-stream fluid inside the mean shear and the boundary layer response. Our conditional sampling results provide the necessary direct evidence of the extent of penetration of free-stream turbulence towards the wall: The average

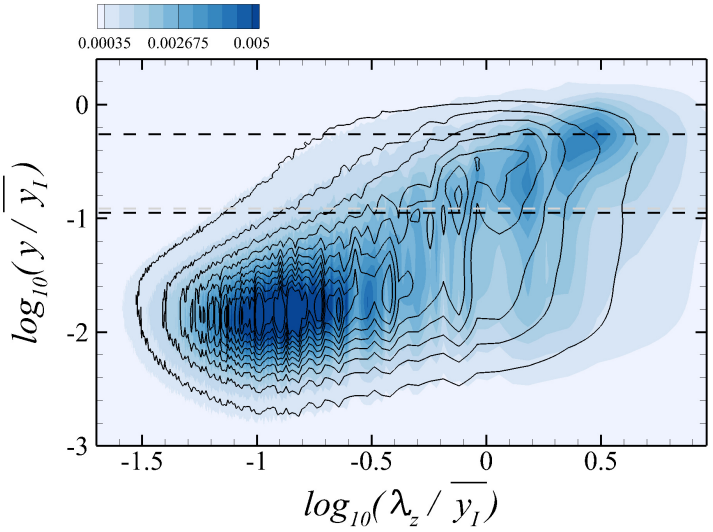

Figure 3.28: One-dimensional pre-multiplied energy spectra, $\kappa_z \Phi_{u'u'}(\lambda_z)$, at $Re_\theta = 3000$ in (line contour) REF and (flood contour) FRC. The lower dashed line marks $y^+ = \{90, 100\}$ in the REF and FRC, and the upper dashed line marks $y/\overline{y_I} = 0.55$.

intermittency profiles (figure 3.11) give the probability of observing free-stream fluid at different heights in the boundary layer; and the conditional two-point correlation (figure 3.26*b*), which only samples free-stream fluid inside the boundary layer, directly demonstrates shear filtering of the high-frequency components.

While free-stream perturbations can breach the outer part of the boundary layer and directly impact the turbulence in the logarithmic region, they do not reach the buffer layer (c.f. figure 3.11). As such, their role in enhancing the Reynolds shear and normal stresses, in and below the buffer layer, must be indirect. One possibility is that the spawned energetic large-scale motions in the log layer modulate the near-wall flow – an effect that can be assessed by evaluating the amplitude modulation (AM) coefficient. Mathis et al. [57] defined a local AM coefficient as the one-point

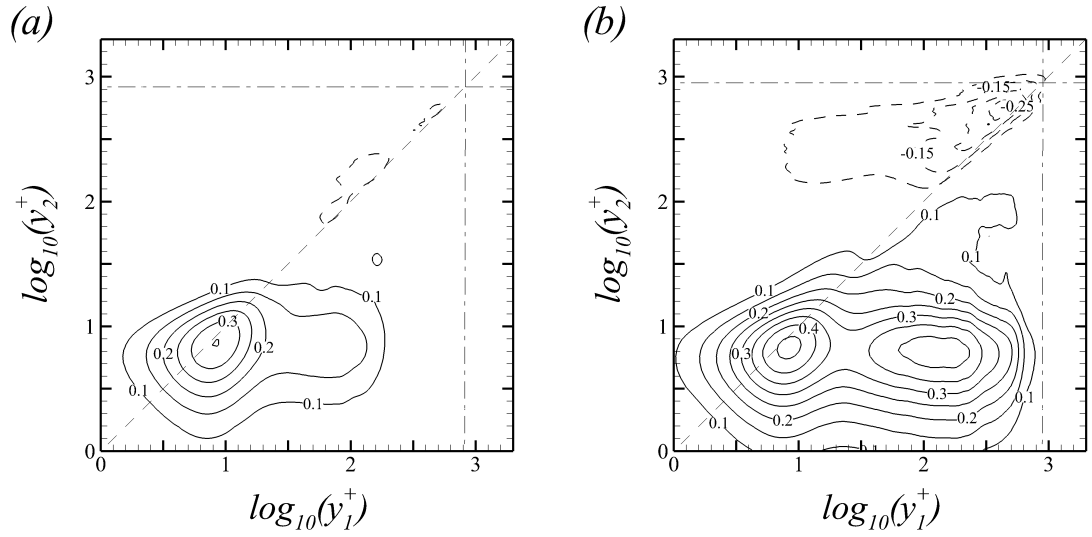

Figure 3.29: Amplitude modulation coefficient, $C^{2p}_{u,u}$, normalized by u_τ^2 at $Re_\theta = 3000$. (a) REF and (b) FRC. Negative contours are plotted with dashed lines; Dashed-dot lines (- · -) indicate $y/\overline{y_I} = 1$. Increments of contour levels are 0.05.

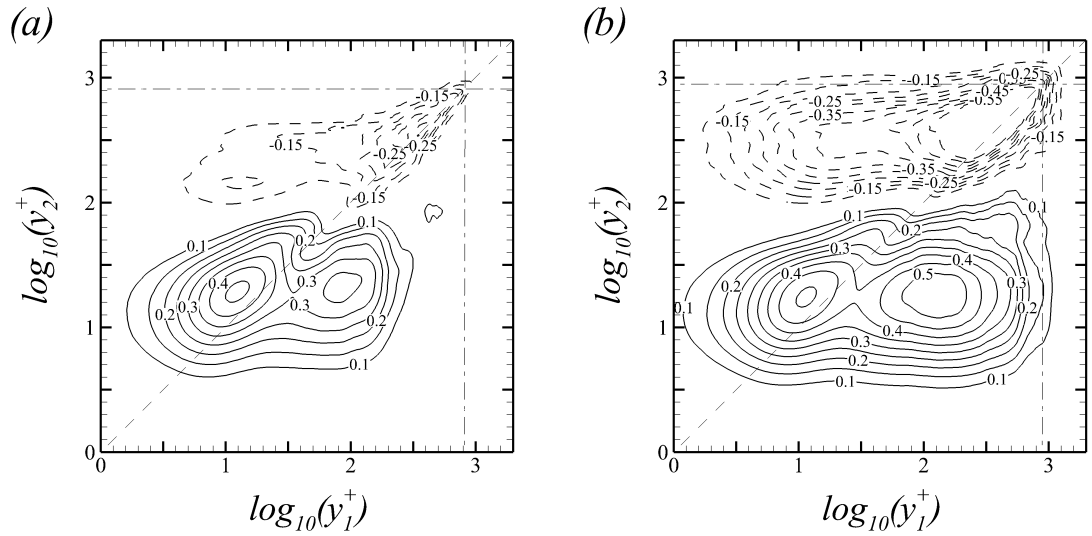

Figure 3.30: Amplitude modulation coefficient, $C^{2p}_{u,uv}$, normalized by u_τ^3 at $Re_\theta = 3000$. (a) REF and (b) FRC. Negative contours are plotted with dashed lines; Dashed-dot lines (- · -) indicate $y/\overline{y_I} = 1$. Increments of contour levels are 0.05.

correlation between a large-scale velocity, u'_L, and a filtered envelope of a small-scale part, u'_{EL}. The definition was extended by Bernardini and Pirozzoli [9] who computed the two-point AM coefficient as the covariance between u'_L at position y_1 and u'_{EL} at position y_2,

$$C^{2p}_{u,u}(y_1, y_2) = \overline{u'_L(y_1)u'_{EL}(y_2)}. \tag{3.29}$$

Iso-contours of $C^{2p}_{u,u}/u^2_\tau$ are plotted in figure 3.29. In the canonical boundary layer, a emergent positive peak in the bottom-right side of the contour plot of figure 3.29(a) indicates that large-scale motions at $y_1^+ \approx 80$ modulate the small scales at $y_2^+ \approx 8$. In the forced case, that peak becomes more distinct, occupies a wider area and is stronger (figure 3.29(b)). Its wall-normal height is also farther away from the wall, and is consistent with the outer peak in the pre-multiplied energy spectra (figure 3.28). The larger AM coefficient indicates that, when the boundary layer is forced, the resulting coherent motions in the logarithmic layer modulate, and thus enhance, the near-wall structures. As a result, $\overline{u'u'}$ increases in the buffer region, where the direct free-stream contribution to the stresses is negligible (c.f. figure 3.17(b)).

In order to evaluate the influence of the large energetic structures in the logarithmic layer u'_L on the near-wall Reynolds shear stress $(u'v')_{EL}$, we define,

$$C^{2p}_{u,uv}(y_1, y_2) = \overline{u'_L(y_1)(-u'v')_{EL}(y_2)}. \tag{3.30}$$

Iso-contours of $C^{2p}_{u,uv}/u^3_\tau$ are plotted in figure 3.30, and support a similar interpretation as $C^{2p}_{u,u}$: The peak in the AM coefficient shifts to a higher wall-normal location when

the boundary layer is forced by free-stream vortical perturbation. More importantly, its value increases from $C^{2p}_{u,uv} \approx 0.37$ to 0.54, which is indicative of a more pronounced modulation of near-wall Reynolds shear stress by the outer u' large-scale structures. Also note that the modulated site in the contours of $C^{2p}_{u,uv}$ is higher than the corresponding point in $C^{2p}_{u,u}$, namely $y_2^+ \approx 20$ versus $y_2^+ \approx 8$. This shift is consistent with the mean Reynolds stresses, where the peak position of $-\overline{u'v'}$ is higher than that of $\overline{u'u'}$ as shown in figure 3.17.

Viewed all together, the present results indicate that the low-frequency free-stream vortical perturbations directly force the boundary layer in logarithmic layer and lead to the amplification of energetic large-scale motions. These structures modulate the near-wall Reynolds stresses, far below the extent of penetration of free-stream turbulence. The Reynold shear stresses in the buffer layer thus enhance the production of $\overline{u'u'}$ which is also modulated by the outer structures. The increase in production is balanced by an increase in dissipation at the wall. In addition, in a frame moving with the free stream, the higher production of wall turbulence necessitates an increased power input into the wall to move it at a constant speed, $-U_\infty$, and hence drag is increased.

Designation	HIT Tu, L_k, Re_λ	Domain size (θ_{in}) $L_x \times L_y \times L_z$	No. of Grid points $N_x \times N_y \times N_z$
FRC-S	10%, $7.4\theta_{in}$, 85	$1000 \times 80 \times 80$	$5760 \times 768 \times 768$

Table 3.2: Summary of domain information and FST properties at inlet.

3.6 Free-stream turbulence with smaller lengthscale

In this section, we summarize an additional simulation, which is designated 'FRC-S' and where the boundary layer is subjected to free-stream forcing with the same intensity but smaller lengthscale relative to FRC. Properties of the free-stream turbulence, and the computational domain size and grid resolution are listed in table 3.2. The lengthscale at the inlet is approximately 30% smaller in FRC-S, or precisely $L_k = 7.4\theta_{in}$. Comparisons of its downstream evolution in FRC-S and FRC, as well as the evolutions of Tu and β, are provided in figure 3.31. Due to the smaller lengthscale, the turbulence intensity decays more rapidly in FRC-S and, while the Hancock parameter β is initially higher for the new computation, it is smaller throughout the majority of the domain due to the faster decay in Tu. The same data is visualized in figure 3.31*c*, which shows the trajectory of the free-stream turbulence in the space of L_u/δ_{99} and Tu.

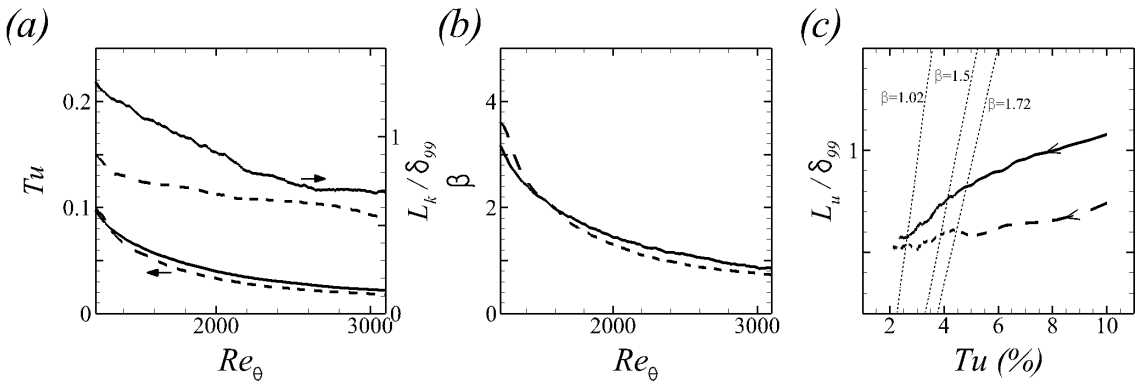

Figure 3.31: Downstream evolutions of (a) Tu and L_k and (b) β. (c) L_u/δ_{99} versus Tu, and dotted lines mark constant β [29]. (—) FRC; (- - -) FRC-S

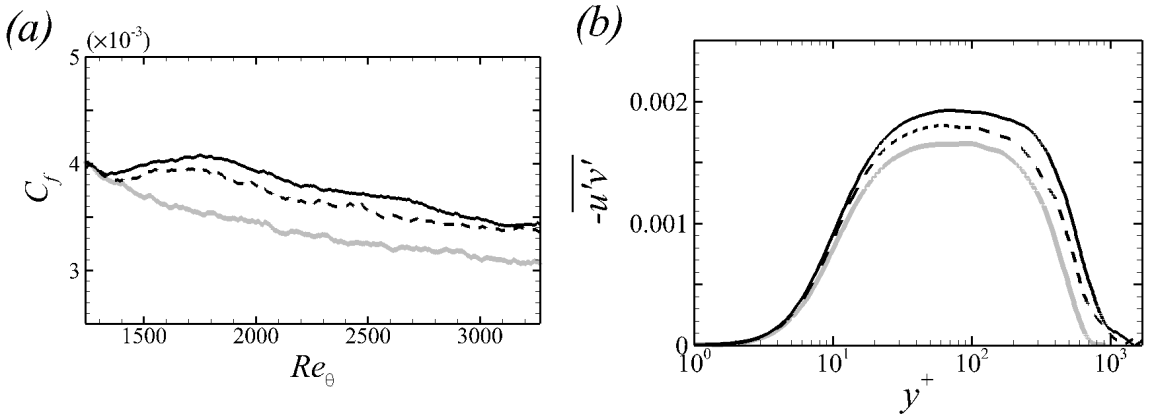

Figure 3.32: (a) Skin-friction coefficients, C_f. (b) Reynolds shear stress, $-\overline{u'v'}$ at $Re_\theta = 1900$. (Gray) REF; (black solid line) FRC; (black dashed line) FRC-S.

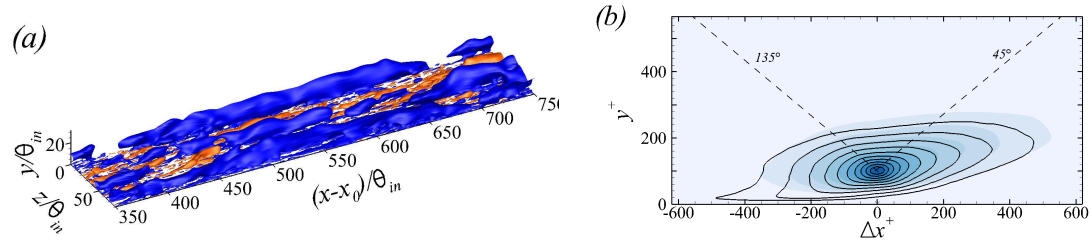

Figure 3.33: (a) Instantaneous iso-surfaces of the Gaussian-filtered velocity $\hat{u}' = \pm 0.06$ in FRC-S. (b) Side view of contours of $R_{u'u'}$ at $y^+_{ref} = 100$ and $Re_\theta = 3000$. (lines) FRC-S; (flood) FRC.

The skin-friction coefficient is reported in figure 3.32a. While it is larger in FRC-S relative to the reference boundary layer, its increase is not as pronounced as in FRC as anticipated since β is generally reduced. In §3.4, the change in C_f was ascribed primarily to enhanced dissipation in the distorted mean-velocity profile and to a higher rate of turbulence production, and both effects were related to $-\overline{u'v'}$. The Reynolds shear stress is plotted in figure 3.32b and, congruent with C_f, monotonically increases from REF to FRC-S and finally to FRC.

Whether outer large-scale motions are amplified depends on the low-frequency content of the free-stream forcing. By reducing L_k in case FRC-S, that content is reduced and the energy that is available to perturb the boundary layer is weaker. It was also shown by Nagata et al. [60] that for very small L_k/δ, while skin-friction is enhanced, large-scale motions are not formed in the boundary layer. Their free-stream lengthscale was, however, smaller than the smallest one considered here, and their turbulence intensity was also weaker. The energetic structures in the outer part of the boundary layer are visualized in figure 3.33a using the Gaussian-filtered flow field. Similar to figure 3.22, we note the formation of coherent streamwise velocity structures in the logarithmic layer, which were shown to play an important role in modulating the near wall streamwise and shear stress (§3.5). The size of these structures is examined in figure 3.33b using the two-point correlation, and is commensurate in FRC-S and FRC despite the 30% reduction in L_k at the inlet plane. It can therefore be concluded that, even at the smaller free-stream lengthscale considered here, sufficient energy is

available in the low-frequency component of the forcing turbulence to trigger the amplification of outer large-scale energetic structures in the boundary layer.

3.7 Conclusion

Direct numerical simulations of turbulent boundary layers beneath quiescent and vortical free streams were performed. In the forced case, the free-stream turbulence is homogeneous and isotropic, and its intensity and integral length scale are $Tu = 10\%$ and $L_k \approx 10.8\theta_{in}$, respectively, at the inflow plane and decays downstream. In order to perform conditional sampling, a technique is sought to distinguish the boundary-layer and free-stream fluids. Conventional methods which are based on a vorticity threshold are not applicable when the free stream is vortical. Instead, a level set interface capturing approach was adopted in order to differentiate the fluids which, at the inlet, belong to the boundary layer and to the free stream, and to perform conditional sampling.

When the free stream is turbulent, the skin-friction coefficient increased by up to 15% relative to the reference flow within the simulated Reynolds-number range (figure 3.12). This effect is interpreted from the perspective of the power required to move the wall with speed $-U_\infty$ in a stationary fluid, which leads to three contributions: the dissipation due to the established mean-flow profile, the acceleration of the base flow, and the production of turbulent kinetic energy. The final contribution is most

sensitive to external forcing, and increases appreciably even closer to the wall than the depths to which external vortical perturbations effectively enter the boundary layer.

In the forced flow, the mean streamwise velocity profile shows a depression in the wake region which is consistent with the increased drag. In contrast, the log-law behaviour remains robust, and persists not only in the conventional mean but also in the conditional profiles. With the intermittency weighting, the free-stream contribution to the mean velocity decays slower in the boundary layer than in the reference case, but nonetheless becomes negligible within the logarithmic region. The vortical forcing also enhances all components of the Reynolds stress (figure 3.17), including the shear stress even though the forcing turbulence is itself free of $\overline{u'v'}$. In addition, even though the conditional free-stream contribution vanishes in the near-wall region, the stresses especially $\overline{u'u'}$ increase throughout the buffer layer. This increase, chiefly due to the boundary-layer contribution, can not be ascribed to any transport of turbulence kinetic energy from the free stream since the conditional statistics are based on the level set function which is a material line.

The increase in the Reynolds stresses is the statistical outcome of changes in the structures within the boundary layer, when exposed to free-stream forcing. In the outer logarithmic region, large-scale energetic structures become evident in the instantaneous perturbation fields (figure 3.22). Their extents in the spanwise and streamwise directions are larger than those observed in the reference flow below a

quiescent free stream. The spanwise size is, nonetheless, commensurate with the lengthscale of the free-stream turbulence, which was selected to be on the order of the boundary layer thickness. On the other hand, the streamwise extent of these large-scale structures is much longer, which was explained by demonstrating the ability of the boundary layer to low-pass filter the free-stream perturbations. A clear signal of these structures is recorded as an outer peak in the pre-multiplied energy spectra.

Once the outer large scale motions are established within the boundary layer, they evolve on a long timescale during which the flow advects many streamwise characteristic lengths. As such, we anticipate they will long outlive the decay of the free-stream turbulence. Much longer domains, perhaps using large-eddy simulations or experiments, would be required to quantify this effect.

Unlike the amplification of the outer coherent structures in the log layer which is a direct response to free-stream forcing, the appreciable increase in the near-wall stresses takes place in a region where the free-stream conditional contributions are vanishingly small. An explanation is put forward where the outer large-scale motions modulate the near-wall shear and streamwise normal stresses (figures 3.29-3.30), and is demonstrated by evaluating the two-point amplitude modulation coefficients. The enhanced shear stresses also lead to higher production of turbulence kinetic energy in the buffer layer and, as a result, drag.

Another configuration with similar inlet free-stream intensity and a 30% smaller lengthscale $L_k \approx 7.4\theta_{in}$ is also examined in this chapter. Due to the faster downstream

decay of the turbulent intensity, the increase in the Reynolds stresses and skin-friction coefficient are less pronounced. The outer peak in the pre-multiplied energy spectra is also observed in the smaller lengthscale case since the high-frequency content of FST is filtered inside the boundary layer while longer waves persist. The next chapter addresses the statistical and dynamical changes in the thermal boundary layer exposed to the free-stream vortical forcing.

Chapter 4

Turbulent heat-transfer enhancement in boundary layers exposed to free-stream turbulence

4.1 Introduction

The canonical turbulent boundary layer (TBL) description assumes that the free-stream is quiescent, without any background disturbances. In engineering applications, however, the free stream is often vortical and can modify both the hydrodynamic and thermal characteristics of wall turbulence, the latter being the focus of this study. Using direct numerical simulations (DNS), the interaction of inflow homogeneous isotropic turbulence (HIT) with a zero-pressure-gradient TBL on a heated

plate is examined. Both the statistical and structural changes in the thermal field are evaluated and their origins are traced back to the influence of the free-stream forcing.

Previous experiments examined the response of turbulent boundary layers to grid-generated HIT with intensity less than 7% [11, 78]. The main interests were the changes in skin friction and in heat-transfer rate, and how they relate to the properties of the external disturbances. Simonich and Bradshaw [78] reported that both heat transfer and drag are directly proportional to the free-stream turbulence intensity: they increase by 2% and 5%, respectively, relative to the canonical TBL when the turbulence intensity increases by 1%. Hancock and Bradshaw [28] attempted to capture the influence of HIT intensity and lengthscale on skin friction by introducing a parameter $\beta \equiv \frac{u'/U_\infty}{L_u/\delta+2}$, where L_u and δ are the dissipation lengthscale and boundary-layer thickness. Blair [11] correlated the Hancock parameter to the increase in heat-transfer rate.

The influence of more energetic vortical forcing of the boundary layer was also examined. For example, free-stream turbulence intensities greater than 10% from gas turbine combustors [2] and high-velocity cross jets [55, 80, 81] were considered. At these levels of forcing, much larger increase in heat transfer was observed: Maciejewski and Moffat [55] reported that 60% free-stream turbulence intensity led to the four folds increase in the heat-transfer rate, although the forcing in this case was anisotropic. Thole and Bogard [80] demonstrated that the Hancock parameter, β, can accurately predict the change in drag up to $Tu = 28\%$. However, the TLR parameter

proposed by Ames and Moffat [2] ($TLR \equiv Tu(\Delta_2/L_u)^{0.33}(Re_{\Delta_2}/1000)^{0.25}$ where Δ_2 is the enthalpy thickness) was more successful for predicting the increase in the mean Stanton number.

In addition to the above experimental studies, Péneau et al. [68] and Li et al. [50] performed large-eddy simulations (LES) of free-stream vortical forcing of turbulent boundary layers. In the former study, the external disturbances were a random superposition of Oseen vortices [68], and in the latter a superposition of Orr-Sommerfeld and Squire eigenfunctions [50]. Péneau et al. [68] reported that the thermal field was more sensitive to the free-stream turbulence than the hydrodynamic one. For example, the logarithmic layer of the mean-temperature profile was appreciably influenced by the presence of free-stream turbulence, while the velocity profile was hardly affected. They reported a 40% increase in heat transfer relative to the unforced flow; it should be noted however that their mean Stanton number increased by 30% at the inlet to their computational domain due to numerical issues. In addition, their domain size was limited in streamwise extent ($1200 < Re_\theta < 1500$). Li et al. [50] started their computation at a lower Reynolds number, and their domain spanned the range $100 < Re_\theta < 1000$. They imposed thermal perturbations in the free stream and, contrary to Péneau et al. [68], reported that the logarithmic region in the temperature profile was not affected by the presence of the external forcing. Li et al. [50] also reported two distinct peaks in the pre-multiplied spectra of thermal fluctuations, which is a similar observation to the one made in connection with the spectra of

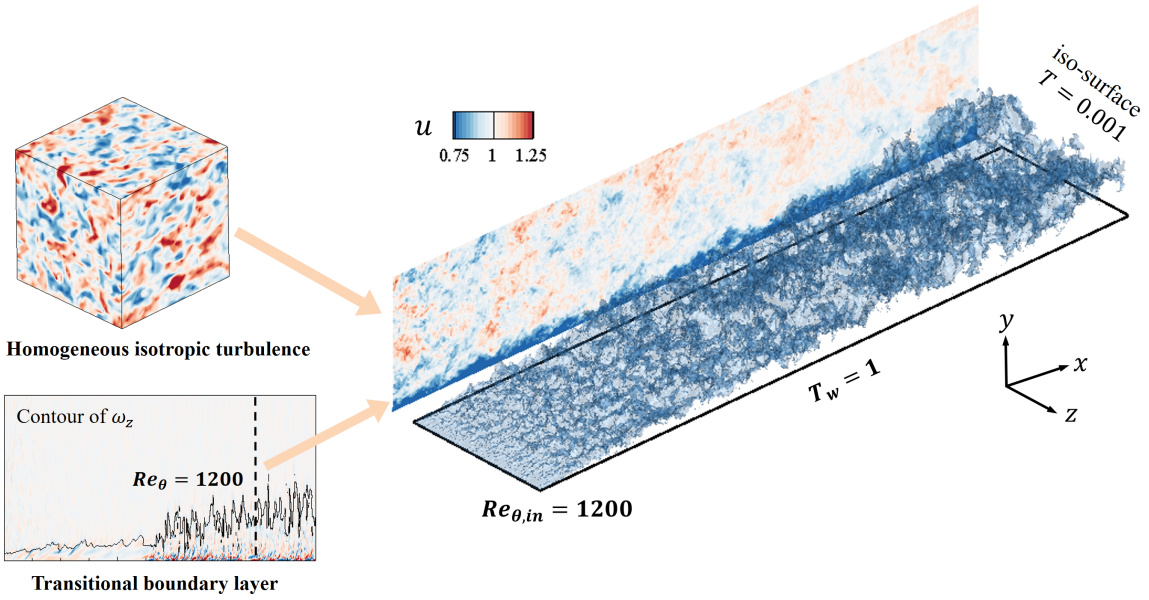

Figure 4.1: Schematic of the flow configuration showing the inflow condition and the thermal boundary layer developing beneath free-stream turbulence.

streamwise velocity fluctuations in their own study and in experiments [20, 77, 81]. The outer peaks in the pre-multiplied spectra of thermal and velocity fluctuations are indicative of the formation of large-scale thermal and hydrodynamic structures, respectively, in the outer region of the boundary layer. A fully resolved simulation that examines the effect of free-stream vortical forcing on the thermal boundary layer at $Re_\theta > 1500$ is therefore absent from the literature.

The increase in turbulence kinetic energy in the near-wall region of forced boundary layers is well documented experimentally and numerically. Using multipoint measurements, Dogan et al. [21] argued that the increase is due to the direct penetration of the free-stream turbulence towards the wall. In §3, we also investigated HIT interact-

ing with an underlying spatially developing boundary layer, with Reynolds numbers exceeding $Re_\theta = 3200$.

Previous efforts have focussed on the impact of external forcing on skin friction and wall turbulence. And while the increase in the rate of heat transfer is established, the changes in the thermal boundary layer have received relatively less scrutiny; for example prior work has not drawn a connection between the large-scale hydrodynamic motions that emerge in response to the forcing and the modifications to the thermal structures. The present study focusses on the statistical and dynamical changes in the thermal boundary layer that accompany the increase in the heat-transfer rate and, where possible, will draw a connection to the changes in the boundary-layer turbulence. A schematic of the computational domain is shown in figure 4.1. Two cases are considered: a reference configuration where a zero-pressure-gradient turbulent boundary layer develops on a heated wall below a quiescent free stream, and in the second the flow is exposed to HIT with 10% intensity at the inlet plane.

This chapter is organized into five sections: The details of the simulations are described in section 2. In section 3, the increase in boundary-layer heat transfer due to HIT is quantified, various contributions to the mean Stanton number St are reported, and relevant flow statistics are examined. In section 4, the changes in the thermal structures inside the boundary layer in the forced simulation are discussed, and conclusions are provided in the last section.

4.2 Simulation setup

The flow configuration is shown in figure 4.1. Two main simulations are considered: The first is the reference case (REF), where a zero-pressure-gradient boundary layer evolves over a heated isothermal flat plate without any external forcing. The second case is forced (FRC), where in addition to the boundary layer, isotropic turbulence is introduced in the free stream; note that the forcing does not include thermal fluctuations. Convective outflow conditions are imposed for both the velocity and temperature at the exit planes of the computational domains. At the bottom isothermal wall, no-slip boundary conditions are imposed. At the top boundary, a distribution of suction velocity is dynamically controlled in order to maintain zero pressure gradient on the plate, even in presence of high levels of perturbations (§3.2.2). The flow domains are periodic in the spanwise direction.

The computational parameters are summarized in table 3.1. At the inlet, realistic inflow TBL and HIT are introduced (§2.2). In order to avoid interference with the boundary-layer turbulence at the inlet plane, the HIT was introduced within the irrotational flow region beyond the boundary-layer edge (see §3.3). The downstream evolutions of the intensity and lengthscale of the HIT in the main forced simulation, above the turbulent boundary layer, are provided in figure 3.2. Note that the HIT was only comprised on hydrodynamic fluctuations, and void of thermal perturbations.

4.3 Modification of boundary-layer scalar statistics by free-stream turbulence

4.3.1 Hydrodynamic and thermal thicknesses

Comparison of the reference and forced boundary layers will be performed at the same enthalpy thickness Reynolds numbers $Re_{\Delta_2} \equiv U^*_\infty \Delta^*_2/\nu^*$, where the enthalpy thickness is defined as $\Delta^*_2 \equiv \int_0^\infty \frac{\overline{u^*}}{U^*_\infty}\left(\frac{\overline{T^*}-T^*_\infty}{T^*_w-T^*_\infty}\right) dy^*$. The downstream variation of Re_{Δ_2} is plotted in figure 4.2*a*. Since the wall heating is applied suddenly at the start of the domain, Re_{Δ_2} starts from zero and the thermal boundary-layer approximation is not applicable at that location. However, the errors in that approximation become negligible beyond $Re_{\Delta_2} = 200$; the results presented herein will focus on larger Re_{Δ_2} where the boundary-layer approximation is valid. Despite the different domain lengths, the Reynolds numbers of both simulations exceed $Re_{\Delta_2} = 3200$ before the exit planes. The momentum thickness Reynolds numbers exceed $Re_\theta = 3500$ in the canonical boundary layer and $Re_\theta = 3200$ in presence of free-stream turbulence. Hereafter, gray and black lines always indicate results from the reference and forced configurations, respectively.

The downstream development of the 99% momentum boundary-layer thickness δ_{99} is plotted in figure 4.2*b*. The figure also shows the 99.9% thermal boundary-layer thickness δ_T. The two thicknesses become comparable to one another at $Re_{\Delta_2} = 900$,

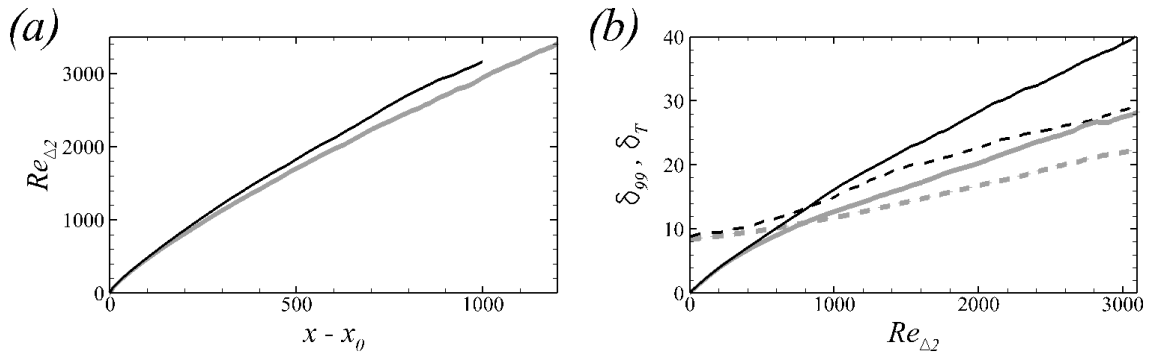

Figure 4.2: Downstream dependence of (a) enthalpy thickness Reynolds number Re_{Δ_2} and (b) the boundary-layer thicknesses: (—) δ_T and (- - -) δ_{99}. (Gray) REF; (black) FRC.

and hence this position is selected for comparison of the reference and forced flows. A farther downstream location, $Re_{\Delta_2} = 2700$, is also considered, where the thermal thickness far exceeds the hydrodynamic one and includes part of the free-stream flow field. In the forced boundary-layer simulation, the free-stream turbulence intensity at these two locations is $Tu = 5.0\%$ and 2.4%.

4.3.2 Stanton number

When the TBL is exposed to external forcing, both the wall-shear stress and the heat-transfer rate are enhanced. The increase of the former was explained in §3.4.1 which provided a detailed account for the contributions to the skin-friction coefficient. The focus here is placed on the mean rate of heat transfer at the wall $\overline{q_w}$, or in non-dimensional form the mean Stanton number,

$$St \equiv \frac{\overline{q_w^*}}{\rho^* U_\infty^* c_p^* (T_w^* - T_\infty^*)} = -\frac{1}{Pe} \frac{\partial \overline{T}}{\partial y}\bigg|_{y=0} \tag{4.1}$$

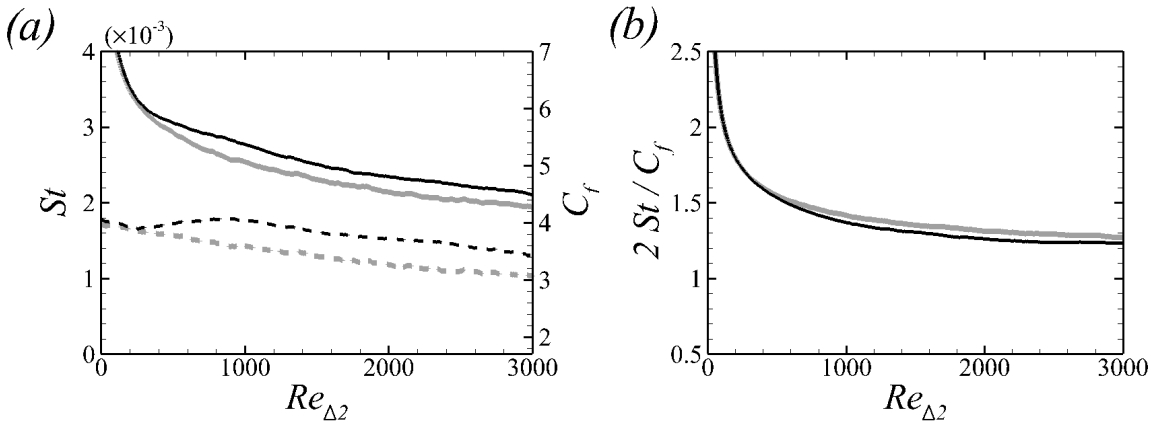

Figure 4.3: Downstream evolution of (a) (—) mean Stanton number St and (- - -) skin-friction coefficient C_f, and (b) Reynolds analogy factor $2St/C_f$. (Gray) REF; (black) FRC.

where c_p^* is the specific heat. Figure 4.3 shows that, at $Re_{\Delta_2} = 900$, the rate of heat transfer is increased by 10% in the forced flow relative to a canonical turbulent boundary layer, and the increase is maintained downstream. The simultaneous increase in skin friction, however, leads to a nearly unchanged evolution of the Reynolds analogy factor $2St/C_f$.

Top views of instantaneous Stanton number, st, are shown in figure 4.4. The increase in the rate of heat transfer at the wall can be associated with an expansion of the high-st regions and/or an increase in the extrema of st. The figure qualitatively captures the former effect, where the area of high st is much wider in the forced flow compared to the reference case. A quantitative assessment is provided by the weighted probability density function (P.D.F.) of st in figure 4.5. The peak of the curve shifts to higher st when the boundary layer is exposed to free-stream forcing, and there is higher likelihood, or larger regions, of high st. For example, at $st = 0.005$, the

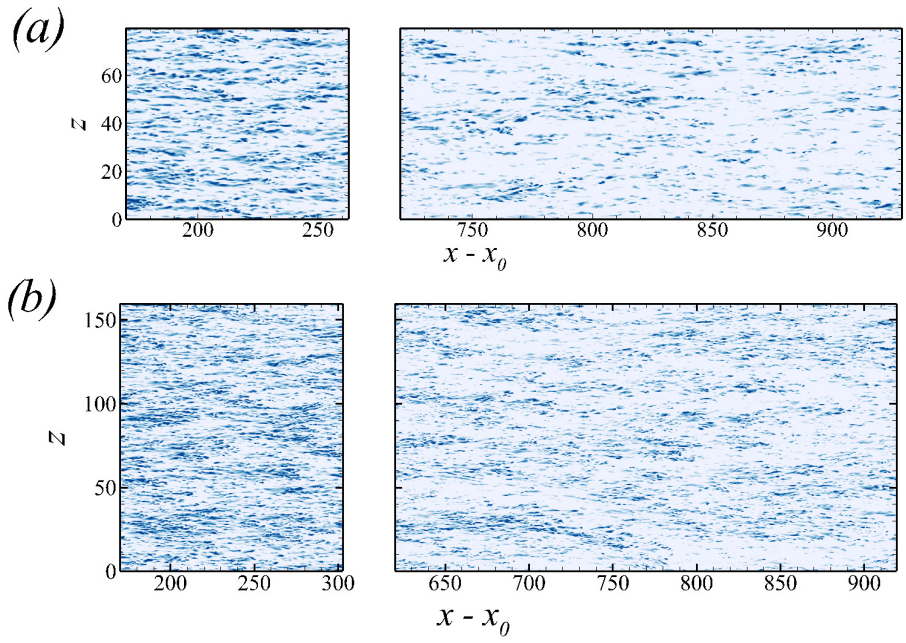

Figure 4.4: Contours of instantaneous Stanton number, $0.0025 \leq st \leq 0.005$. ($a$) REF; ($b$) FRC.

weighted PDF of the forced case is 53% larger than the reference flow at $Re_{\Delta_2} = 900$, and 90% larger at $Re_{\Delta_2} = 2700$.

The increase in St can be related to changes in the base-temperature profile and also turbulence statistics, using a similar decomposition to the one introduced by Renard and Deck [71] for the skin friction coefficient C_f. That approach was successfully adopted in §3.4.1 to relate the increase in C_f is due to enhanced rate of dissipation of mean streamwise kinetic energy and of the rate of production of turbulence kinetic energy. A thermal boundary-layer approximation is invoked in the derivation, and therefore the decomposition is only applicable where that approximation is valid. The

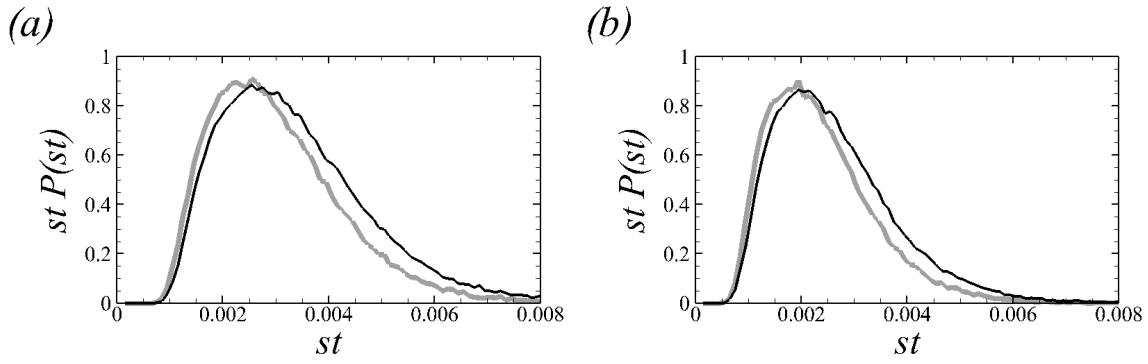

Figure 4.5: Weighted P.D.F. of the instantaneous Stanton number, $st\ P(st)$. (a) $Re_{\Delta_2} = 900$ and (b) $Re_{\Delta_2} = 2700$. (Gray) REF; (black) FRC.

mean temperature $\overline{T}$ is governed by the advection-diffusion equation,

$$\frac{\partial \overline{u}\overline{T}}{\partial x} + \frac{\partial \overline{v}\overline{T}}{\partial y} + \frac{\partial \overline{u'T'}}{\partial x} + \frac{\partial \overline{v'T'}}{\partial y} \;=\; \frac{1}{Pe}\left\{\frac{\partial^2 \overline{T}}{\partial x^2} + \frac{\partial^2 \overline{T}}{\partial y^2}\right\}. \tag{4.2}$$

Beyond a small region near the inlet of the domain, the thermal boundary-layer approximation becomes valid and therefore,

$$\frac{\partial \overline{u}\overline{T}}{\partial x} + \frac{\partial \overline{v}\overline{T}}{\partial y} = \frac{\partial}{\partial y}\left(\frac{1}{Pe}\frac{\partial \overline{T}}{\partial y} - \overline{v'T'}\right). \tag{4.3}$$

Equation (4.3) is then multiplied by $\overline{T}$, and integrated from $y = 0$ to infinity,

$$\begin{aligned}\int_0^\infty \overline{T}\left(\frac{\partial \overline{u}\overline{T}}{\partial x} + \frac{\partial \overline{v}\overline{T}}{\partial y}\right)\, dy \;&=\; -T_w \frac{1}{Pe}\frac{\partial \overline{T}}{\partial y}\bigg|_{y=0} - \int_0^\infty \frac{1}{Pe}\left(\frac{\partial \overline{T}}{\partial y}\right)^2 dy \\ &\quad + \int_0^\infty \overline{v'T'}\frac{\partial \overline{T}}{\partial y}\, dy.\end{aligned} \tag{4.4}$$

The first term on the right-hand side is proportional to the mean Stanton number, $St = -\frac{1}{Pe}\left(\partial \overline{T}/\partial y\right)_{y=0}$. Equation (4.4) is then divided by T_w and rearranged,

$$St \;=\; \underbrace{\frac{1}{T_w}\int_0^\infty \frac{1}{Pe}\left(\frac{\partial \overline{T}}{\partial y}\right)^2 dy}_{St_a} + \underbrace{\frac{1}{T_w}\int_0^\infty -\overline{v'T'}\frac{\partial \overline{T}}{\partial y} dy}_{St_b} \tag{4.5}$$

$$+\underbrace{\frac{1}{T_w}\int_0^\infty \overline{T}\left(\frac{\partial \overline{u}\overline{T}}{\partial x}+\frac{\partial \overline{v}\overline{T}}{\partial y}\right)dy}_{St_c}.$$

In terms of the temperature deficit, $\Theta \equiv (T^* - T_w^*)/(T_\infty^* - T_w^*) = 1 - T$, the decomposition becomes,

$$St = \underbrace{\frac{1}{1-\Theta_w}\int_0^\infty \frac{1}{Pe}\left(\frac{\partial \overline{\Theta}}{\partial y}\right)^2 dy}_{St_a} + \underbrace{\frac{1}{1-\Theta_w}\int_0^\infty -\overline{v'\Theta'}\frac{\partial \overline{\Theta}}{\partial y}dy}_{St_b} + \underbrace{\frac{1}{1-\Theta_w}\int_0^\infty \left(\overline{\Theta}-1\right)\left(\frac{\partial \overline{u}\overline{\Theta}}{\partial x}+\frac{\partial \overline{v}\overline{\Theta}}{\partial y}\right)dy}_{St_c}. \tag{4.6}$$

In equation (4.6), St_a is the rate of thermal dissipation due to the mean-temperature gradient; St_b is the rate of production of the thermal variance $\overline{\Theta'\Theta'}$; and St_c is due to the advection of heat into the flow. Figure 4.6*a* presents the evolutions of the coefficients calculated from the wall-normal scalar flux and the decomposition (4.6) as a function of Re_{Δ_2}. The figure shows a good agreement between the coefficients computed in a different way.

The decomposition (4.6) is verified within the region of validity of the thermal boundary-layer approximation ($Re_{\Delta_2} \geq 200$) in figure 4.6*a*, where the sum of the three contributions is shown to reproduce the total St. Each term is plotted separately in figure 4.6*b*, normalized by the mean Stanton number from the reference TBL simulation, $St_{REF}(Re_{\Delta_2})$. The results demonstrate that the total heat-transfer rate is primarily comprised of St_a and St_b, while St_c is relatively smaller. In addition, the enhanced rate of heat transfer in the forced flow is due to the increase in the first two terms. Common to both term is the importance of the wall-normal scalar

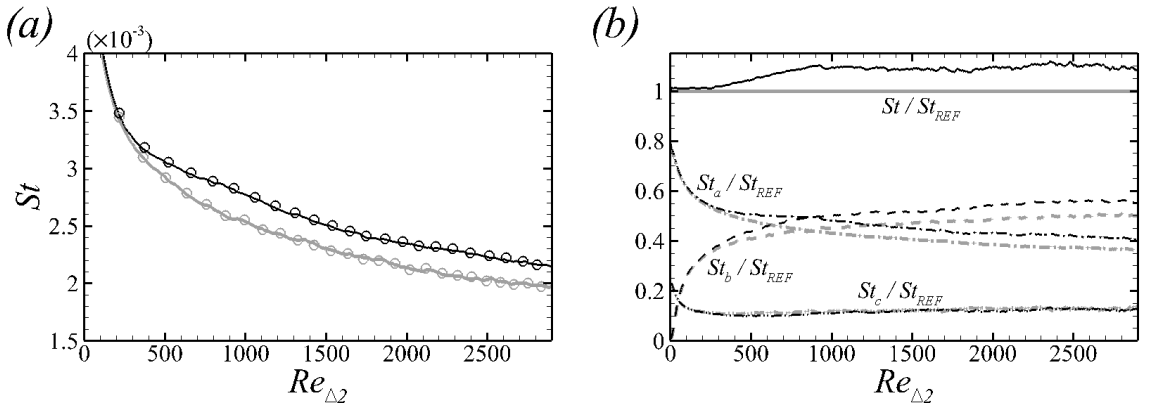

Figure 4.6: (a) Mean Stanton numbers computed from (—) the heat flux at the wall (equation 4.1) and from (◯) the decomposition (4.6). (b) Contributions to the mean Stanton number normalized by St_{REF}; (—) St, (- · -) St_a, (- - -) St_b and (- · · -) St_c. (Gray) REF; (black) FRC.

flux $\overline{v'\Theta'}$, which distorts the base-temperature profile in St_a and directly appears in the production term St_b. The following discussion will therefore focus on St_a and St_b. Regarding St_c, we only note that the wall-normal integral of the advection term alone increases in the forced flow, but its weighting by $\left(\overline{\Theta}-1\right)$ ultimately causes the integral to be inappreciably changed from the reference case.

4.3.3 Distortion of the mean-temperature profile

Profiles of the mean temperature deficit at $Re_{\Delta_2} = \{900, 2700\}$ are plotted in figure 4.7. In the top panels, they are normalized by the local friction temperature $\Theta^*_\tau \equiv \overline{q^*_w}/(\rho^* c^*_p u^*_\tau)$. In presence of HIT, the profiles are suppressed in the outer region, which is indicative of enhanced rate of heat transfer. At $Re_{\Delta_2} = 900$, the modification persists within the logarithmic layer, even though the velocity profile

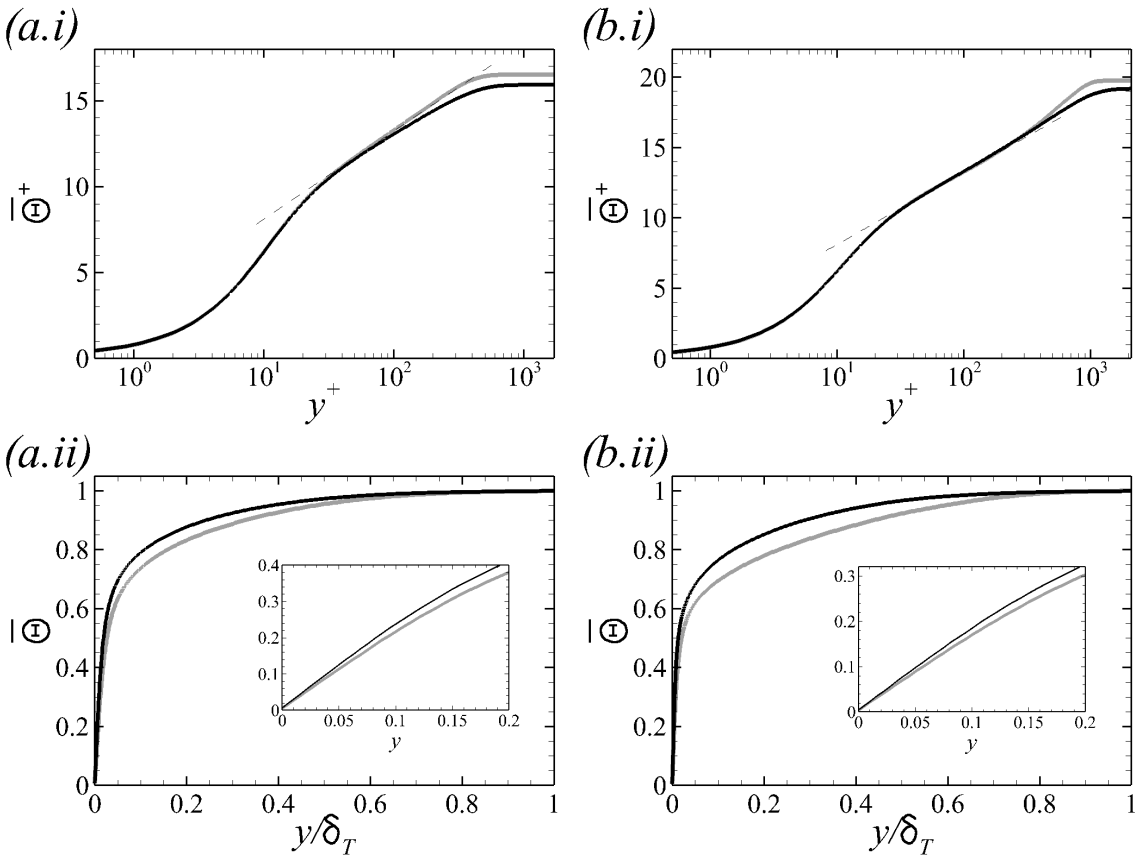

Figure 4.7: Profiles of the mean scalar at (a) $Re_{\Delta_2} = 900$ and (b) $Re_{\Delta_2} = 2700$, normalized by (i) Θ_τ and (ii) Θ_∞. The thin dashed line: $\overline{\Theta}^+ = \frac{1}{0.45}\ln(y^+) + 3$. (Gray) REF; (black) FRC.

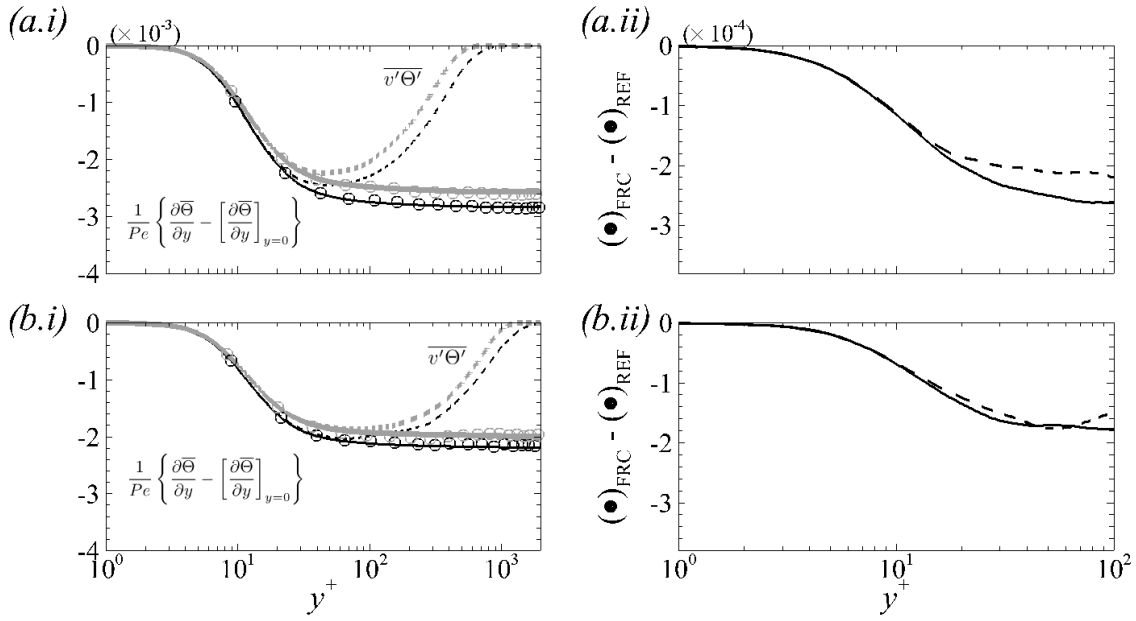

Figure 4.8: Profiles of (i) (—) $\frac{1}{Pe}\left(\frac{\partial\overline{\Theta}}{\partial y}-\frac{\partial\overline{\Theta}}{\partial y}\Big|_{y=0}\right)$, (- - -) $\overline{v'\Theta'}$ and (◯) summation of the right-hand side terms in equation (4.8) in (gray) REF and (black) FRC. (ii) Change in (—) $\frac{1}{Pe}\left(\frac{\partial\overline{\Theta}}{\partial y}-\frac{\partial\overline{\Theta}}{\partial y}\Big|_{y=0}\right)$ and (- - -) $\overline{v'\Theta'}$ from reference to forced flow. (a) $Re_{\Delta_2}=900$ and (b) $Re_{\Delta_2}=2700$.

is essentially unchanged in that region in presence of the forcing [11, 50, 77]. At the farther downstream location, $Re_{\Delta_2}=2700$ where the intensity of the free-stream forcing has significantly decayed, the effect of the disturbances on the mean profile is restricted to the thermal wake region. The bottom panels of figure 4.7 show the mean scalar using outer scaling. The temperature profile is much fuller in the forced case due to enhanced mixing of the high-Θ, or cold, fluid. The insets in the figures focus on the near-wall region to highlight the increase in the wall-normal gradient of the temperature deficit.

The change in $\partial\overline{\Theta}/\partial y$ in presence of free-stream forcing can be related to the wall-normal flux $\overline{v'\Theta'}$. Within the region of validity of the thermal boundary-layer approximation, the mean scalar is governed by,

$$\frac{\partial}{\partial y}\left(\frac{1}{Pe}\frac{\partial\overline{\Theta}}{\partial y}\right) = \frac{\partial\overline{u}\overline{\Theta}}{\partial x} + \frac{\partial\overline{v}\overline{\Theta}}{\partial y} + \frac{\partial\overline{v'\Theta'}}{\partial y}. \tag{4.7}$$

By integrating (4.7) from the wall to a height y, we obtain

$$\frac{1}{Pe}\left\{\frac{\partial\overline{\Theta}}{\partial y} - \left[\frac{\partial\overline{\Theta}}{\partial y}\right]_{y=0}\right\} = \int_y \frac{\partial\overline{u}\overline{\Theta}}{\partial x}\, dy + \overline{v}\overline{\Theta} + \overline{v'\Theta'}. \tag{4.8}$$

The left- and right-hand sides of equation (4.8) are plotted in figures 4.8*i* (solid lines and symbols), and agree to within the accuracy of the boundary-layer approximation. The figures also include the wall-normal-flux terms, and demonstrate the close connection between $\frac{\partial\overline{\Theta}}{\partial y}$ and $\overline{v'\Theta'}$ up to $y^+ \approx 100$. The change in each quantity from the reference to the forced flow is plotted in figures 4.8*ii*. The results confirm that the change in $\overline{v'\Theta'}$ is the key reason for the change in $\partial\overline{\Theta}/\partial y$ near the wall. Since the integral that defines St_a in equation (4.6) converges to 95% of its total value below $y^+ = 30$ (and 99% by $y^+ = 100$), the increase in the mean thermal dissipation in presence of free-stream turbulence can be tied to the change in wall-normal scalar flux.

Quadrant analysis [83] provides a finer grained view of the events that make up the wall-normal scalar flux. Of the four quadrants, the second ($Q2$) corresponds to ejection $v' > 0$ of hot fluid away from the wall $\Theta' < 0$; and the fourth ($Q4$) comprises sweeps $v' < 0$ of cold free-stream fluid $\Theta' > 0$. The quadrant contributions in the

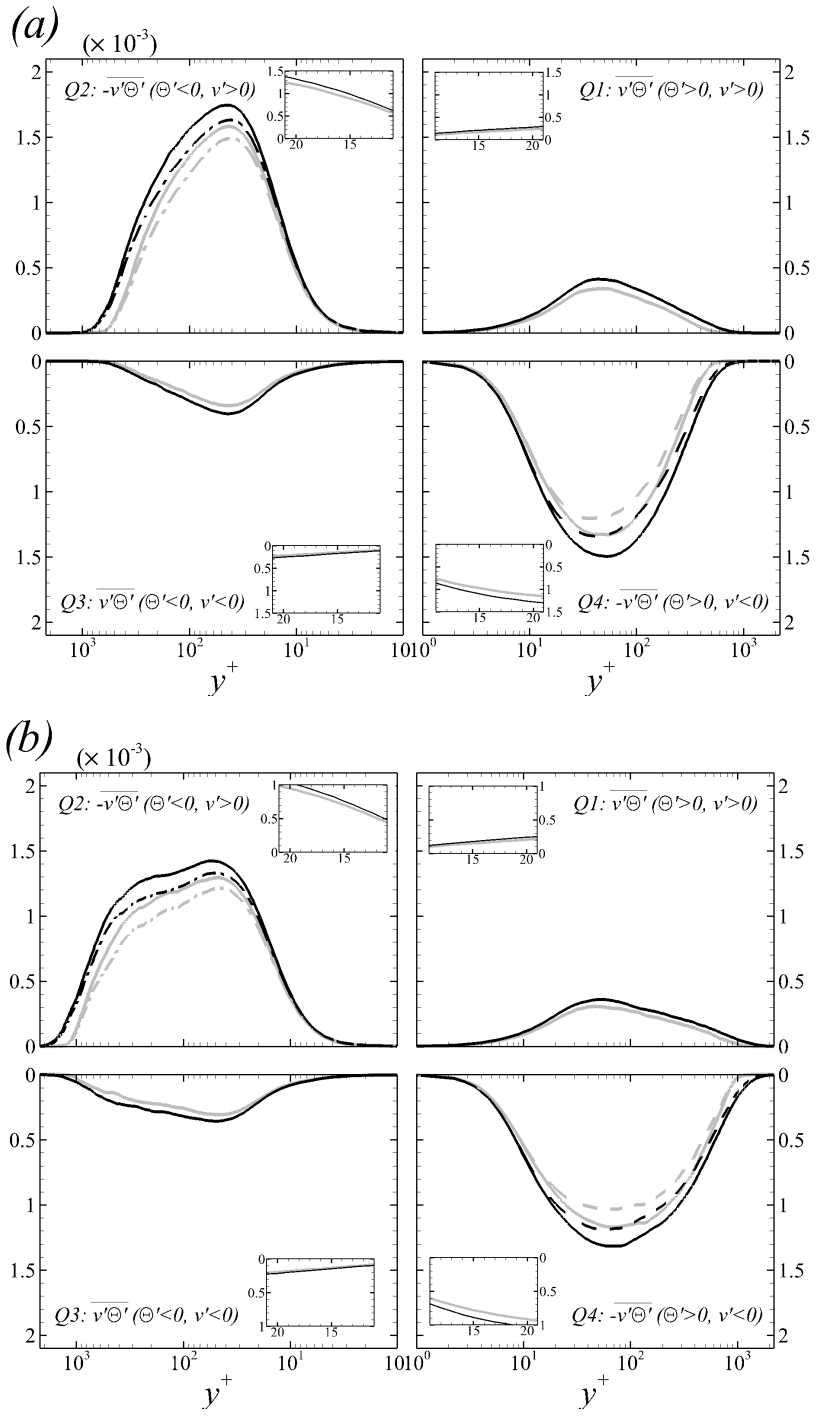

Figure 4.9: Contributions to wall-normal scalar flux, $-\overline{v'\Theta'}$ from each quadrant at (*a*) $Re_{\Delta_2} = 900$ and (*b*) $Re_{\Delta_2} = 2700$. Conditional contributions from the events: (- - -) $u' > 0$ and (- · -) $u' < 0$. (Gray) REF; (black) FRC.

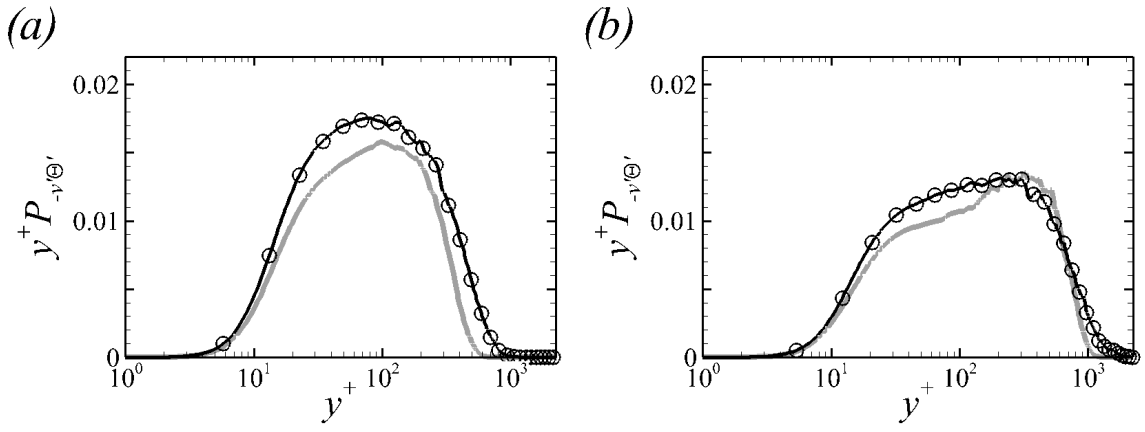

Figure 4.10: Profiles of pre-multiplied production of $-\overline{v'\Theta'}$, $y^+\mathcal{P}_{-v'\Theta'}$ at (a) $Re_{\Delta_2} = 900$ and (b) $Re_{\Delta_2} = 2700$. Symbols mark the leading contribution of $y^+\overline{v'v'}\frac{\partial\overline{\Theta}}{\partial y}$. (Gray) REF; (black) FRC.

reference and forced flows are compared in figure 4.9, at the two downstream positions $Re_{\Delta_2} = \{900, 2700\}$. In addition, the figure also reports the results for $Q2$ and $Q4$ further conditioned based on the sign of u'. In response to the free-stream forcing, the increase in the contributions by $Q2$ and $Q4$ events relative to their values in the reference flow are more appreciable than the other quadrants. This effect persists in the near-wall region (see insets) and is significant in the outer part of the boundary layer, at both downstream locations. At $Re_{\Delta_2} = 2700$, the profile of $Q2$ shows a pronounced increase in the log layer (figure 4.9b), which is not observed in $Q4$ fluxes which is related to the outer large-scale motions (§4.4).

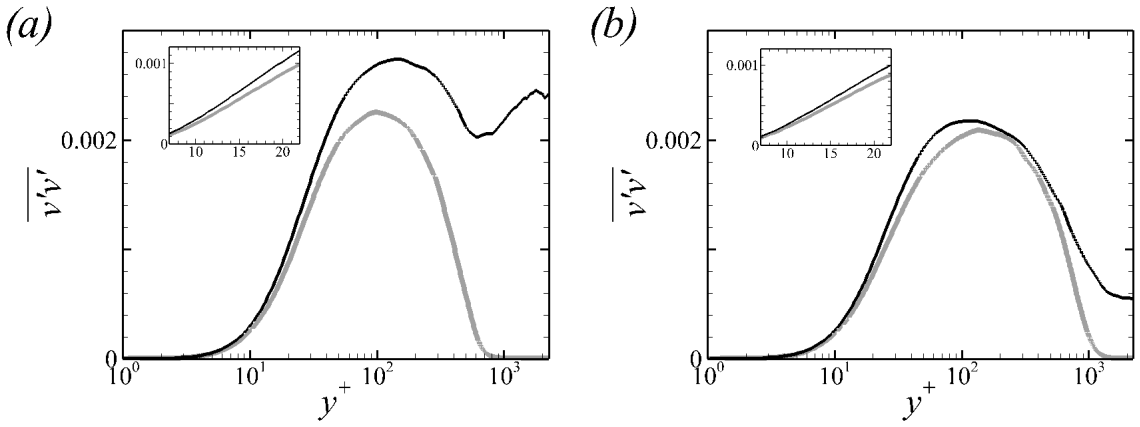

Figure 4.11: Profiles of wall-normal stress, $\overline{v'v'}$ at (a) $Re_{\Delta_2} = 900$ and (b) $Re_{\Delta_2} = 2700$. (Gray) REF; (black) FRC.

4.3.4 Turbulent stresses and heat flux

The increase in the wall-normal scalar flux, $-\overline{v'\Theta'}$, motivates an assessment of its production,

$$\mathcal{P}_{-v'\Theta'} = \overline{u'v'}\frac{\partial\overline{\Theta}}{\partial x} + \overline{v'v'}\frac{\partial\overline{\Theta}}{\partial y} + \overline{u'\Theta'}\frac{\partial\overline{v}}{\partial x} + \overline{v'\Theta'}\frac{\partial\overline{v}}{\partial y}, \tag{4.9}$$

which is plotted in figure 4.10 pre-multiplied by y^+. In the forced case, this term is enhanced throughout the boundary layer at the upstream location $Re_{\Delta_2} = 900$. Farther downstream, at $Re_{\Delta_2} = 2700$, the difference between the two cases is still appreciably up to $y^+ \approx 200$, despite the decay of the free-stream forcing.

The predominant contribution to $\mathcal{P}_{-v'\Theta'}$ is by $\overline{v'v'}\frac{\partial\overline{\Theta}}{\partial y}$, which is marked by circles in figure 4.10. Its increase in the forced flow is anticipated since energetic free-stream turbulence comprises $\overline{v'v'}$, and buffets the underlying boundary layer where the normal stresses would decay towards the free stream absent external forcing. Profiles of $\overline{v'v'}$ are plotted in figure 4.11: At $Re_{\Delta_2} = 900$, the free-stream value of

the stress in the forced flow is of the same order as the peak boundary-layer value in the reference case. The external disturbances augment $\overline{v'v'}$ inside the boundary layer at this upstream location and, in turn, appreciably enhance the production term $\mathcal{P}_{-v'\Theta'} \approx \overline{v'v'}\left(\partial\overline{\Theta}/\partial y\right)$. However, the effect is reduced downstream at $Re_{\Delta_2} = 2700$ as the free-stream turbulence decays.

Once the higher level of $-\overline{v'\Theta'}$ is established, it has the dual effect of distorting the mean-scalar profile (equation 4.8 and figure 4.8) and also causing an increase in production of scalar variance—both effects increase the Stanton number. The second is reported in figure 4.12 where the production of scalar variance is plotted in the pre-multiplied form, $-y^+\overline{v'\Theta'}\left(\partial\overline{\Theta}/\partial y\right)$. The peak at $y^+ \approx 20$ is enhanced throughout the streamwise extent of the flow, as exemplified at the two reported Reynolds numbers. At $Re_{\Delta_2} = 900$, where the thermal boundary-layer thicknesses have just become commensurate in size with the momentum counterpart, the increase in production in the forced case is primarily due to the buffer layer (figure 4.12*a*). At the downstream location $Re_{\Delta_2} = 2700$, the logarithmic layer becomes an equally important contributor to the increase in production of scalar variance (figure 4.12*b*). These changes should be viewed in conjunction with the enhanced ejection and sweep events ($Q2$ and $Q4$ in figure 4.9*b*).

The above changes in the forced boundary layer are accompanied with higher levels of thermal fluctuations $\overline{\Theta'\Theta'}$ as shown in figure 4.13. At $Re_{\Delta_2} = 900$, the peak at $y^+ \approx 18$ increases by 12.5%, but the effect diminished at larger wall-normal

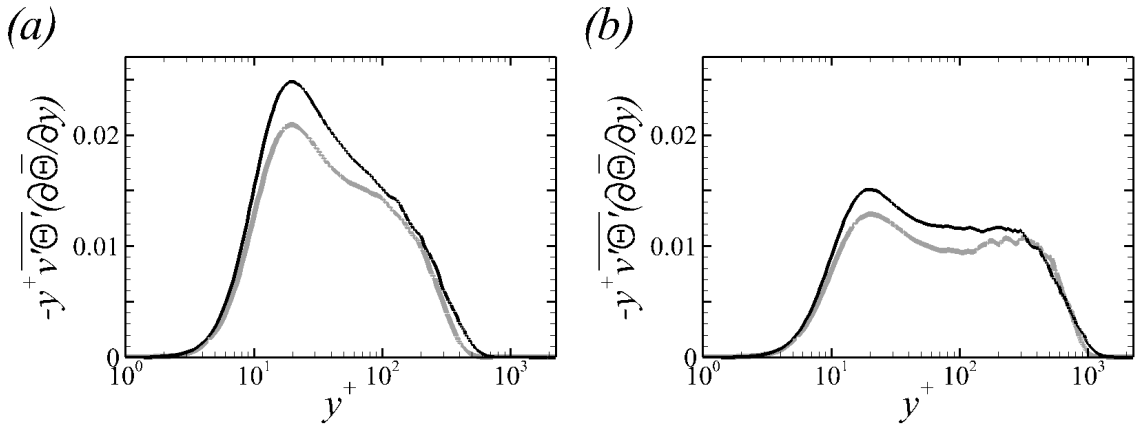

Figure 4.12: Profiles of $-y^+\overline{v'\Theta'}\frac{\partial\overline{\Theta}}{\partial y}$ at (a) $Re_{\Delta_2} = 900$ and (b) $Re_{\Delta_2} = 2700$. (Gray) REF; (black) FRC.

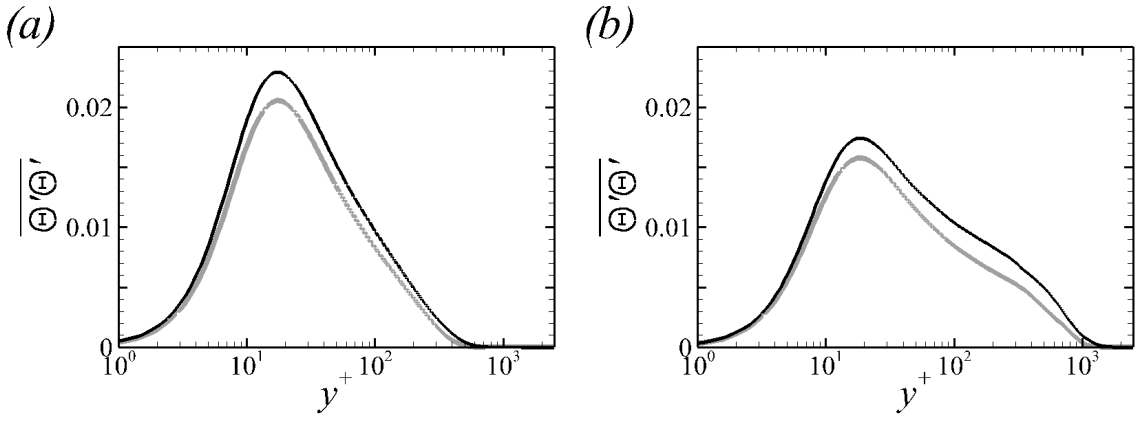

Figure 4.13: Profiles of scalar variance, $\overline{\Theta'\Theta'}$ at (a) $Re_{\Delta_2} = 900$ and (b) $Re_{\Delta_2} = 2700$. (Gray) REF; (black) FRC.

heights. At the downstream station $Re_{\Delta_2} = 2700$, where the thermal boundary layer has outgrown the momentum counterpart, the buffer layer peak in $\overline{\Theta'\Theta'}$ increases by 10.7%. In addition, the enhanced thermal fluctuations remain appreciable throughout the logarithmic layer, which can be indicative of the formation of outer large-scale thermal structures.

4.4 Thermal structures

When the low-frequency perturbations with the free-stream turbulence interact with the boundary layer, they lead to the formation and amplification of large-scale velocity perturbations in the logarithmic region, even at Reynolds numbers where they would not be observed in the unforced flow (§3.5). The present simulations indicate that the large-scale momentum perturbations in the forced boundary layer are accompanied by large-scale thermal structures. An instantaneous realization of these structures is shown in figure 4.14, where they are visualized using iso-surfaces of Gaussian filtered thermal perturbations $\hat{\Theta}'$ (see Lee et al. [49] for details of the structure identification procedure). By contrasting the reference and forced boundary layers, the figure qualitatively demonstrates that in the latter configuration the outer thermal structures form and grow to significantly larger sizes with downstream distance.

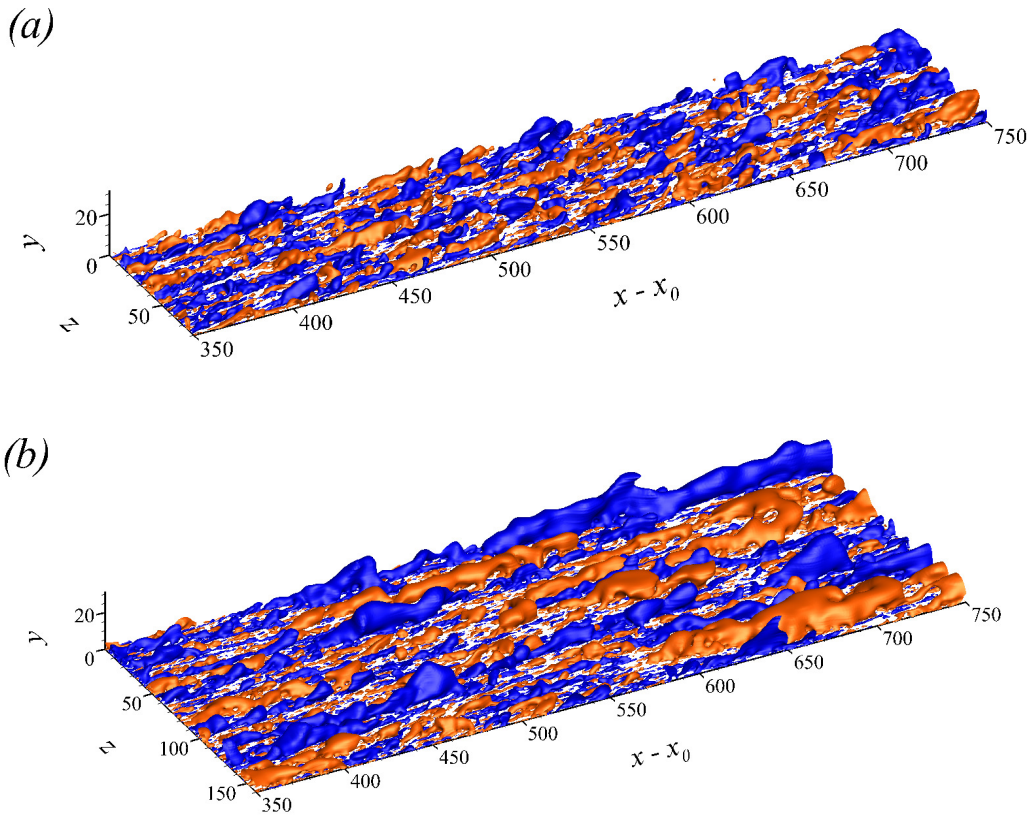

Figure 4.14: Iso-surfaces of the Gaussian filtered thermal field $\hat{\Theta}'$. (a) REF and (b) FRC. (Blue) $\hat{\Theta}' = -0.06$ and (red) $\hat{\Theta}' = 0.06$.

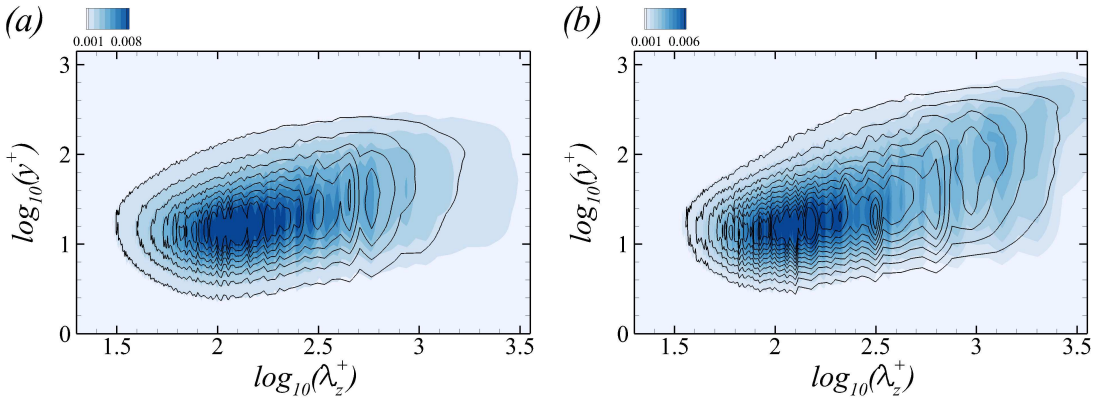

Figure 4.15: One-dimensional premultiplied spectra of Θ, $\kappa_z \Phi_{\Theta'\Theta'}(\lambda_z)$ at (a) $Re_{\Delta_2} = 900$ and (b) $Re_{\Delta_2} = 2700$. (Line contour) REF; (color contour) FRC.

The spanwise spectrum of the scalar fluctuations was evaluated,

$$\Phi_{\Theta'\Theta'} = \int_{-\infty}^{\infty} \overline{\Theta'(z)\Theta'(z+\zeta)} e^{-i\kappa_z \zeta} \, d\zeta, \tag{4.10}$$

where $\kappa_z = 2\pi/\lambda_z$ is the spanwise wavenumber and λ_z is the wavelength. Figure 4.15 compares the pre-multiplied spectra $\kappa_z \Phi_{\Theta'\Theta'}$ in the reference and forced flows, which are represented by the line and color contours, respectively. At $Re_{\Delta_2} = 900$, a near-wall peak is visible in both flow configurations, although the contours spread towards larger λ_z in the forced case. At the higher Reynolds number $Re_{\Delta_2} = 2700$, an outer peak emerges and is due to the large-scale thermal structures. The associated spanwise wavelengths are $\lambda_z^+ \approx 950$ in the canonical boundary layer and $\lambda_z^+ \approx 1400$ in the forced flow, and its magnitude is appreciably higher in the latter case. The spectra thus provide quantitative evidence that the outer thermal structures in the boundary layer are enhanced in strength and size in presence of free-stream turbulence.

The outer large-scale thermal structures do not exist in isolation; they are estab-

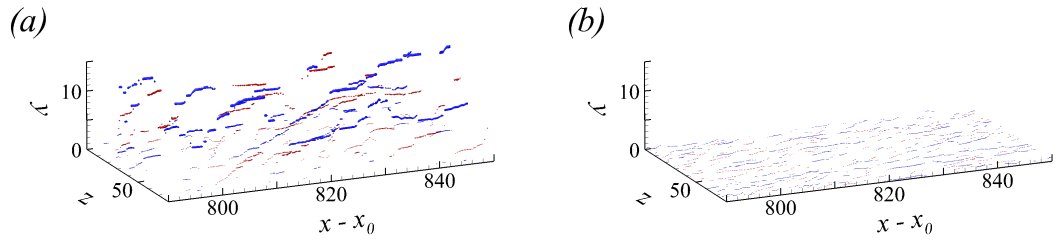

Figure 4.16: Cores of the filtered thermal structures (a) in outer region $y^+ > 30$ and (b) near the wall $y^+ < 30$. (Blue) $\mathcal{C}^N$ and (red) $\mathcal{C}^P$.

lished by and coexist with the velocity perturbations. The connection is examined by evaluating the conditionally averaged perturbation fields in the vicinity of the cores of large-scale thermal features. Details of the algorithm are provided in the work by Lee et al. [49], and are only summarized here. Firstly, these cores of the structures are identified in the filtered fields (figure 4.14) using the local extrema of $\hat{\Theta}'$ in the cross-flow plane which exceed a prescribed threshold, here ten percent of $\overline{\Theta'\hat{\Theta}'}/\overline{\Theta'\Theta'}$. The cores are distinguished into outer and inner ones based on their heights relative to $y^+ = 30$, as shown in figure 4.16. They are subsequently classified based on the sign of the perturbation into positive $\mathcal{C}^P$ and negative $\mathcal{C}^N$ ones. The thermal and velocity fields are then shifted in the span in order to align the cores of the structures and evaluate the conditional averages, are computed. For example,

$$\Psi^P_{\mathcal{L}}(y, \Delta z) = \overline{\Psi(y, z + \Delta z) \;\; | \;\; \mathcal{C}^P{}_{|y^+>30}}, \tag{4.11}$$

$$\Psi^N_{\mathcal{L}}(y, \Delta z) = \overline{\Psi(y, z + \Delta z) \;\; | \;\; \mathcal{C}^N{}_{|y^+>30}}, \tag{4.12}$$

where $\Psi = \{\Theta', u', v', w'\}$; the superscripts $\{P, N\}$ refer to positive and negative perturbations; and the subscript $\mathcal{L}$ indicates that the average is conditioned on the

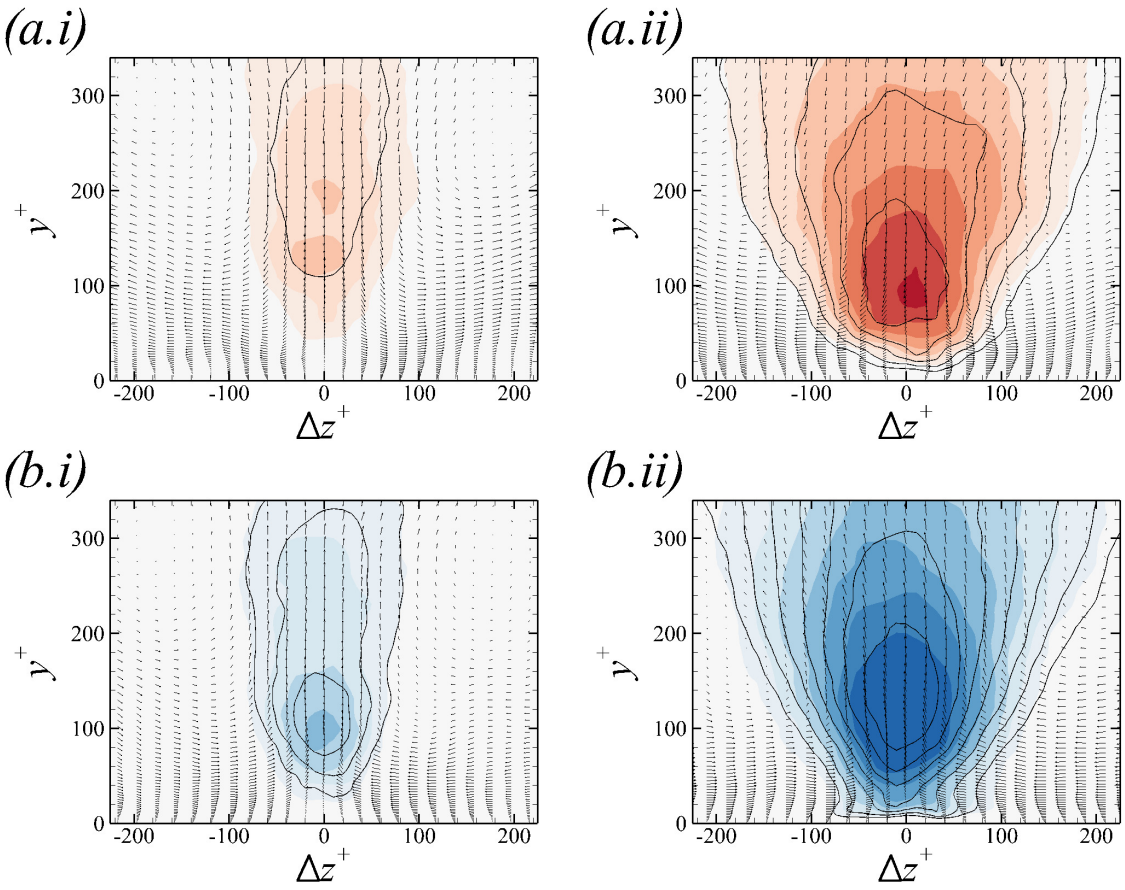

Figure 4.17: Contours of (a) (color) $\Theta'^P_{\mathcal{L}}$ and (line) $u'^P_{\mathcal{L}}$, and (b) (color) $\Theta'^N_{\mathcal{L}}$ and (line) $u'^N_{\mathcal{L}}$ at $Re_{\Delta_2} = 2700$. (i) REF; (ii) FRC. Vectors represent the components (v', w'). Positive (negative) contour levels are $[0.04, 0.1]$ ($[-0.04, -0.1]$) plotted with red (blue). Contour level increment is 0.01.

extrema of the large-scale structures in the outer region $y^+ > 30$. A subscript $\mathcal{B}$ is used when the average is conditioned on the cores of near-wall structures, $y^+ < 30$.

The conditionally averaged fields are reported in figure 4.17: the color contours correspond to Θ', the line contours correspond to u', and the vectors are the in-plane velocity perturbations (v', w'). While the condition for averaging is based on the extrema in $\hat{\Theta}'$, the conditional fields show that the thermal structures coincide with

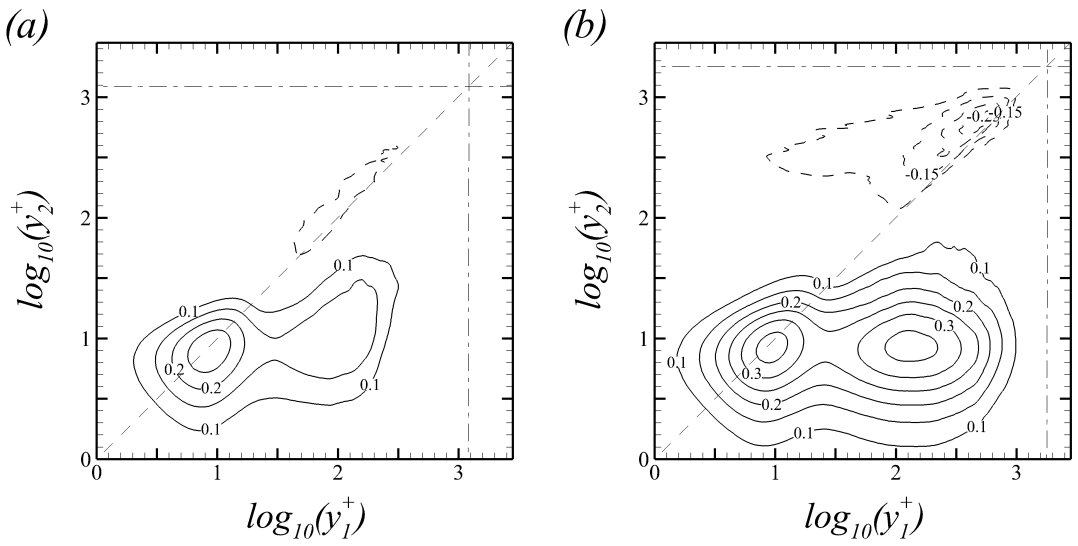

Figure 4.18: Two-point amplitude modulation coefficient $C^{2p}_{u,\Theta}$ normalized by $u_\tau\Theta_\tau$ at $Re_{\Delta_2} = 2700$. (a) REF; (b) FRC. Negative contours are plotted with dashed lines ($--$). Dashed-dot lines ($-\cdot-$) indicate $y/\delta_T = 1$. Increments of contour levels are 0.05.

the streamwise velocity ones. Both are accompanied by counter-rotation roll motions in the (v', w') vector fields; these rolls effect the sweeps of positive (Θ', u') and lift up of negative (Θ', u'). In addition, the size and amplitude of both the thermal and hydrodynamic perturbations are larger in the forced boundary layer than in the reference case. These results are consistent with the enhanced $Q2$ and $Q4$ events in the quadrant analysis (figure 4.9). Furthermore, the wall-normal extrema of $\Theta'^{\{P,N\}}_{\mathcal{L}}$ are located at approximately $y^+ \approx 100$, which corresponds to the position of the outer peak in the pre-multiplied spectra (figure 4.15b).

In §3.5, the formation of outer large-scale u' motions in the forced boundary layer strongly influence the near-wall hydrodynamic field. Whether they similarly influence the near-wall thermal field can be assessed by examining the two-point amplitude

modulation (AM) coefficient,

$$C^{2p}_{u,\Theta}(y_1, y_2) = \overline{u'_L(y_1)\Theta'_{EL}(y_2)}, \tag{4.13}$$

where u'_L is the large-scale streamwise velocity perturbation computed using a spectral cut-off filter in the spanwise direction, and Θ'_{EL} is the filtered envelope of small-scale thermal perturbation. Contours of $C^{2p}_{u,\Theta}$ are provided in figure 4.18, normalized by $u_\tau\Theta_\tau$. In the reference case, a positive peak below the diagonal indicates that large-scale velocity structures at $y_1^+ \approx 100$ modulate the small-scale thermal perturbations at $y_2^+ \approx 10$. When the boundary layer is forced by free-stream turbulence, this peak becomes much more pronounced, which demonstrates that the coherent velocity perturbations in the log layer modulate and invigorate the near-wall thermal structures.

This modulation can also be identified in the near-wall ($y^+ < 30$) conditionally averaged fields, $\Psi^{\{P,N\}}_{\mathcal{B}}(y, \Delta z)$. The results are visualized in figure 4.19. Similar to the observation by Hwang et al. [37] for the velocity motions, the near-wall thermal structures are accompanied by larger-scale rolls that extend much higher into the logarithmic layer. And even though the sizes of the conditionally averaged fields in the reference and forced flows are comparable to one another, the intensity of the latter is larger due to the amplitude modulation: The extrema of $\Theta'^{\{P,N\}}_{\mathcal{B}}$ increase from $\{+0.215, -0.194\}$ to $\{+0.227, -0.205\}$ with free-stream forcing.

The signature of the near-wall thermal structures on the heat-transfer rate at the wall is captured by evaluating the conditional average st,

$$st^P_{\mathcal{B}}(\Delta z) = \overline{st(z + \Delta z) \;\; | \;\; \mathcal{C}^P}_{|y^+<30}, \tag{4.14}$$

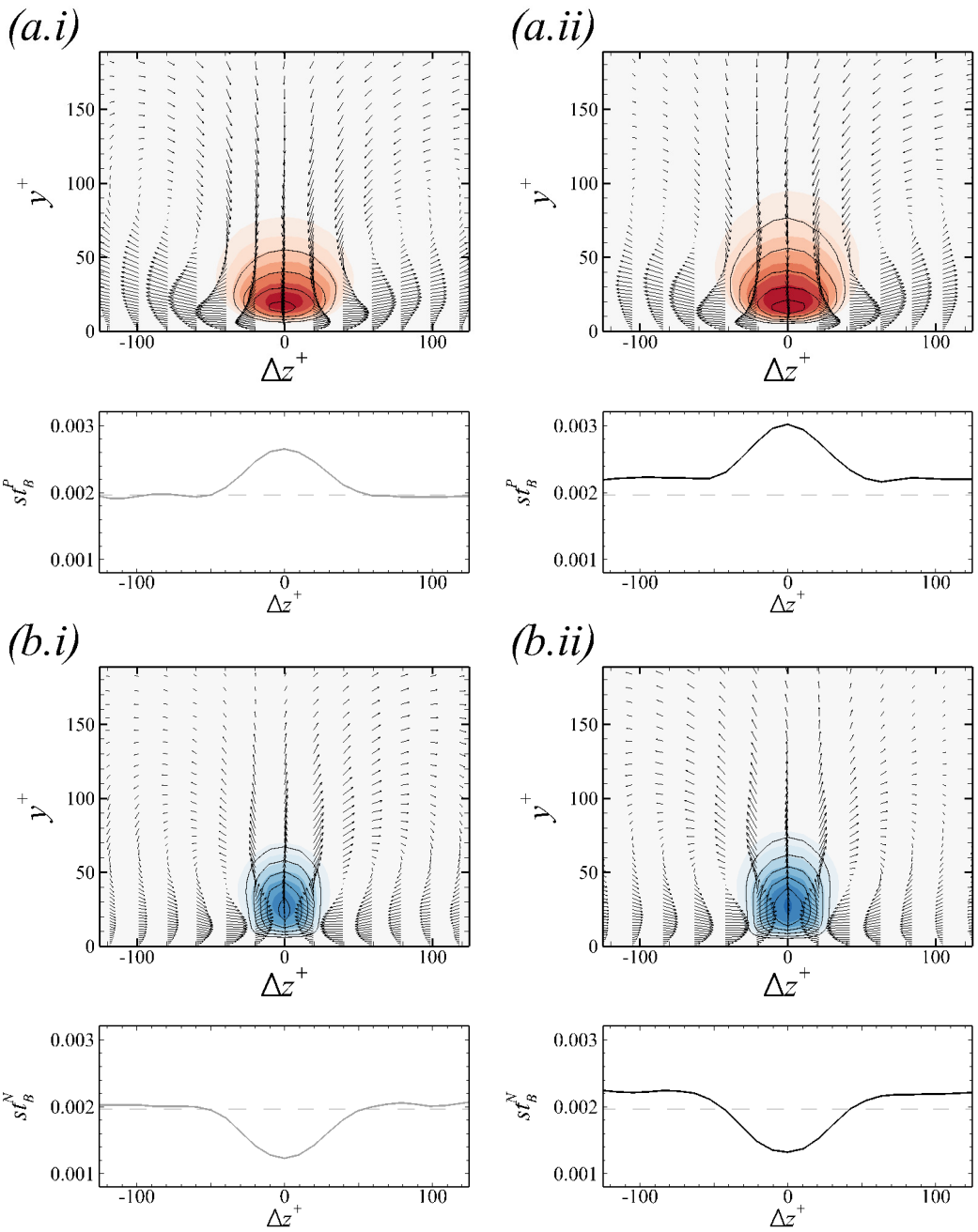

Figure 4.19: Contours of (a) (color) $\Theta_{\mathcal{B}}'^{P}$ and (line) $u_{\mathcal{B}}'^{P}$, and (b) (color) $\Theta_{\mathcal{B}}'^{N}$ and (line) $u_{\mathcal{B}}'^{N}$, at $Re_{\Delta_2} = 2700$. The contour ranges are $[0.08, 0.2]$ and $[-0.08, -0.2]$, with increment 0.02. Vectors represent the components (v', w'). (i) REF; (ii) FRC. Shown below each contour plot is the spanwise distribution of the conditionally average Stanton number, $st_{\mathcal{B}}^{\{P,N\}}$. The thin dashed line marks St of the reference boundary layer.

$$st^N_{\mathcal{B}}(\Delta z) = \overline{st(z+\Delta z) \;\; | \;\; \mathcal{C}^N}_{|y^+<30}. \tag{4.15}$$

The profiles in figure 4.19 demonstrate that the heat flux is increased by sweeps of $\Theta'^{\{P\}}_{\mathcal{B}}$, and to a lesser extent reduced by the weaker ejections of $\Theta'^{\{N\}}_{\mathcal{B}}$. This trend is enhanced when the boundary layer is exposed to free-stream turbulence.

In summary, when a turbulent boundary layer is buffeted by free-stream vortical perturbations, both the wall friction and heat-transfer rate are enhanced. The dynamics of wall turbulence have been studied previously; for example the Reynolds stresses are enhanced and large-scale energetic motions are formed in the logarithmic layer. These hydrodynamic changes are also accompanied by changes in the thermal field as well: the variance of thermal fluctuations is also increased, and the outer large-scale streaky structure are accompanied by thermal counterparts. In addition, the outer large-scale velocity motions modulate the near-wall thermal structures and enhance their amplitude.

4.5 Conclusion

Direct numerical simulations of a thermal turbulent boundary layer beneath quiescent and vortical free streams were performed. The inflow momentum-thickness Reynolds number is $Re_\theta = 1200$ and, in the forced case, the intensity of the homogeneous and isotropic free-stream turbulence is $Tu = 10\%$. The fluid at the inlet plane has temperature $T = 0$, and encounters an isothermal flat plate at $T_w = 1$; the

corresponding temperature deficits are therefore $\Theta \equiv 1 - T = \{1, 0\}$ respectively.

When the free stream is turbulent, the wall heat-transfer rate increases by up to 10% relative to the unforced flow. This phenomenon is explained by evaluating three contributions to the Stanton number St: the rates of thermal dissipation in the mean-temperature gradient, production of the scalar variance, and advection of heat into the flow. The first two make the largest contribution to St and also account for its increase in the forced boundary layer. Both terms are enhanced due to the increase in the wall-normal scalar flux $\overline{v'\Theta'}$.

The ingested free-stream vortical disturbances contribute additional $\overline{v'v'}$ stresses in the outer part of the boundary layer (figure 4.11). It thus enhances the production of scalar flux $\overline{v'\Theta'}$ which distorts the mean-temperature profile (figures 4.10) and increases the production of scalar variance $\overline{\Theta'\Theta'}$ (figures 4.12). The latter effect is concentrated in the buffer layer at $Re_{\Delta_2} = 900$, although the contribution from the logarithmic layer becomes equally important with downstream distance. On the whole, while the free-stream turbulence is only vortical and without any thermal disturbances, the forced boundary layer sustains higher levels of thermal fluctuations.

Underlying the statistical changes in the scalar field of the forced boundary layer are the formation and amplification of large-scale thermal structures in the logarithmic region. These elongated regions of positive and negative temperature perturbations coincide with large-scale streamwise velocity disturbances, and both are generated by the same roll motions. The outer large-scale hydrodynamic field also

modulates, and enhances the intensity, of the near-wall thermal streaks (figure 4.18*b*). The signature of these near-wall thermal events is evident in the conditionally averaged Stanton number, which is more elevated beneath sweeps of positive $\Theta'_{\mathcal{B}}$ than reduced beneath ejections of negative $\Theta'_{\mathcal{B}}$.

In the present study, the free-stream turbulence was homogeneous and isotropic. Since the low-frequency part of the free-stream energy spectrum is most effective at permeating the boundary layer and inducing the amplification of the outer large-scale motions (§3.5), future efforts should examine the influence of free-stream anisotropy on the boundary-layer hydrodynamic and thermal responses.

The effects of the free-stream forcing on the boundary layers on the flat plate were covered in §3 and §4. The free-stream turbulence buffets the underlying flow on the concave curve in the next chapter.

Chapter 5

Turbulent boundary layer buffeted by free-stream disturbances over concave curvature

5.1 Introduction

In practical flow configurations, turbulent boundary layers (TBLs) often develop over curved surfaces. The focus in the present study is on concave curvature which induces centrifugal effects in addition to the external pressure gradient. Another important practical consideration is the presence of environmental disturbances, or free-stream forcing, which can appreciably alter the dynamics within the underlying boundary layer. For example, when a flat-plate TBL is buffeted by free-stream tur-

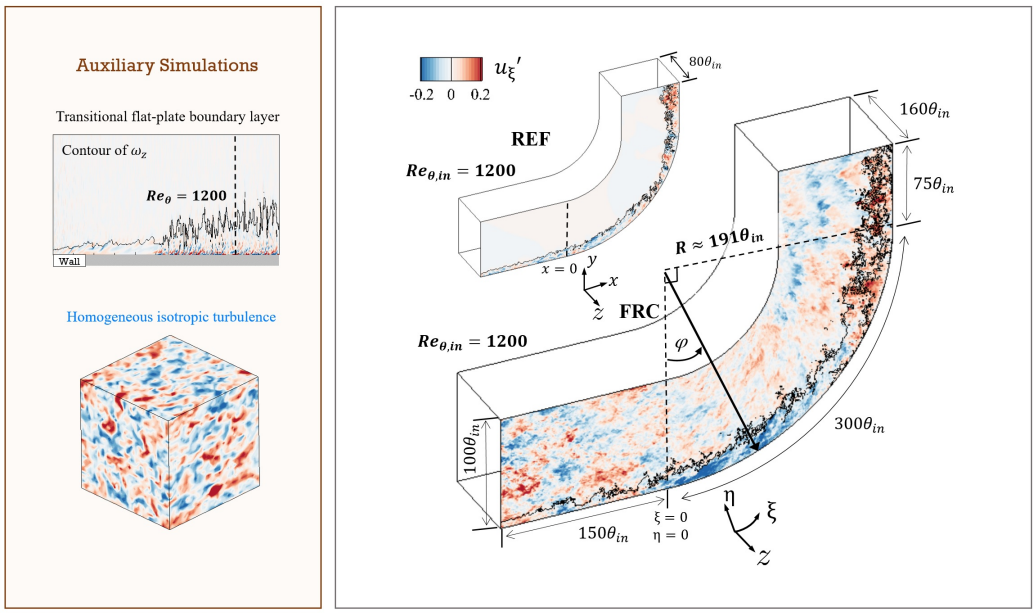

Figure 5.1: Configurations of two auxiliary computations to generate the inflow conditions, and the two main computations of turbulent boundary layer over curved wall without and with free-stream turbulence.

bulence (FST), its thickness and skin-friction coefficient increase appreciably, even though the free-stream fluid does not breach the logarithmic layer as it penetrates towards the wall (§3). The present work uses direct numerical simulations (DNS) to probe the combined effects of the concave curvature and FST on the boundary layer. Two simulations are contrasted, and correspond to the turbulent boundary layer on the concave wall developing beneath quiescent and vortical free streams (see figure 5.1).

Curved-wall turbulent boundary layers are influenced by three effects [23]: i) turbulence changes due to the mean-flow turning, ii) potential formation of coherent Görtler vortices, and iii) the impact of these coherent vortices on the turbulence. The

second mechanism is triggered when the boundary-layer thickness (e.g. momentum thickness θ) is comparable to the radius of curvature (R). In laminar flows, an instability leads to the formation of distinct longitudinal Görtler vortices [73]. In turbulent flows, however, Görtler structures are notoriously difficult to identify, which obfuscates precise description. The complexity is compounded when TBLs are exposed to free-stream turbulence: Whether the external forcing will decorrelate the centrifugal structures or enhance them is uncertain, and how the coupling between the Görtler structures and the finer-scale boundary-layer turbulence will be affected is unknown.

Much of the literature on curved-wall turbulence has focused on conditions with quiescent free streams. Barlow and Johnston [5] performed experiments to probe the response of the boundary layer to a sudden onset of concave curvature. They reported that higher momentum eddies move toward the wall, while lower momentum eddies travel away from it. Despite efforts to visualize the streamwise vortices using the colored-dye and laser-induced-fluorescence methods, the influence of the roll cells on the statistics was not evident. Random distribution of vortex structures in turbulence can obscure their detection [23]. In other works, Hoffmann et al. [33] and Barlow and Johnston [6] used a vortex generator to induce large-scale, time-stable roll cells, which produced a coupling between the large-scale outer fluid motions and near-wall turbulence. Barlow and Johnston [6] showed that the downwash suppresses the bursting, which induces interactions between sublayer structures and outer-layer eddies, while the upwash enhances the process. However, the connection between

naturally occurring Görtler vortices in turbulence (irregularly spaced and temporally intermittent) to those produced by synthetic means is unknown [e.g. 67].

Lund and Moin [54] and Arolla and Durbin [3] numerically modelled the experiment by Barlow and Johnston [5]. They used large-eddy simulations (LES) to directly probe the longitudinal vortices due to the centrifugal effect. Spatially filtering the turbulence field revealed streamwise-aligned structures inside the TBL above the curved wall, which supports the existence of Görtler structures within the boundary-layer turbulence [3, 54]. However, the degree that the external pressure gradient influences the TBL on the curved surface was not addressed—an effect that depends on the flow setup. At the onset of mean-streamline curvature, an adverse pressure gradient is established and the opposite effect takes place at the end of the curved section. Such minutiae have implications on the choice of the computational domain and consequence on the downstream development of the boundary layer and flow structures. Top walls can be contoured to isolate curvature effects from streamwise pressure gradient [5, 6], but in practical configurations the pressure gradient is present and impacts the behaviour of the flow on the curved wall.

A related configuration is the flow in an 'S'-shaped duct, where the boundary layer is subject to pressure gradients and curvature. Experiments show that the skin friction has local extrema after curvature changes, which are concomitant with streamwise pressure variations [4]. Corresponding LES by Lopes et al. [53] shows that the mean flow was separated near the convex-to-concave transition due to the strong

adverse pressure gradient. Intermittent separation was also observed as the flow progressed from the convex to flat region, but the phenomenon was seldom observed in the flat-to-concave transition [53].

Studies that have examined FST-TBL interactions over curved walls have mainly focused on the flow recovery from the curved section on the downstream flat wall. [42] compared the boundary layers at low and high inlet free-stream turbulence intensities, $Tu = 0.6\%$ and 8%, and reported an increase in skin friction by up to 20% in the latter case. The authors also contrasted their ability to identify the Görtler vortices in the first case but not in presence of free-stream forcing, which is unlike the established observation that free-stream forcing promotes the generation of outer large-scale motions in flat-plate boundary layers (§3). In the same experimental configuration, Kestoras and Simon [43] used the temperature field over the constant heat-flux plate in order to evaluate the probability of observing boundary-layer fluid, which was their definition of intermittency. The forced case exhibited enhanced mixing, a trend that is in agreement with flat-plate boundary layers exposed to free-stream turbulence [29]. Their intermittency curves were not however presented in viscous scaling, so it is not possible to quantify the extent to which the free-stream fluid penetrated towards the wall.

To date, few works quantify the degree of coupling between turbulent boundary layers on curved walls in tandem with free-stream disturbances. We herein examine the curved-wall configuration and contrast the turbulent boundary layers from two

simulations: (i) a reference case with a quiescent free stream and (ii) a forced case with 10% free-stream turbulence intensity at the inlet plane. The setup of the simulations is described in section 2. Section 3 briefly discusses the influence of curvature and FST on the mean flow and the turbulence, statistically, and §4 focuses on the impact on the turbulent flow structures. The conclusions are provided in the final section.

5.2 Simulation setup

In this chapter, the velocity components in the streamwise (ξ), wall-normal (η) and spanwise (z) directions are u_ξ, u_η and w, respectively. Note that x and y indicate the horizontal and vertical directions in Cartesian coordinates.

A schematic of the flow configurations is shown in figure 5.1. Two main simulations are contrasted: a reference (REF) case where the curved-wall boundary layer develops beneath a quiescent free stream and a forced (FRC) case where the free stream is turbulent. In both cases, the flow domains include an initial flat section ($150\,\theta_{in}$), a curved section ($300\,\theta_{in}$), and a recovery flat section ($75\,\theta_{in}$). The quarter-circular section has radius $R = 191\,\theta_{in}$. The spanwise domain of the forced configuration is two times larger than the reference case, in order to accommodate the formation of large-scale structures which are anticipated based on earlier studies (§3). Table 5.1 summarizes the domain sizes and grid resolutions. The grids are uniform in the span and stretched in the wall-normal direction using a hyperbolic tangent function. In the

Designation	Inflow	Domain size (θ_{in}) $L_\xi \times L_\eta \times L_z$	No. of grid points $N_\xi \times N_\eta \times N_z$	Resolution $\Delta\xi^+, \Delta\eta^+, \Delta z^+, \Delta t^+$
REF	TBL	$525 \times 100 \times 80$	$2688 \times 896 \times 768$	10.5, 0.29-7.8, 5.6, 0.048
FRC	TBL+HIT	$525 \times 100 \times 160$	$2688 \times 896 \times 1536$	10.5, 0.29-7.8, 5.6, 0.041

Table 5.1: Computational domain sizes, and spatial and temporal resolutions at the inflow plane expressed in viscous '$_+$' units.

streamwise direction, the grid spacing is uniform on the bottom wall ($\eta = 0$). On the top surface, the grid is uniform on the curved section and is adjusted smoothly near the changes in curvature. An elliptic grid generation technique [e.g. 82] is adopted to reduce strong variations in mesh spacing in those regions; the ratio of successive streamwise grid spacing was less than 3%.

No-slip conditions are applied at the bottom wall, while impermeability and no-stress conditions are imposed at the parallel top boundary. The domains are periodic in the spanwise direction, and convective outflow conditions are imposed at the exit planes.

At the inflow plane of the main computations, either the time-dependent turbulent boundary layer is applied alone (REF case) or is it superposed with free-stream turbulence (FRC case). In the latter case, the HIT box is introduced above the edge of the boundary layer which was identified using a normalized vorticity threshold, $\frac{|\omega|}{u_\tau^2/\nu}\sqrt{\delta_{99}^+} = 0.2$ where ω is the vorticity, u_τ is the friction velocity, ν is the kinematic viscosity and δ_{99}^+ is the 99% boundary-layer thickness in wall units [49]. A

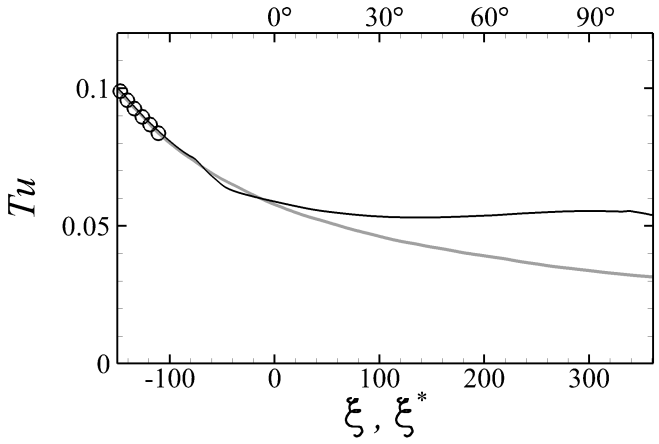

Figure 5.2: Downstream dependence of the free-stream turbulence intensity Tu. (Black) Curved-wall FRC simulation; (gray) results from flat-plate simulations in §3; (◯) temporal decay of HIT in precursor simulation plotted versus $\xi^* = U_\infty t$.

levelset function ψ is defined at the inflow plane and tags, or differentiates, the fluid within the boundary layer ($\psi = 1$) and the free stream ($\psi = 0$). Full details of the implementation are provided in §3.3.

Beyond an initial transient and once the flow over the curved surface has reached a statistically stationary state, statistics were collected for $T_{\text{stat}} = 1{,}207.5$ (REF) and 892.5 (FRC) convective time units. A bar will indicate an average in homogeneous coordinates, and the prime will refer to perturbation quantities according to Reynolds decomposition, for example $u_\xi = \overline{u_\xi} + u'_\xi$.

Before assessing the impact of FST on curved-wall boundary layers in the following section, we quantify the downstream dependence of the FST intensity in figure 5.2. Upstream, within the flat section ($\xi \leq -100$), the decay in space in the main simulation agrees with the temporal decay of Tu in the pseudo-spectral auxiliary

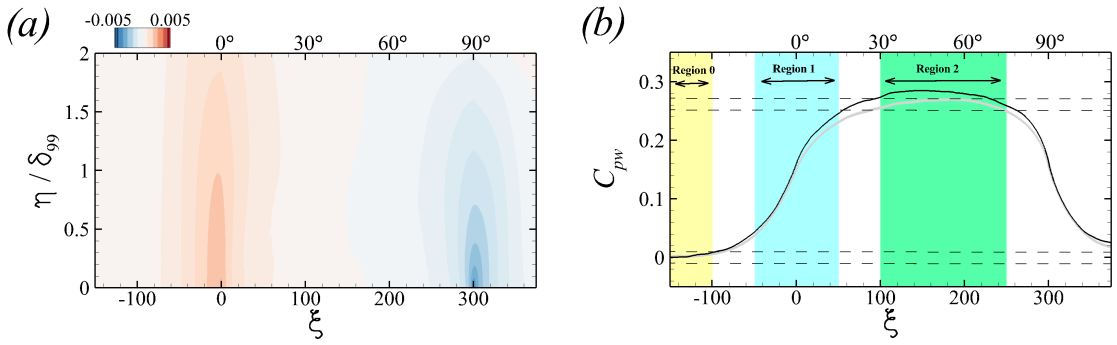

Figure 5.3: (a) Streamwise pressure gradient $\partial\overline{p}/\partial\xi$ in REF. (b) Wall-pressure coefficient, C_{pw}: (gray) REF and (black) FRC. Lower dashed lines mark ZPG region following criterion by Harun et al. [30]; top dashed lines mark $(\max(C_{pw}) - C_{pw}) \leq 0.02$ for REF.

DNS of HIT to within the Taylor's hypothesis $\xi^* = U_\infty t$. In that region, the present results also agree with the previous study of free-stream turbulence over a flat-plate boundary layer (§3), but the two curves show the first signs of dissimilarity ahead of the flat-to-curved transition due to the pressure gradient in that region. Farther downstream, on the curved section, the difference is more pronounced because the free-stream flow over the curved wall sustains a mean shear and hence production of turbulence kinetic energy.

Besides the FST input, the wall geometry induces a pressure gradient responsible for turning the oncoming flow, which has profound implications on boundary layer dynamics. Figure 5.3 shows the streamwise pressure gradient, $\partial\overline{p}/\partial\xi$, and wall-pressure coefficient, $C_{pw} \equiv (\overline{p}_{\xi,\eta=0} - \overline{p}_{\xi=0,\eta=0})/\frac{1}{2}\rho U_\infty^2$. Both quantities naturally delineate three regions: approximately zero-pressure-gradient (ZPG) boundary layer on the flat plate (Region 0), adverse-pressure-gradient (APG) flow near the onset of the curvature (Re-

Zone	Description	ξ	φ	$Re_{\tau,REF}$	$Re_{\tau,FRC}$
Region 0	ZPG on flat plate	-100	–	455	480
Region 1	APG near onset of curvature	0	0°	363	463
		+50	15°	461	623
Region 2	ZPG on concave curvature	+100	30°	557	769
		+200	60°	762	1027

Table 5.2: Summary of main analysis locations selected based on C_{pw} in figure 5.3.

gion 1), and nearly ZPG flow on the concave curve (Region 2). Table 5.2 provides the information of stations which will be discussed in the following section. Region 0 has been the focus of numerous previous studies of the boundary-layer response to external turbulence [20, 29, 87], and hence the focus herein is directed to Region 1 and Region 2.

5.3 Influence of FST on the boundary-layer state: a statistical perspective

The present simulations involve the combined effects of pressure gradient, curvature and free-stream turbulence on the boundary layer. The outcome is expectedly complex. In this section, we examine the overall changes in the statistical state of

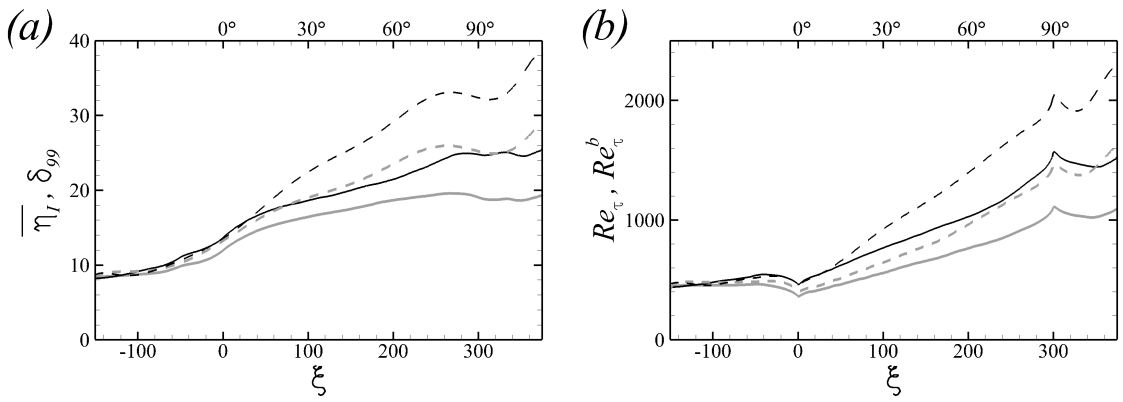

Figure 5.4: (a) Downstream development of (—) the mean interface height based on levelset function $\overline{\eta_I}$ and (- - -) the boundary-layer thickness δ_{99}. (b) Downstream dependence of the friction Reynolds numbers (—) $Re_\tau \equiv u_\tau \overline{\eta_I}/\nu$ and (- - -) $Re_\tau^b \equiv u_\tau \delta_{99}/\nu$. (gray) REF; (black) FRC.

the flow. Unlike flat-plate boundary layers, the tangential free-stream velocity on the curved section is not uniform. For this purpose, the notion of potential velocity U_p will be helpful, where U_p is given by the linearly increasing tangential velocity profile in the free stream. The profile is linearly extended into the boundary layer and its wall value is denoted U_{pw} [5].

Free-stream turbulence is known to enhance mixing near the edge of the boundary layer and as a result increases its thickness. Figure 5.4a reports two quantities that examine this effect: (i) $\overline{\eta_I} = \overline{\eta(\psi = 0.5)}$ which is the mean height of the virtual interface that distinguishes the boundary layer and the free stream using the levelset function and (ii) the 99% thickness δ_{99} defined as the wall-normal location where $\overline{u_\xi} = 0.99U_p$. Both thickness metrics increase appreciably near the onset of the curvature due to the adverse pressure gradient. However, over the curve in Region 2,

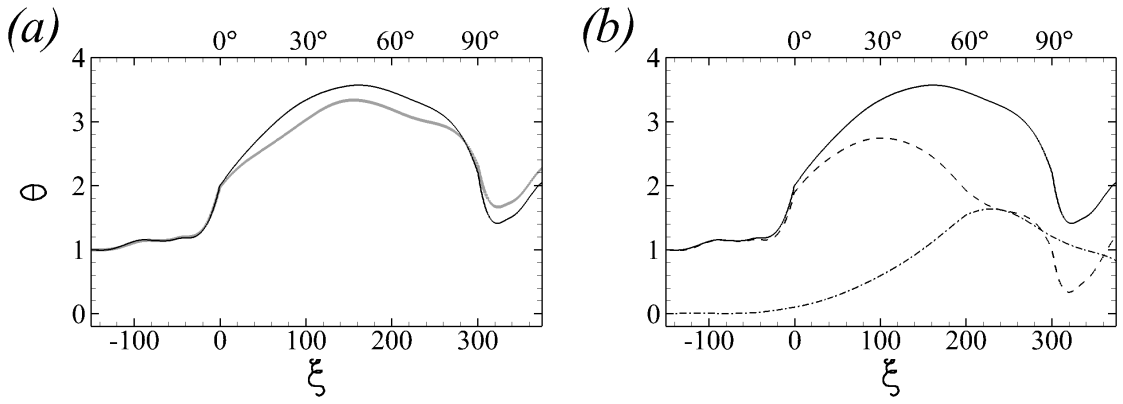

Figure 5.5: (a) Development of momentum thickness θ in (gray) REF and (black) FRC. (b) For FRC, equation (5.2) further decomposes (—) θ into (- - -) $\frac{(U_{pw})^2}{(U_{pw,R})^2}\tilde{\theta}$ and (- · -) $\int_0^{\eta_p} \frac{\overline{u_\xi}}{U_{pw,R}} \left(\frac{U_{p,R}}{U_{pw,R}} - \frac{U_p}{U_{pw,R}} \right) d\eta$.

the mean height of the material line $\overline{\eta_I}$ has a depressed growth relative to δ_{99} which is known to be sensitive to details of the mean-velocity profile. Since $\overline{\eta_I}$ has a physical interpretation, it will be adopted when possible in the rest of this work. The ratio of the boundary-layer thickness to the radius of the curved wall is $\overline{\eta_I}/R < 0.13$ (and $\delta_{99}/R < 0.17$), which places the present flows in the regime of moderate-curvature effect according to the criterion by Patel and Sotiropoulos [67]. The downstream dependence of the friction Reynolds numbers, $Re_\tau \equiv u_\tau \overline{\eta_I}/\nu$ and $Re_\tau^b \equiv u_\tau \delta_{99}/\nu$ is plotted in figure 5.4b. Even though $\overline{\eta_I}$ and δ_{99} increase rapidly near the onset of the curvature, the adverse pressure gradient decreases u_τ and the Reynolds numbers. The higher recorded values of Re_τ in the FRC case are due in part to the larger boundary-layer thickness, and also an increase in the wall stress in presence of FST.

The change in the boundary-layer thickness has a unique effect in the present

configuration because it alters the apparent curvature and turning of the external flow. The first evidence is seen in the momentum thickness, which is also an important proxy of the state of the boundary layer. Various definitions have been proposed for curved-wall flows, and we here consider the form adopted by Patel [65],

$$\theta = \int_0^{\eta_p} \frac{\overline{u_\xi}}{U_{pw,R}} \left(\frac{U_{p,R}}{U_{pw,R}} - \frac{\overline{u_\xi}}{U_{pw,R}} \right) d\eta. \tag{5.1}$$

The subscript R indicates that we are adopting the profile of the potential velocity from the REF case, which is not necessarily preserved in the FRC case. For this reason, we also perform the integration up to the wall-normal position η_p where the potential-velocity profiles from both REF and FRC intersect. The downstream dependence of θ is reported in figure 5.5*a* which shows the anticipated increase in the momentum thickness near $\xi = 0$ due to flow deceleration. On the curved wall θ is larger in the FRC case; this effect is seemingly consistent with flat-plate boundary layers where the change in θ can be directly related to increase in skin friction under free-stream turbulence forcing. The reality is, however, more complex as can be shown by re-expressing the momentum thickness as,

$$\theta = \frac{(U_{pw})^2}{(U_{pw,R})^2} \underbrace{\int_0^{\eta_p} \frac{\overline{u_\xi}}{U_{pw}} \left(\frac{U_p}{U_{pw}} - \frac{\overline{u_\xi}}{U_{pw}} \right) d\eta}_{=\tilde{\theta}} + \int_0^{\eta_p} \frac{\overline{u_\xi}}{U_{pw,R}} \left(\frac{U_{p,R}}{U_{pw,R}} - \frac{U_p}{U_{pw,R}} \right) d\eta. \tag{5.2}$$

The first term involves a momentum thickness $\tilde{\theta}$ defined using the potential velocity of each flow (instead of adopting $U_{p,R}$ for both REF and FRC), and the second term is due to the difference of the potential velocities in the two simulations. Figure 5.5*b* shows that the increase in θ in FRC is due to this second term. The thicker boundary

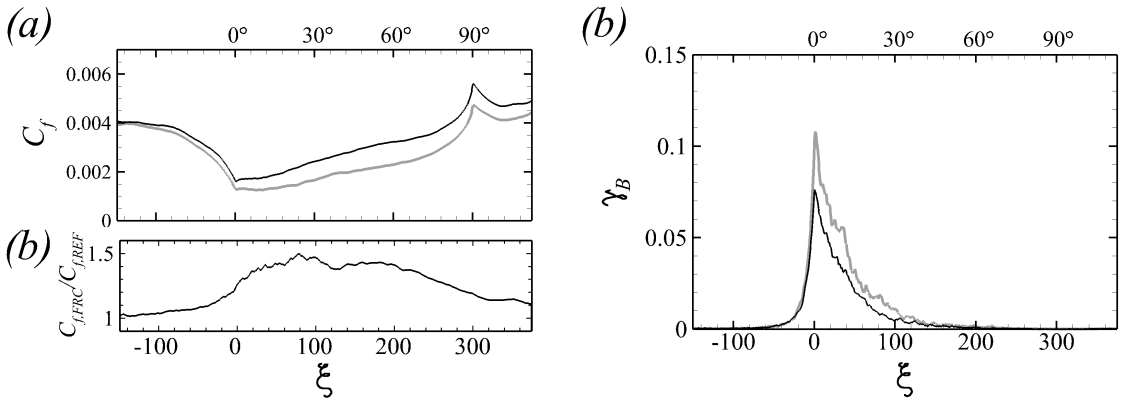

Figure 5.6: Downstream dependence of (a) the mean skin-friction coefficient C_f, (b) $C_{f,FRC}/C_{f,REF}$ and (c) backward-flow intermittency factor γ_B. (gray) REF and (black) FRC.

layer in the forced case increases the effective curvature, specifically $\overline{\eta_I}/R$ or similarly δ_{99}/R, and hence turning of the outer flow. The result is a steeper U_p profile in the free stream, a lower U_p inside the boundary layer and increased deficit $U_{p,R} - U_p$. Modeling this flow or interpreting seemingly banal and established quantities, such as the momentum thickness, must therefore take such effects into account.

Much of the interest in concave-wall boundary layers beneath vortical forcing has been dedicated to the impact on skin friction [42, 43]. Figure 5.6a shows the downstream development of $C_f \equiv \overline{\tau_w}/\frac{1}{2}\rho U_\infty^2$ where $\overline{\tau_w}$ is the mean wall-shear stress. The largest relative increase in C_f when the flow is forced is on the order of 49%, which is appreciably higher than the 15% observed for the same flow conditions over a flat plate (§3.4.1). Note that the increase is not limited to the low C_f region near the onset of curvature; instead it is sustained above 40% over the majority of Region 2 on the curved wall. While the effect of forcing appears relatively modest at the

onset of curvature, an important change in the state of the flow takes place in that region due to the flow deceleration. As the curvature is approached, the skin friction drops precipitously due to the adverse pressure gradient in both REF and FRC cases. In the latter, FST enhances momentum mixing, which leads to a more moderate reduction of C_f. However, the statistically positive value of C_f masks an intermittent separation that takes place in that region. This intermittency, or probability, of negative instantaneous wall-shear stress is denoted γ_B and is plotted in figure 5.6*b*; its reduced value in FRC is noteworthy due to the qualitative change in boundary layers at separation.

An elegant interpretation of separation is in terms of the spanwise vorticity and its wall flux; the latter is due to the streamwise pressure gradient [52]. Figure 5.7*a* shows the spanwise vorticty distribution near the wall. At the onset of curvature, the depletion of negative vorticity is less pronounced in the FRC case, which can be interpreted in terms of a reduction in its mean outflux at the wall. A more detailed view is provided in figure 5.7*b* which reports the probability density function (PDF) of instantaneous outflux of negative vorticity at the onset of curvature. The integral of the PDF yields a smaller value for the FRC case, consistent with figure 5.7*a*. The PDF of the forced case also has larger positive and negative tails, i.e. stronger instantaneous outflux of negative vorticity (positive values) and also influx (negative values). The former alone would be at odd with reduced frequency of separation. However, the strong influx of negative vorticity (negative values) renders the state of

the boundary layer less prone to separation. Intuition may suggest that this effect is associated with enhanced momentum mixing on the flat upstream section, due to the additional vortical motions from the free stream that may breach the boundary layer. However, recent results for flat-plate flows showed that the free-stream turbulence does not reach the buffer layer. Instead, the external forcing has an indirect effect of modulation of the near-wall region that enhances the near-wall turbulent shear stresses (§3.5). The resulting energetic near-wall flow is then less prone to separation at the onset of curvature. Two vertical lines are marked on figure 5.7*b*; events with higher amplitudes than these thresholds have the same probability as separation (9.73% for REF and 7.39% for FRC). Based on this simple conceptual model, the results indicate that the threshold required for the forced boundary layer to undergo local intermittent separation is approximately 30% higher than REF. The mean-flow profile $\overline{u_\xi}$ is therefore anticipated to be fuller in the forced flow, and is shown in figure 5.8. Indeed, at $\xi = 0$ through $\xi = 50$, the near-wall region of the FRC boundary layer carries more momentum than the reference case.

The changes to the mean profile as the flow traverses from the APG Region 1 to the ZPG Region 2 on the curve are noteworthy (figure 5.8): Firstly, the figure shows the subtle but important effect of the change in the outer potential velocity that was referenced earlier. Secondly, the acceleration of the near-wall flow $0 < \eta/\overline{\eta_I} \leq 0.5$ is much more pronounced in the forced boundary layer.

Based on previous studies, whether naturally occurring Görtler vortices play a

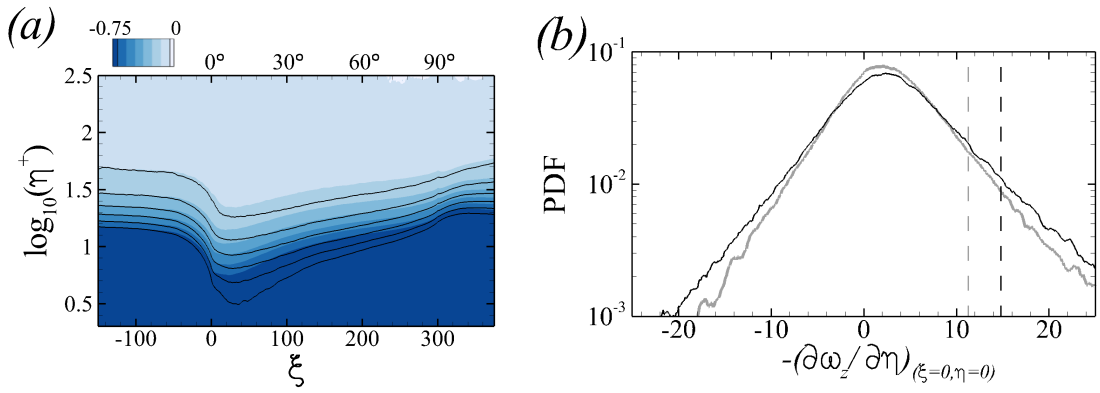

Figure 5.7: (a) Mean spanwise vorticity $-0.75 \leq \overline{\omega_z} \leq 0$ of (lines) REF and (color) FRC cases. (b) PDF of $-\partial\omega_z/\partial\eta$ at the wall at the onset of the curvature, $(\xi, \eta) = (0, 0)$. Dashed lines mark thresholds for higher amplitude events having the same probability as intermittent separation. (gray) REF and (black) FRC.

role in this regime is difficult to assert because they have been elusive. For example, unable to identify Görtler vortices directly in curved wall boundary layers, Barlow and Johnston [6] resorted to artificially imposing them using vortex generators. Should Görtler vortices exist in our configuration, we must identify them and quantify their effect on the near-wall flow, be that an indirect process akin to the modulation of near-wall stresses by outer large-scale motions in the flat-plate boundary layer or a direct effect. In addition, how these interactions change in presence of the free-stream turbulence is of primary interest. Statistical evidence is considered here, followed by a discussion of the turbulence structures in the next section.

Evidence of persistent, or statistically relevant, Görtler structures is sought by plotting the turbulence stresses in figure 5.9(a, b), for both the quiescent and turbulent free stream cases. The colour contours show the tangential component, and the lines show the (black) wall-normal and (gray) spanwise ones. The first observation is a

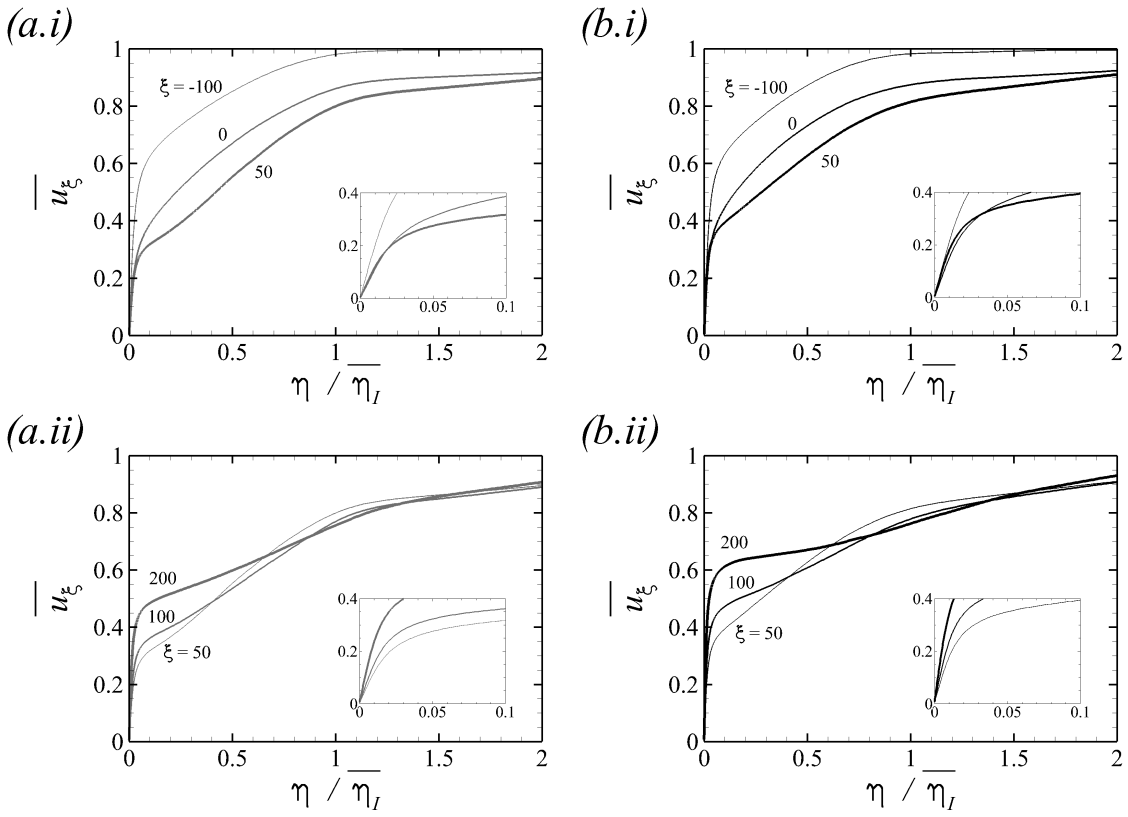

Figure 5.8: Downstream development of the mean streamwise velocity in (a) REF and (b) FRC. (i) Progression from the flat-plate ZPG Region 0 to APG Region 1, and (ii) from APG Region 1 to ZPG Region 2 along the curve.

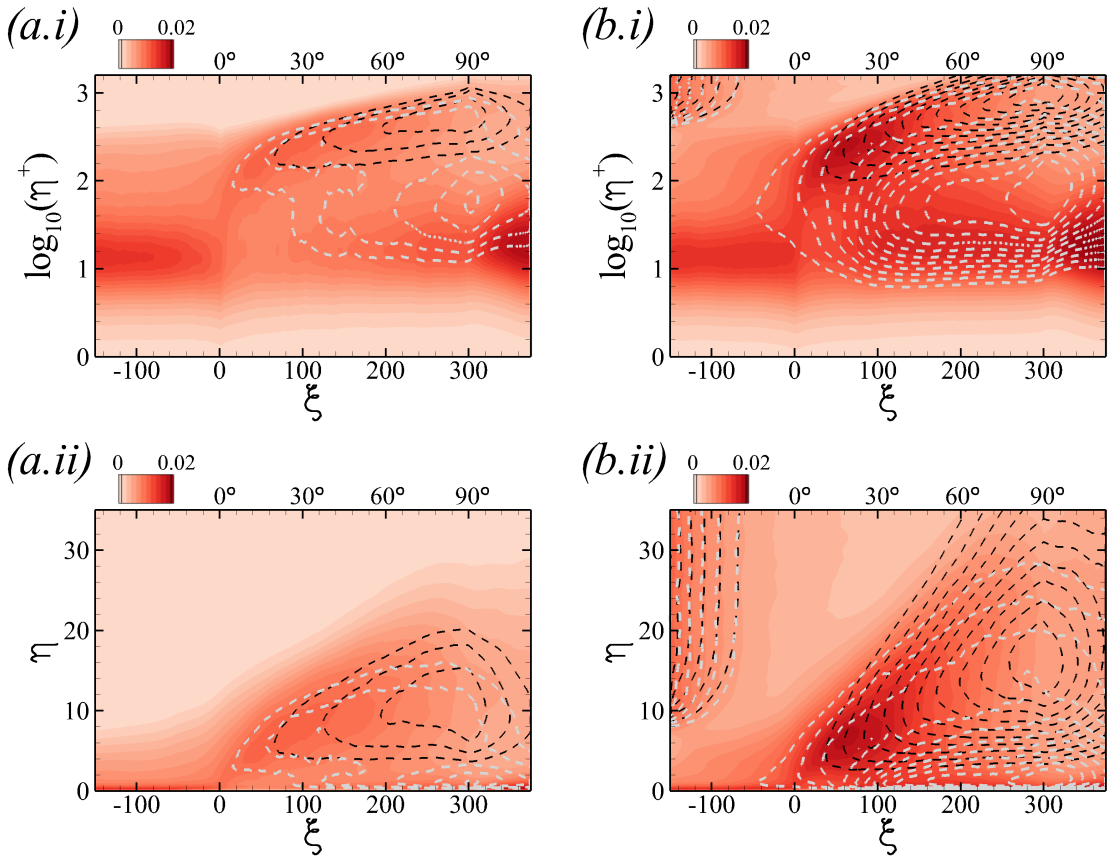

Figure 5.9: Reynolds Normal stresses for (a) REF and (b) FRC. The wall-normal coordinate is normalized using (i) viscous and (ii) outer scales. Colours correspond to the streamwise stress, and lines show the (black) wall-normal $\overline{u'_\eta u'_\eta}$ and (gray) spanwise $\overline{w'w'}$ stresses, from 5×10^{-3} with increment 1×10^{-3}.

sudden change in the contours of $\overline{u'_\xi u'_\xi}$ across the onset of curvature: The upstream wall-normal profile of $\overline{u'_\xi u'_\xi}$ has only one maximum in the buffer layer, but beyond $\xi = 0$ two maxima can be detected: The inner peak retains its original height within the buffer layer $\eta^+ \approx 11$, decays quickly due to adverse pressure gradient, and shows faster recovery in the forced flow; In contrast the outer peak is in the logarithmic layer and shifts away from the wall with the downstream growth of the boundary layer. The emergence of the outer peak at that onset of curvature is consistent with APG [see e.g. 32], which is sufficiently large to induce intermittent separation. In addition, relative to the reference case, free-stream turbulence enhances the intensity of these structures—an effect that is anticipated based on previous studies of forced flat-plate boundary layers.

Observations in connection with the tangential stress are not, however, the most important to note from this figure if interest is in the Görtler structures. Instead, attention is drawn to the wall-normal $\overline{u'_\eta u'_\eta}$ and spanwise $\overline{w'w'}$ stresses in Region 2. Both stresses amplify on the curved wall, which is consistent with earlier studies [3, 5, 54], and the present results show that the effect of free-stream forcing is rather pronounced. In the lower panels (*a.ii* and *b.ii*), the wall-normal coordinate is normalized by the inlet boundary-layer momentum thickness, which highlights that the separation between the peak $\overline{u'_\eta u'_\eta}$ and $\overline{w'w'}$ increases downstream. We interpret the increase in $\overline{u'_\eta u'_\eta}$ and $\overline{w'w'}$ as the first, perhaps indirect evidence of Görtler structures (further evidence provided in §5.4). In reality, instantaneous structures may form

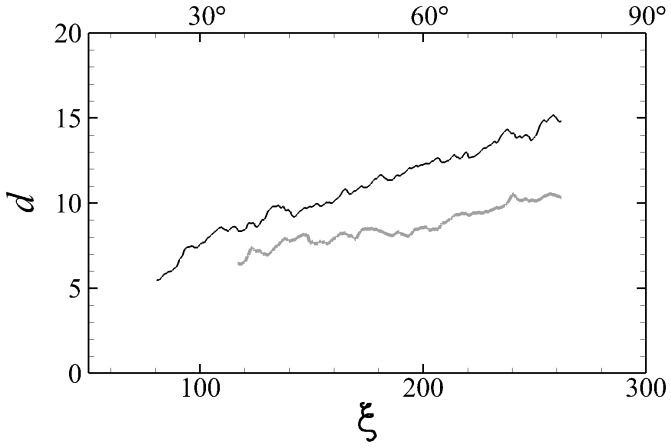

Figure 5.10: Separation distance d between the peaks of $\overline{u'_\eta u'_\eta}$ and $\overline{w'w'}$. (Gray) REF and (black) FRC.

at various heights in the boundary layer, meander, decay or be overtaken by other structures. For these reasons, in the statistical interpretation, we regard the peaks of $\overline{u'_\eta u'_\eta}$ and $\overline{w'w'}$ as only indicative of the locations of the Görtler structures, and hence the separation distance d between their peaks as indicative of the size of the vortices. Figure 5.10 shows the increase of that size d with downstream distance, more so in the forced flow in light of the stronger amplification of the outer large-scale structures and the faster growth of the boundary layer.

The departure from isotropy $I = \overline{u'_\xi u'_\xi}/2k - \frac{1}{3}$ succinctly captures the changes of the perturbation field within the boundary layer, across the onset of curvature and on the curved wall. Figure 5.11 shows that upstream of $\xi \approx 100$, large values of I are sustained in the outer region, consistent with the lifting of streaky structures across the adverse pressure gradient region. For example, Lian [51] visualized that

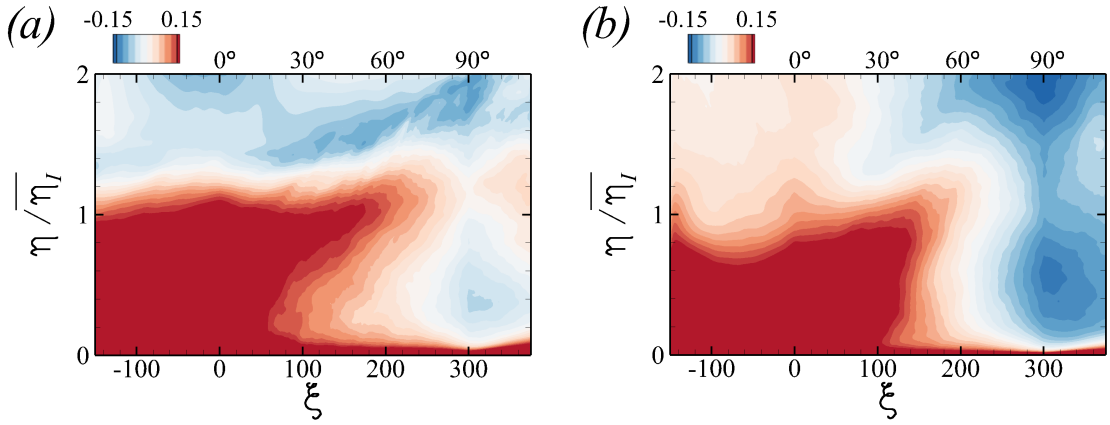

Figure 5.11: Deviation of Reynolds normal stresses from isotropy, $I = \overline{u'_\xi u'_\xi}/2k - \frac{1}{3}$. ($a$) REF and ($b$) FRC.

boundary-layer structures are lifted up and bent at approximately 45° relative to the wall in the APG turbulent boundary layers. With downstream distance on the curved section, I is reduced and in fact becomes negative due to the enhancement of $\overline{u'_\eta u'_\eta}$ and $\overline{w'w'}$, which are associated with the vortex structure. In the forced case, stronger Görtler structures are consistent with more appreciable decrease of I.

The changes in the normal stresses are paralleled by changes in the production of turbulence kinetic energy, $\mathcal{P} \equiv -\overline{u'_i u'_j}\frac{\partial \overline{u_i}}{\partial x_j}$, which is reported in figure 5.12. Since a logarithmic scale is adopted in the wall-normal direction, the contours show the pre-multiplied quantity $\eta^+\mathcal{P}$ in order to reflect the contribution to the wall-normal integral. Also note that two contour levels are adopted in each figure, with larger range for the outer region of the boundary layer above the curved surface. On the flat upstream section, the inner and outer peaks make comparable contributions to the integrated production, and both are enhanced by free-stream turbulence—an effect

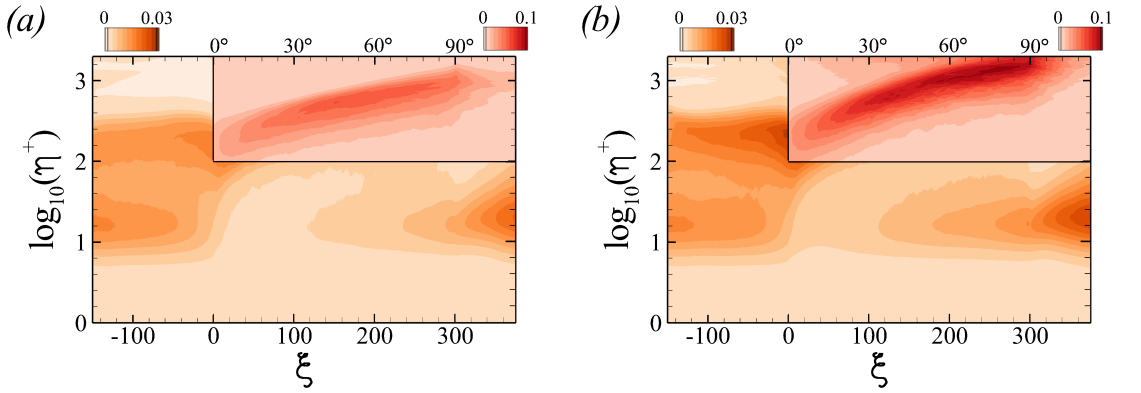

Figure 5.12: Contours of pre-multiplied turbulence kinetic-energy production, $\eta^+\mathcal{P}$. (a) REF and (b) FRC.

that has been detailed in previous chapter §3.4.2. The adverse pressure gradient at the flat-to-curved transition suppresses the near-wall production, and recovery is slow on the curved region albeit faster in presence of free-stream turbulence. In the outer region of the curved-wall boundary layer ($\xi \geq 0$), the production peak is significantly enhanced. While its initial amplification near the onset of curvature coincides with the lifting of near-wall streaks due to APG, its continued amplification downstream coincides with the amplification of the outer stresses and potentially the formation and amplification of Görtler structures. In presence of free-stream forcing, the magnitude of that outer peak is nearly twice its value in the reference configuration.

The TKE production in the outer region is significantly affected by Reynolds shear stresses. We first recall results from forced flat-plate boundary layers for comparison: Even when the free-stream turbulence is isotropic, and hence free of average shear stress, it enhances $-\overline{u'_\xi u'_\eta}$ within the boundary layer although it reduces the stress

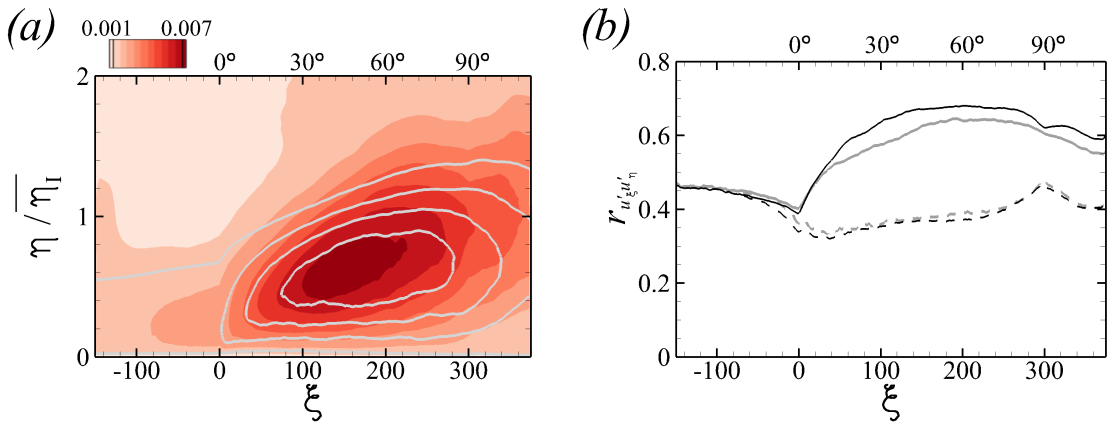

Figure 5.13: (a) Reynolds shear stress $-\overline{u'_\xi u'_\eta}$ for (line) REF and (color) FRC cases. Contours lines correspond to levels from 1×10^{-3} with increment 1×10^{-3}. (b) Downstream development of shear-stress correlation coefficient $r_{u'_\xi u'_\eta}$, extracted at (- - -) $\eta^+ = 10$ and (——) wall-normal location of the maximum. (Gray) REF and (black) FRC.

correlation coefficient $r_{u'_\xi u'_\eta} \equiv -\overline{u'_\xi u'_\eta}/u'_{\xi,rms}u'_{\eta,rms}$ [29, 81]. The shear stress and its correlation coefficient for the present curved-wall boundary layers are reported in figure 5.13. The former quantity is plotted throughout the boundary layer, and the latter is extracted at select locations. Over the curved section, $-\overline{u'_\xi u'_\eta}$ increases appreciably and reaches larger values for the FRC case. Figure 5.13b shows the correlation coefficient at $\eta^+ = 10$ and at the wall-normal height where it is maximum. The figure shows that the peak occurs at $\eta^+ = 10$ on the flat section of the wall, but the correlation at that location decays due to the pressure gradient [26]. Note that this effect was not reported in the previous experimental curved-wall studies by Barlow and Johnston [5] who removed the effect of pressure gradient by contouring the top convex wall. On the curved wall, however, the peak shifts higher in the

boundary layer and is much larger in magnitude due to the coherence of the turbulence structures in that region. In addition, the coefficient of the forced case is markedly greater in the outer region than that of the reference flow. We anticipate that the FST strengthens the outer roll motion on the curved region, thereby enhancing the correlation coefficient.

This section has demonstrated that the turbulence on the curved wall is modified by geometric effects, including streamwise pressure gradient and centrifugal forces. The distribution of the turbulent stresses suggests the formation of naturally triggered Görtler structures, which have evaded a definitive characterization on curved walls in previous simulations and experiments [e.g. 3, 6, 54]. In addition, these evidences were more pronounced when the boundary layer develops underneath free-stream turbulence. The following section upholds these interpretations by directly probing the flow structures on the curved wall without and with FST.

5.4 Modification of boundary-layer structures

A commonly adopted approach to identifying coherent vortical motions is to evaluate an invariant of the velocity gradient tensor, for example $Q \equiv \Omega_{ij}\Omega_{ij} - S_{ij}S_{ij}$ where S_{ij} is the symmetric, rate-of-deformation tensor and Ω_{ij} is the anti-symmetric, spin tensor. Figure 5.14 shows iso-surfaces of the Q-criterion coloured by their wall-

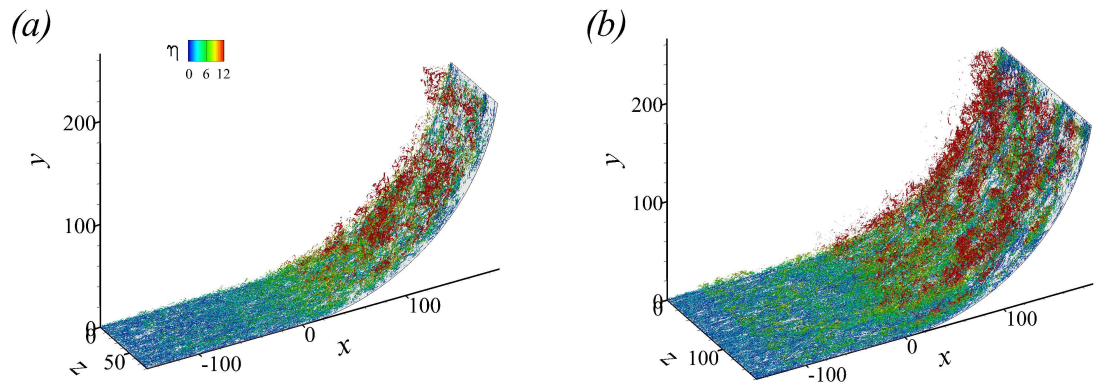

Figure 5.14: Iso-surface of Q-criterion with threshold $Q = 0.03$, coloured by $0 \leq \eta \leq 12$. (a) REF and (b) FRC.

normal distance. In both REF and FRC, the structures grow and spread in η as they travel into the concave curvature; similar observations were made for FST-free flows [3]. This trend is consistent with the development of the outer peak in the profiles of Reynolds stresses (figures 5.9). The increase in vortical activity has previously been attributed to Görtler vortices due to the centrifugal effect, although coherent large-scale vortical structures are not apparent in the figure. It is also important to note that the response in presence of FST is hardly distinguishable from the reference flow, based on the instantaneous Q iso-surfaces. While streamwise organization is visually discernible in the figure, Görtler vortices which are associated with coherent longitudinal roll motions can not be easily identified, and attempts to adopt filtering techniques were not successful.

While it is often difficult to identify coherent roll motions in wall turbulence, the associated displacement of mean momentum generates coherent tangential velocity

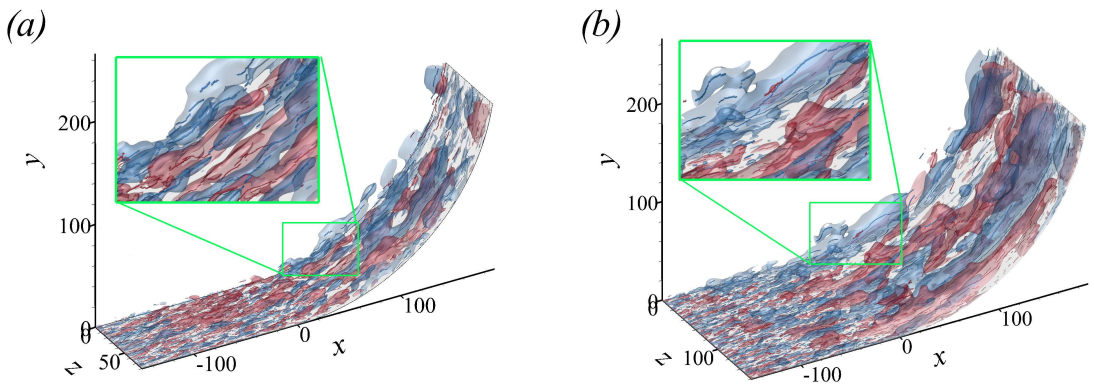

Figure 5.15: Iso-surfaces of filtered streamwise velocity, (red) $\hat{u}'_\xi = +0.06$ and (blue) $\hat{u}'_\xi = -0.06$. Lines within the transparent surfaces mark the cores of the structures. (a) REF and (b) FRC.

perturbations that are more readily observable. Following the approach described by [49], we identify the large-scale tangential velocity structures by evaluating iso-surfaces of Gaussian-filtered $\hat{u}'_\xi$ (see figure 5.15). In order to interpret the present results, it is helpful to recall those for a flat plate at the same Reynolds numbers §3.5: In that case, a canonical boundary layer without free-stream forcing does not develop outer large-scale motions; under free-stream turbulence, large-scale structures form and amplify, but a much longer streamwise extent is required than the flat region in the present configuration. Contrasting REF and FRC for $\xi < 0$, the velocity structures appear similar in that region, and hence any differences downstream on the curved wall are due to the interaction in that regime. There, the outer structures are clearly visible, and the iso-surfaces are larger in presence of free-stream forcing which also implies that the tangential velocities within their cores are higher in amplitude. In addition, at least for this particular instance of the flow, the low-speed, or negative,

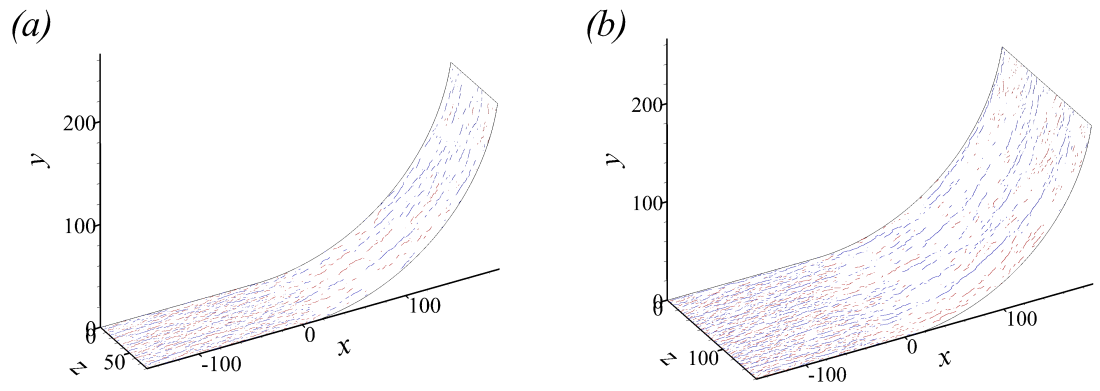

Figure 5.16: Cores of the filtered structures (blue) $\mathcal{C}^N$ and (red) $\mathcal{C}^P$, near the wall ($\eta^+ < 30$). (a) REF and (b) FRC.

motions are much pronounced than positive ones although a quantitative comparison is needed.

Visualization of the large-scale outer motions on the curved wall (figure 5.15) conceals the structures near the wall. To reveal the changes in that region, the cores of the filtered structures are differentiated into outer and inner ones based on their heights relative to $\eta^+ = 30$. Cores are subsequently classified based on the faster $\mathcal{C}^P$ ($\hat{u}'_\xi > 0$) and slower $\mathcal{C}^N$ ($\hat{u}'_\xi < 0$) structures. Relative to the upstream flat plate, the number of near-wall structures on the curved wall is reduced, as shown in figure 5.16. This initial reduction is due to APG [59], but the lack of recovery in the ZPG Region 2 is connected to the modulation by the outer large scale motions [37].

Definitive evidence of the outer roll, or Görtler, motions and their influence on the near-wall flow are sought by computing conditionally averaged velocity perturbation fields. The condition adopted for averaging is the existence of a core of an outer

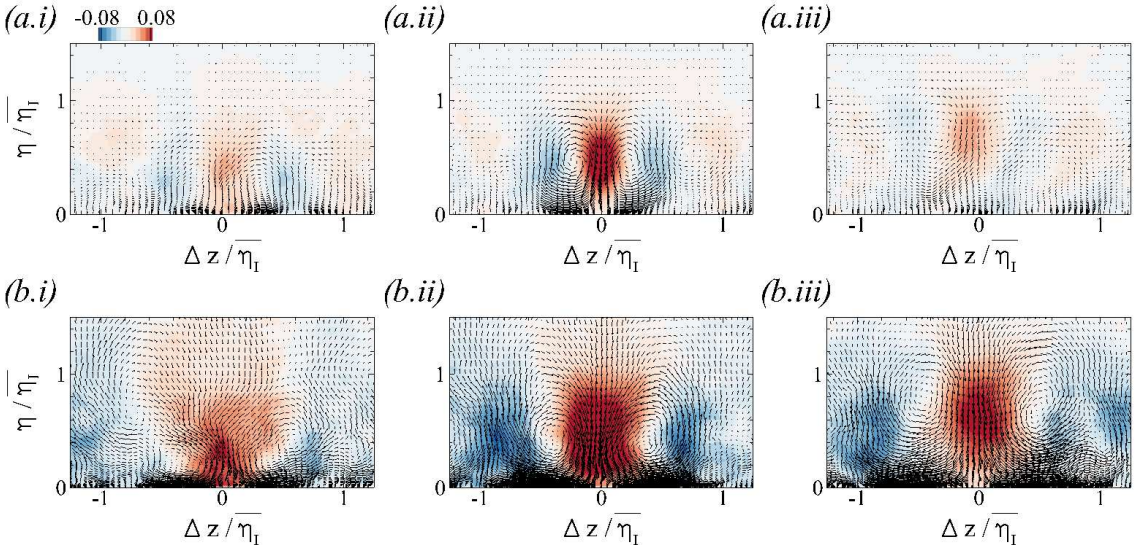

Figure 5.17: Conditionally averaged positive streamwise velocity on the curve with reference position $\xi_o = 100$ (30° station), and coloured by $u'^{P}_{\xi_\mathcal{L}}$. Black vectors are $(u'^{P}_{\eta_\mathcal{L}}, w'^{P}_{\mathcal{L}})$. (a) REF, (b) FRC, (i) $\Delta\xi = -25$, (ii) $\Delta\xi = 0$, and (iii) $\Delta\xi = +25$.

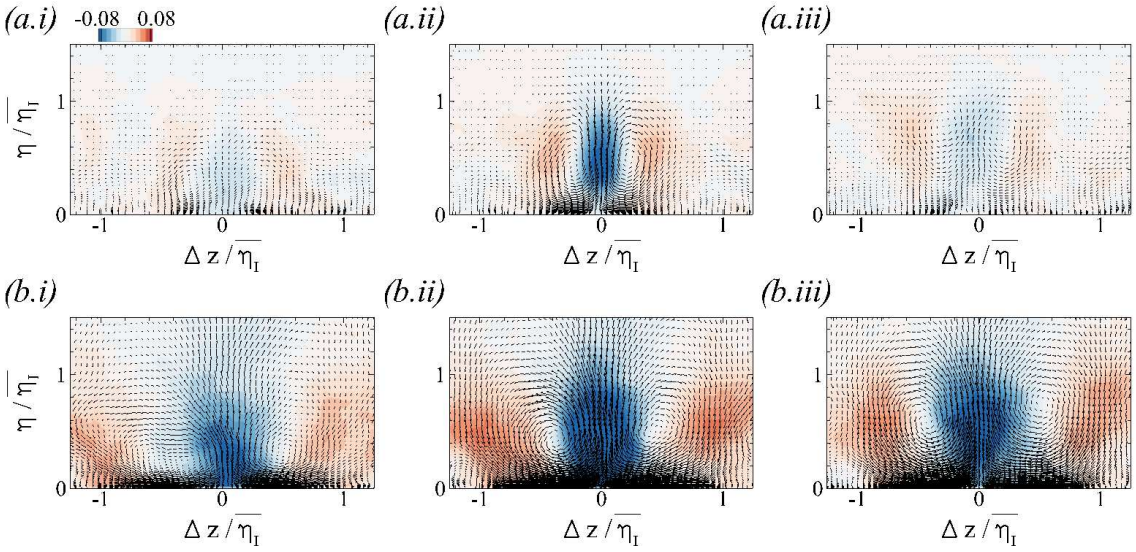

Figure 5.18: Conditionally averaged negative streamwise velocity on the curve with reference position $\xi_o = 100$ (30° station), and coloured by $u'^{N}_{\xi_\mathcal{L}}$. Black vectors are $(u'^{N}_{\eta_\mathcal{L}}, w'^{N}_{\mathcal{L}})$. (a) REF, (b) FRC, (i) $\Delta\xi = -25$, (ii) $\Delta\xi = 0$, and (iii) $\Delta\xi = +25$.

tangential velocity structure, and is further differentiated into positive and ones similar to the instantaneous visualization (c.f. figures 5.15). The conditionally averaged perturbation fields are therefore,

$$\mathbf{u}^P_{\mathcal{L}}(\Delta\xi,\eta,\Delta z) = \overline{\mathbf{u}(\xi_o+\Delta\xi,\eta,z+\Delta z) \;\mid\; \mathcal{C}^P}_{|30<\eta^+<\eta^+_I}, \tag{5.3}$$

$$\mathbf{u}^N_{\mathcal{L}}(\Delta\xi,\eta,\Delta z) = \overline{\mathbf{u}(\xi_o+\Delta\xi,\eta,z+\Delta z) \;\mid\; \mathcal{C}^N}_{|30<\eta^+<\eta^+_I}. \tag{5.4}$$

Figures 5.17 and 5.18 show the contours of $\mathbf{u}^P_{\mathcal{L}}$ and $\mathbf{u}^N_{\mathcal{L}}$, with the reference streamwise position $\xi_o = 100$ (30° station). Vectors represent the in-plane velocity components. While the outer roll motions are visible at $\Delta\xi = 0$ in the canonical boundary layer, they are much more pronounced (larger in size and amplitude) beneath free-stream turbulence. The more important observation, however, is the persistence of the roll motion and associated tangential velocity response upstream and downstream of the reference position. In the quiescent flow, the perturbation field $u'^{\{P,N\}}_{\xi_{\mathcal{L}}}(\Delta\xi = \pm 25)$ is decorrelated appreciably from the reference point (e.g. figures 5.17-5.18, *a.i* and *a.iii*). In contrast, in the FRC case, the structures identified at the reference location persist beyond $\Delta\xi = \pm 25$ (e.g. figures 5.17-5.18, *b.i* and *b.iii*). This improved coherence should not be taken for granted, but rather be viewed against the background of free-stream turbulence being free of Reynolds shear stress which may intuitively, but incorrectly, suggest that it would act to decorrelate the wall turbulence. Instead, the free-stream turbulence acts against the weak shear in the outer part of the boundary layer, promotes the shear stress there and spurs the formation and amplification of stronger and larger scale motions.

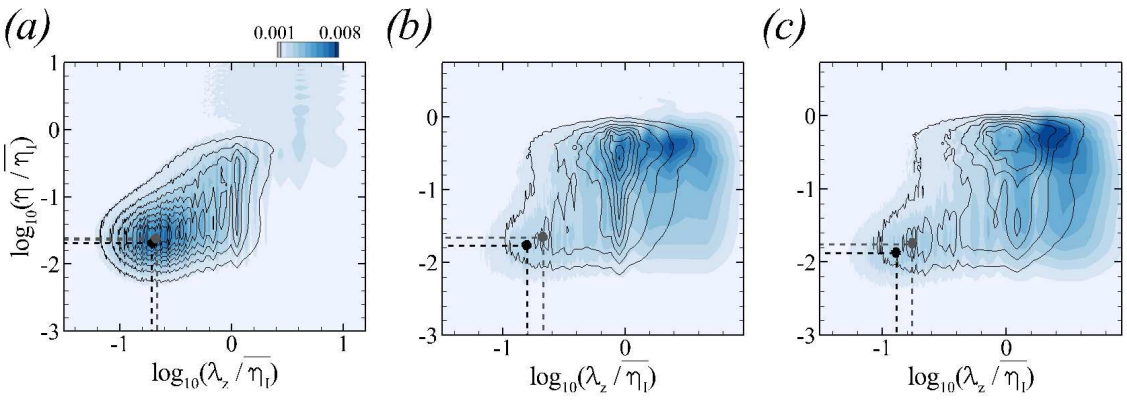

Figure 5.19: Pre-multiplied spanwise energy spectra $0.001 \leq \kappa_z \Phi_{u'_\xi u'_\xi} \leq 0.008$ at (a) $\xi = -100$, (b) $\xi = 50$ and (c) $\xi = 100$. (Black lines) REF and (color) FRC. Filled circles mark $\eta^+ = 10$ and $\lambda_z^+ = 100$ in (gray) REF and (black) FRC.

The outer roll motion also increases in size with downstream distance, from $\Delta\xi = -25$ to $+25$. This view was also supported by further evidence (not shown) where we evaluated the conditional velocity fields using equations (5.3) and (5.4) at reference locations $\xi_o = 75$ and $\xi_o = 125$. The large roll motions which are growing with downstream distance in the forced flow are consistent with earlier statistical evidence based on the Reynolds stress, namely that the gap between the peak $\overline{u'_\eta u'_\eta}$ and $\overline{w'w'}$ increases along the curved wall (c.f. figure 5.10).

The coherent outer roll motions have important implications, including their recognized role in modulating the near-wall structures—an effect that we will quantify below. Additionally, in the FRC case, they may enhance the transport of free-stream fluid that is itself turbulent towards the wall. Before we investigate these effects in detail, we examine the spectra of these outer perturbations in order to compare their energy and size relative to other boundary layer disturbances. Figure 5.19 shows the

spanwise energy spectra of the streamwise velocity,

$$\Phi_{u'_\xi u'_\xi}(\lambda_z) = \int_{-\infty}^{\infty} \overline{u'_\xi(z)u'_\xi(z+\zeta)} e^{-i\kappa_z \zeta}\, d\zeta, \tag{5.5}$$

pre-multiplied by spanwise wavenumber $\kappa_z = 2\pi/\lambda_z$ where λ_z is the wavelength. In figure 5.19*a*, on the flat section, only an inner peak is visible, be that in the REF or FRC boundary layer. On the curved section, the energy in the small wavelengths decreases (figures 5.19*b*-*c*), which is consistent with reduced TKE dissipation (not shown). In the reference flow, a clear outer peak emerges at $\lambda_z \approx \overline{\eta_I}$. In contrast, in FRC at 15° (color contour of figure 5.19*b*), there are two outer peaks and both are associated with Görtler motions: The first, at the smaller spanwise wavelength (left), coincides with the contours of the canonical boundary layer and is the naturally forming Görtler vortices. The second emerges at the wavelength of the free-stream turbulent forcing (see panel (*a*) above $\eta \geq \overline{\eta_I}$); this peak is the boundary layer Görtler response to the external forcing. The two peaks ultimately merge downstream $\xi = 100$, with the larger Görtler vortices becoming the most dominant. An important observation is the extent to which that wavenumber persists, or remains energetic, deep into the boundary layer, which is suggestive of a stronger modulation of the near-wall region than in flat plates, perhaps even a direct influence.

The small-scale energy in the near-wall region is also modified by the free-stream forcing. Figure 5.19 shows that, along the curved wall, energy shifts towards smaller spanwise wavenumbers in FRC which is consistent with enhanced dissipation. The inner peak in the spectra is generally located at $\eta^+ \approx 10$ and $\lambda_z^+ \approx 100$, and thus

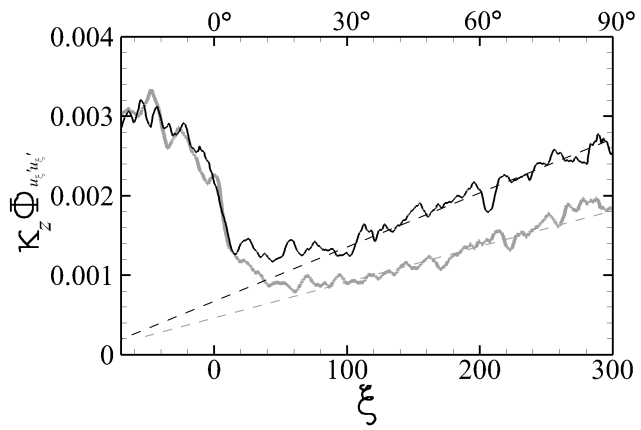

Figure 5.20: Downstream development of $\kappa_z \Phi_{u'_\xi u'_\xi}$ at $\eta^+ = 10$ and $\lambda_z^+ = 100$: (gray) REF and (black) FRC. Dashed lines indicate the recovery rate in Region 2.

the downstream dependence of $\kappa_z \Phi_{u'_\xi u'_\xi}$ at the position is provided in figure 5.20. Downstream of the fast decay associated with the adverse pressure gradient at the onset of curvature, $\kappa_z \Phi_{u'_\xi u'_\xi}$ recovers at a faster rate for FRC.

An objective measure of penetration of the free-stream fluid into the boundary layer is the intermittency γ. Starting from the levelset function that provides an objective instantaneous virtual interface between the two regions, an indicator function is defined $\Gamma = \{0, 1\}$ based on ψ, and then averaged to obtain $\gamma = \overline{\Gamma}$. We recall that in a flat-plate boundary layer, §3.4 adopted the same measure and demonstrated that the free-stream turbulence does not breach the buffer layer. The results for the present curved wall configuration are reported in figure 5.21, and show remarkable levels of penetration of free-stream fluid inside the buffer layer at $\xi \geq 100$ ($\varphi > 30°$, Region 2) due to FST. This enhanced "mixing" is unique to the present configuration

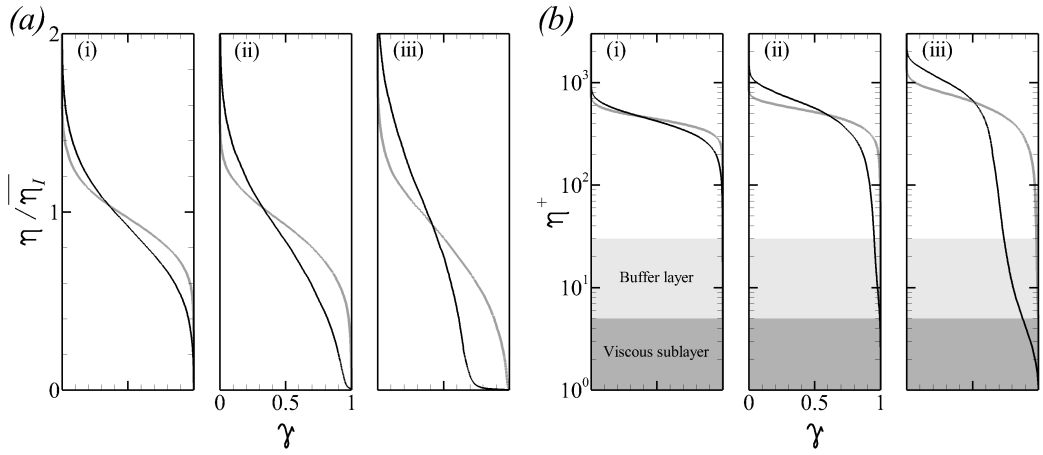

Figure 5.21: Intermittency for (gray) REF and (black) FRC as a function of the wall-normal distance in (a) outer and (b) viscous units, at (i-iii) $\xi = \{-100, 100, 200\}$.

and is precipitated by the large-scale outer roll motions, transporting the free-stream fluid deep towards the wall and ejecting near-wall fluid outwards. The interaction of the outer and inner regions is therefore direct. Ultimately, however, this large-scale effect is also accompanied by further dispersion of the ingested turbulence due to the various flow scales within the boundary layer, and by molecular diffusion acting on the smallest scales. Thus, we next consider the recovery of the near-wall small-scale structures on the curved wall, and in particular their modulation by the outer large scales that can spur that recovery.

Bernardini and Pirozzoli [9] defined the two-point amplitude modulation (AM) coefficient $C_{u_\xi,u_\xi}(\eta_1,\eta_2)$ in order to quantify the influence of the large-scale motion at η_1 on the near-wall motion at η_2, where

$$C_{u_\xi,u_\xi}(\eta_1,\eta_2) = \overline{u_{\xi L}'(\eta_1) u_{\xi EL}'(\eta_2)}, \tag{5.6}$$

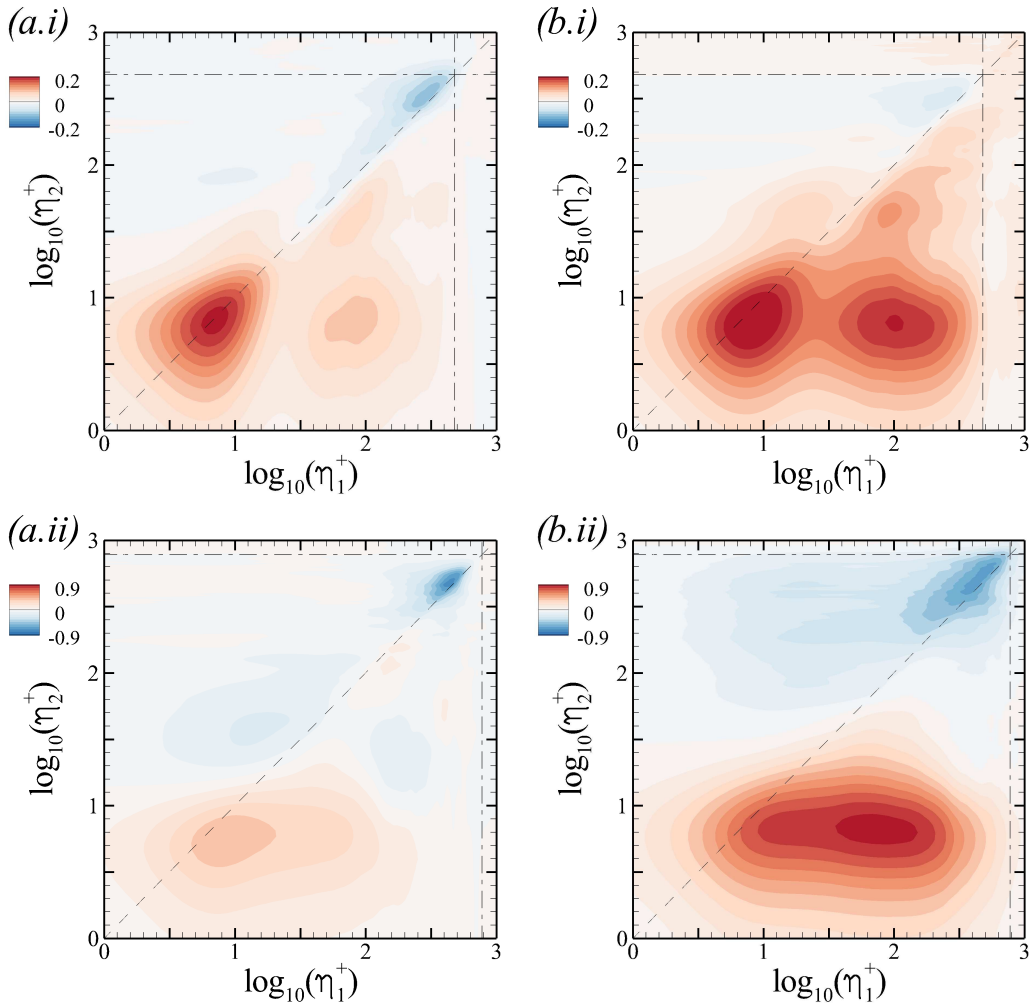

Figure 5.22: Amplitude-modulation coefficient $C_{u_\xi,u_\xi}/u_\tau^2$ for (a) REF and (b) FRC cases. (i) Flat section ($\xi = -50$) and (ii) curved section ($\xi = 100$; 30° station). Vertical and horizontal dash-dotted lines (- · -) mark the edge of the boundary layer, $\eta = \overline{\eta_I}$.

u_{ξ_L}' is a large-scale velocity, and $u_{\xi_{EL}}'$ is a filtered envelope of a small-scale part. The cut-off filter for the large- and small-scale signal is set to $0.5\overline{\eta_I}$, which from the spectra shown in figure 5.19 should discriminate these scales. In the flat section ($\xi = -100$), figure 5.22i shows that upstream boundary layer exhibit a weak level of modulation beneath a quiescent free stream, and this effect is enhanced under FST. In the latter case, the outer large-scale motions at $\eta_1^+ \approx 100$ show relatively higher level of modulation of the small scales at $\eta_2^+ \approx 7$. These results are typical of flat plates, and the values of $C_{u_\xi,u_\xi}(\eta_1,\eta_2)$ would increase downstream if the flat section were extended. A qualitative change takes place over the curved section: Figure 5.22(ii) highlights a much stronger modulation (note the change in the contour levels), especially in the forced flow where the coefficient at $(\eta_1^+,\eta_2^+) \approx (100,7)$ is now the most dominant and is nearly twice as high as without FST. The results for FRC are the outcome of the energetic footprint of the large scales that persists near the wall (figure 5.19) and leads to a faster recovery of near-wall small scales (see figure 5.20).

The deep ingestion of outer fluid by the Görtler structures not only modulates the near-wall scales but also influences the stress at the wall which is of practical interest. In order to empirically demonstrate this connection, figure 5.23(i) shows an instantaneous realization of the skin-friction coefficient c_f, and panels (ii) show the corresponding tangential velocity fluctuations u_ξ' in the outer region. The contours of c_f initially have a streaky pattern that is disrupted by the APG at the onset of curvature, which is consistent with the decrease in the number of near-wall structures

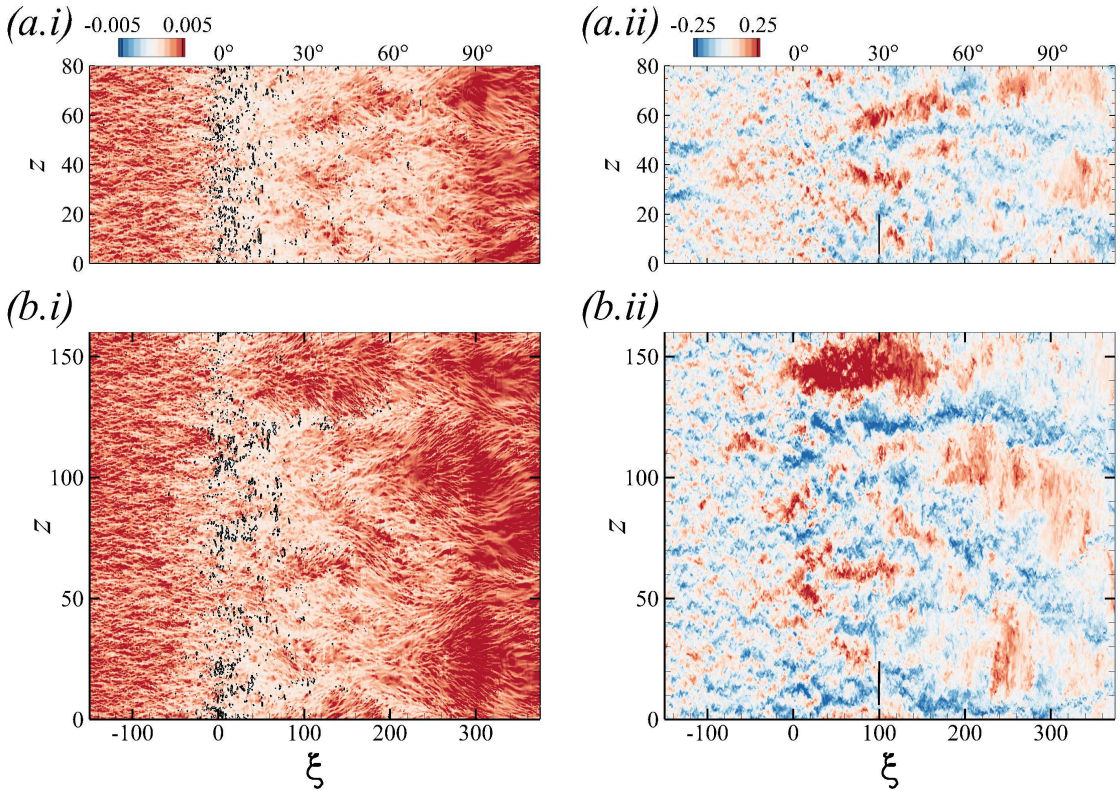

Figure 5.23: (i) Top view of instantaneous skin-friction coefficient, $-0.005 \leq c_f \leq 0.005$ and black isocontour marks $c_f = 0$. (ii) Instantaneous streamwise-velocity fluctuations $-0.25 \leq u'_\xi \leq 0.25$ at $\eta \approx 3$ ($\eta^+ \approx 100$ at $\xi = 0$). (a) REF; (b) FRC. The short black line in (ii) is a graphical length scale equal to $\overline{\eta_I}$ at $\xi = 100$.

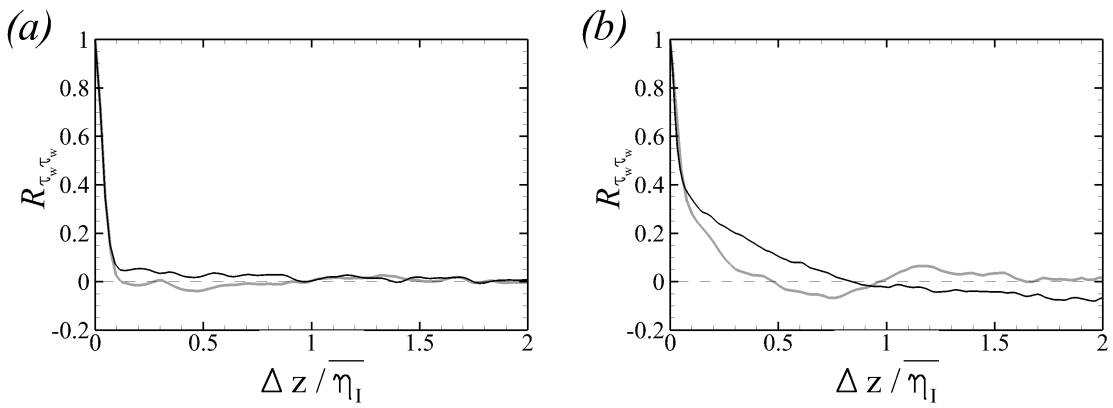

Figure 5.24: Spanwise two-point correlation of the wall-shear stress $R_{\tau_w\tau_w}$ at (a) $\xi = -100$ and (b) $\xi = 100$ (30° station). (Gray) REF and (black) FRC.

on the curved section (c.f. figure 5.16). However, the most important observation is downstream, where localized large-scale regions of high c_f are observed on the curved wall beneath outer large-scale and high-amplitude u'_ξ perturbations.

Close inspection of figure 5.23(i) also provides visual support of faster recovery of the small-scale near-wall structures. For both REF and FRC, the streamwise-aligned near-wall streaks have an intense signature in the wall stress on the flat plate, which is abruptly disrupted near the onset of curvature $\xi \approx 0$. The re-emergence of this signature across the span is clear near the end of the curved wall, $\xi \approx 300$. The key observation, however, is free-stream turbulence re-establishes these streaky structures much earlier upstream on the curve, albeit intermittently, as early as $\xi \approx 50$ for this particular flow realization.

The above empirical observations are quantified, firstly using the normalized two-

point correlation of the wall stress in the span,

$$R_{\tau_w\tau_w}(\xi,\Delta z)=\frac{\overline{\tau_w(\xi,z)\tau_w(\xi,z+\Delta z)}}{\overline{\tau_w(\xi,z)\tau_w(\xi,z)}}. \tag{5.7}$$

Figure 5.24*a* shows that, on the flat section ($\xi=-100$), the wall stress τ_w decorrelates within a fraction of the boundary layer thickness. In contrast, on the curve, the stress is much more correlated in the span, and the correlation length is much wider in presence of free-stream forcing potentially due to the larger size of the outer Görtler motions.

Here we examine whether the wall stress beneath the outer roll motions is indeed statistically large in scale and magnitude, not only in a single realization as shown in figure 5.23 but in a statistically significant fashion. This point is upheld by directly evaluation the average perturbation wall stress,

$$c_f^P(\Delta\xi,\Delta z)=\overline{c_f'(\xi+\Delta\xi,z+\Delta z)\ \mid\ \mathcal{C}^P{}_{|30<\eta^+<\eta_I^+}}\ \text{ and} \tag{5.8}$$

$$c_f^N(\Delta\xi,\Delta z)=\overline{c_f'(\xi+\Delta\xi,z+\Delta z)\ \mid\ \mathcal{C}^N{}_{|30<\eta^+<\eta_I^+}}, \tag{5.9}$$

conditional on the presence of an outer large-scale tangential velocity structure as a surrogate for the Görtler structures. The results are reported in figure 5.25. In both the REF and FRC flows, the peak perturbation stresses are recorded at $\Delta\xi<0$, which is consistent with an inclination of the outer structures relative to the wall. However, in the forced case, the magnitude of perturbations in the wall stress is larger, and the footprint of the outer large scales is greater in extent. In fact, the affected region extends over a longer streamwise distance $\Delta\xi$ (both positive and negative $\Delta\xi$) due

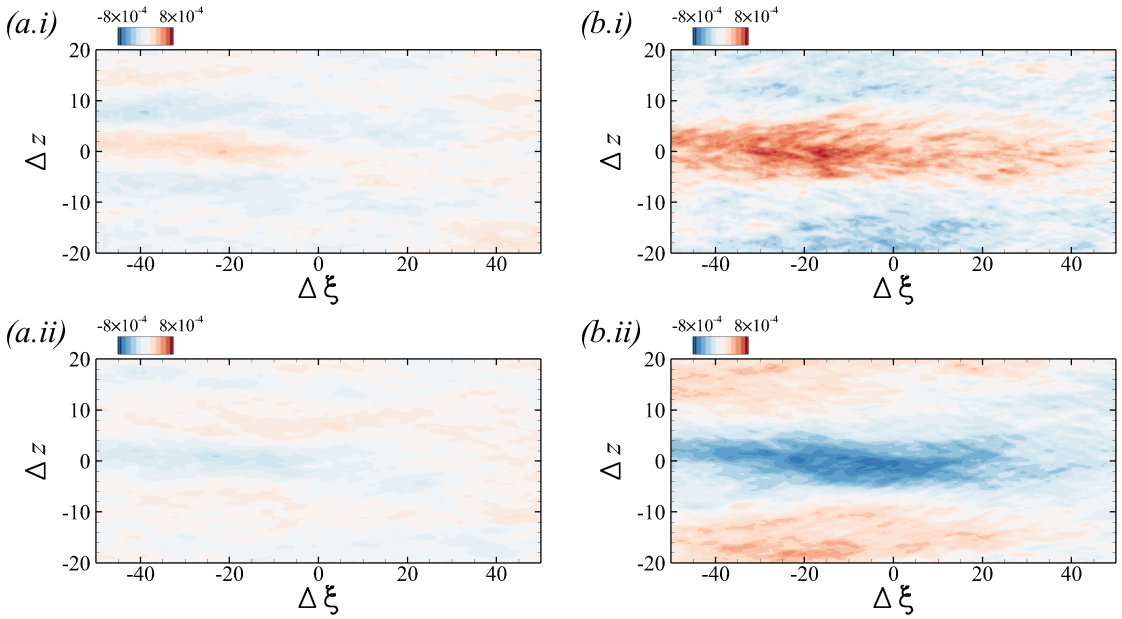

Figure 5.25: Conditionally averaged skin-friction coefficient from (a) REF and (b) FRC at $\xi = 100$ (30° station). (i) $|c_f^P| \leq 8 \times 10^{-4}$ and (ii) $|c_f^N| \leq 8 \times 10^{-4}$.

to the coherence of the outer large scales in this case (c.f. figures 5.17 and 5.18). In addition, the opposite wall stress perturbations are observed in the span which is consistent with the influence of roll motions displacement momentum away and towards the wall at spanwise locations that are separated by their width.

The results presented here provide a structural interpretation of the statistical changes of the boundary layer on the curved surface, without and with free-stream turbulence. While Görtler motions may be elusive in the former case, they are more prominent in the forced flow. Their larger size and strong coherence are evident in the spectra and in conditional averages. They also cause appreciable mixing whereby the near-wall region is directly affected, and the resulting change in the wall stress in

their footprint is therefore significant.

5.5 Conclusion

Direct numerical simulations of turbulent boundary layers on a concave curve without and with free-stream turbulence were contrasted. In the latter case, the inlet turbulence was homogeneous and isotropic with intensity $Tu = 10\%$. The boundary layer and the free-stream turbulence were differentiated using a levelset approach which provides an objective, virtual interface.

In the presence of FST, the skin friction increases up to 49% relative to the reference flow (figure 5.6). Near the onset of the curvature, the drag significantly drops due to the adverse pressure gradient, which induces intermittent flow separation. In this early region, the flow exhibits characteristics of flat-plate APG turbulent boundary layers: decrease in the inner peak of streamwise stress and development of an outer one (figure 5.10). The growth of the outer peak is attributed to the lifting of the near-wall streaks and subsequent formation of Görtler motion on the curved section. The outer peak is more appreciably enhanced in the forced case, since the FST directly influences the outer region of the boundary layer.

The curvature has a clear impact on the wall-normal and spanwise normal stresses, both indicative of the development of Görtler vortices in the outer region (figure 5.9). The wall-normal separation between the peaks of these components of stress increases

with downstream distance, signaling the growth of the vortices as the boundary layer expands (figure 5.10). When the FST is present, the outer roll motions are more energetic and larger is size. In addition, and in contrast to flat-plate boundary layers, introducing FST increases the peak shear-stress correlation coefficient in the curved wall flow (figure 5.13*b*).

Above the curved section, the turbulence structures are significantly modified. The APG near the onset of the curvature disrupts the near-wall streaky structures (figure 5.16). Concurrently, curvature spurs the formation of outer roll motions which increase in size on the concave wall as seen in the conditionally averaged flow fields (figures 5.17 and 5.18). In the forced flow, these longitudinal structures, which we interpret as Görlter vortices, are enlarged in size, strengthened in intensity, display a clear streamwise coherence, and cause efficient wall-normal transport. As a result, the probability of observing free-stream fluid remains finite within the buffer layer (figure 5.21), in contrast to earlier results for flat-plate boundary layers where external turbulence could not reach the buffer layer §3.4. The impact on the near-wall region is direct (figure 5.22), in particular in the wall stress at their footprint (figure 5.25).

5.A Heat transfer over concave curvature

Boundary layers evolve over a heated isothermal curved wall with Prandtl number, $Pr = 0.7$. Figure 5.26*a* shows the evolution of Stanton number, St. Since the wall

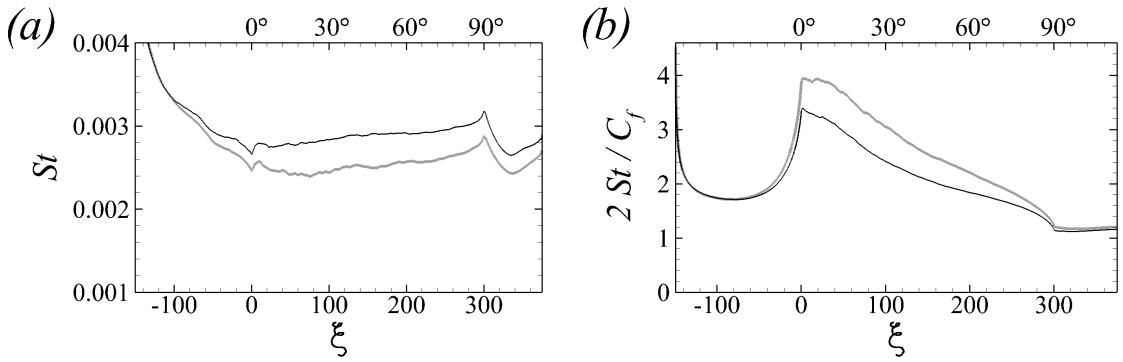

Figure 5.26: Downstream evolution of (a) Stanton number St and (b) Reynolds analogy factor $2St/C_f$. (Gray) REF; (black) FRC.

heating is suddenly applied at the start of the domain, St fastly decays near the inlet. At $\xi = 75$, the rate of heat transfer is increased by 17% in the forced flow relative to the reference case.

In the flat-plate limit (figure 4.3), the Reynolds analogy factor, $2St/C_f$, quickly reaches to the asymptotic state with downstream. On the contrary, the factor is significantly enhanced near the onset of the curvature. Due to the connection between the velocity and pressure through the momentum equation, the skin friction is more affected by the pressure gradient than the heat-transfer rate.

Chapter 6

Conclusion

In the present thesis, spatially evolving turbulent boundary layers beneath the free-stream vortical forcing are investigated using direct numerical simulations. When the boundary layer is subjected to free-stream turbulence, the drag and heat-transfer rate significantly increase. Although many previous studies have reported the increasing rate depending on the intensity and lengthscale of the free-stream turbulence, the internal mechanism remained unclear. In addition, a clear description of contributions of large-scale motions to the turbulent statistics has been unexplored.

The skin-friction coefficient on boundary layers over a flat plate can be interpreted as the power imparted by the wall motion onto the stationary fluid, and is the sum of three contributions: the dissipation due to the established mean-flow profile, the acceleration of the base flow, and the production of turbulent kinetic energy. This analysis showed that the final contribution mainly increases the drag in the forced

flow. In order to differentiate the free-stream and boundary-layer fluids, and then to perform conditional sampling, a level set approach was employed. The free-stream contribution to flow statistics remains finite to greater depth towards the wall when the flow is forced, which is indicative of enhanced mixing. Even though the direct free-stream contribution to the energy vanishes in the near-wall region, the Reynolds shear and normal stresses are enhanced even below the extent of penetration of free-stream perturbations. Thus, the production term increases throughout the buffer layer due to the boundary-layer contribution and leads to the enhancement of skin friction.

This statistical modification is the outcome of changes in the structures within the boundary layer. When the flow is exposed to free-stream forcing, the length scales of the outer boundary-layer structures are increased not only in the streamwise direction but also in the span. Notably, the streamwise extent of the boundary-layer structures is appreciably more extended than the size of the free-stream turbulence, which was demonstrated by the notion of shear sheltering and amplification: Only low-frequency free-stream signals can permeate the boundary layer. The low-frequency free-stream vortical perturbations directly force the boundary layer in the logarithmic layer and lead to the amplification of energetic large-scale motions. These structures modulate the near-wall Reynolds stresses, far below the extent of penetration of free-stream turbulence, and hence drag is increased.

Even though the free-stream turbulence is only vortical and without any ther-

mal disturbances, the heat-transfer rate from the wall also increases relative to the unforced case in the forced boundary layer. The Reynolds stresses enhanced by the free-stream forcing leads to the higher levels of the wall-normal heat flux, which has the dual effect of distorting the mean-scalar profile and also causing an increase in production of scalar variance. Both effects increase the wall heat-transfer rate based on the decomposition of the mean Stanton number. Higher levels of thermal fluctuations accompany the above changes in the forced boundary layer. Notably, the enhanced thermal fluctuations become appreciable throughout the logarithmic layer with downstream, which can be indicative of the formation of outer large-scale thermal structures. These enlarged thermal structures coincide with large-scale streamwise velocity disturbances, and the same roll motions generate both. The outer large-scale velocity motions also modulate the near-wall thermal structures and enhance their amplitude.

Besides the external forcing, the curved surface significantly affects the turbulent structures as well as the flow statistics inside the boundary layer. Due to the complexity of the configuration, the curved-wall boundary layer exposed to the external disturbances has been rarely explored. The present thesis also numerically investigated the forced boundary layers over a concave curvature. The skin friction suddenly drops near the onset of the curvature due to the adverse pressure gradient at the wall. In this region, the inner peak of streamwise stress decreases, and the outer bulge develops. The outer peak is more appreciably enhanced in the forced case since the

free-stream turbulence directly penetrates the outer region of the boundary layer. As the streamwise pressure gradient vanishes with downstream distance, and the flow is mainly subjected to the curvature effect, the mean skin friction increases. The development of the other normal stresses in the outer region is more sensitive to curvature than the streamwise component, which implies the formation of Görtler vortices. The growth of the streamwise vortex tube increases the distance between the maxima of the wall-normal and spanwise stresses. In the presence of the free-stream forcing, the outer roll motions are more enhanced, leading to a further increase in the gap. In the outer region, the roll motions of the forced case make the shear-stress correlation coefficient higher than the value of the reference flow, even though the isotropic free-stream turbulence reduces the coefficient on the flat plate.

Above the curved section, the turbulence structures are significantly modified. Near the onset of the curvature, the adverse-pressure gradient decreases the number of near-wall streaky structures. In the outer region, the roll motions are enhanced in size on the concave curvature in both flows. Thus, the near-wall region is more actively modulated on the curved section relative to the flat plate by the resultant large-scale velocity motions. The free-stream forcing strengthens the Görlter vortices in size and intensity. The enlarged outer roll motions directly send the free-stream turbulence into the buffer layer, which is contrary to the relatively weak penetration in the flat-plate limit and hence induce the even stronger modulation of the near-wall region in the forced case.

Appendix A

Conditional statistics for TKE budget terms

In this appendix, we present relations between the conditional and conventional averages of the pseudo-dissipation and of production of TKE in the Cartesian coordinate. The starting point to derive the expression for the pseudo-dissipation is,

$$\begin{aligned}\overline{\frac{\partial u_i}{\partial x_k}\frac{\partial u_i}{\partial x_k}} &= \gamma\overline{\frac{\partial u_i}{\partial x_k}\frac{\partial u_i}{\partial x_k}}^{B} + (1-\gamma)\overline{\frac{\partial u_i}{\partial x_k}\frac{\partial u_i}{\partial x_k}}^{F} \\ &= \gamma\overline{\frac{\partial u_i^B}{\partial x_k}\frac{\partial u_i^B}{\partial x_k}}^{B} + (1-\gamma)\overline{\frac{\partial u_i^F}{\partial x_k}\frac{\partial u_i^F}{\partial x_k}}^{F} .\end{aligned} \tag{A.1}$$

Using the Reynolds decomposition of each term,

$$\begin{aligned}\overline{\frac{\partial(\overline{u_i}+u_i')}{\partial x_k}\frac{\partial(\overline{u_i}+u_i')}{\partial x_k}} &= \gamma\overline{\frac{\partial(\overline{u_i}^B+u_i^*)}{\partial x_k}\frac{\partial(\overline{u_i}^B+u_i^*)}{\partial x_k}}^{B} \\ &\quad +(1-\gamma)\overline{\frac{\partial(\overline{u_i}^F+u_i'')}{\partial x_k}\frac{\partial(\overline{u_i}^F+u_i'')}{\partial x_k}}^{F} .\end{aligned} \tag{A.2}$$

Recall that conditional averaging does not always commute with the derivative operator (c.f. equation 3.15), and therefore,

$$\begin{aligned}
\frac{\partial \overline{u_i}}{\partial x_k}\frac{\partial \overline{u_i}}{\partial x_k} + \overline{\frac{\partial u_i'}{\partial x_k}\frac{\partial u_i'}{\partial x_k}} &= \gamma\left[\frac{\partial \overline{u_i}^B}{\partial x_k}\frac{\partial \overline{u_i}^B}{\partial x_k} + 2\frac{\partial \overline{u_i}^B}{\partial x_k}\overline{\frac{\partial u_i^*}{\partial x_k}}^B + \overline{\frac{\partial u_i^*}{\partial x_k}\frac{\partial u_i^*}{\partial x_k}}^B\right] \\
&\quad +(1-\gamma)\left[\frac{\partial \overline{u_i}^F}{\partial x_k}\frac{\partial \overline{u_i}^F}{\partial x_k} + 2\frac{\partial \overline{u_i}^F}{\partial x_k}\overline{\frac{\partial u_i''}{\partial x_k}}^F + \overline{\frac{\partial u_i''}{\partial x_k}\frac{\partial u_i''}{\partial x_k}}^F\right] \\
&= \gamma\left[\frac{\partial \overline{u_i}^B}{\partial x_k}\frac{\partial \overline{u_i}^B}{\partial x_k} + 2\frac{\partial \overline{u_i}^B}{\partial x_k}\left(\overline{\frac{\partial u_i}{\partial x_k}}^B - \frac{\partial \overline{u_i}^B}{\partial x_k}\right) + \overline{\frac{\partial u_i^*}{\partial x_k}\frac{\partial u_i^*}{\partial x_k}}^B\right] \\
&\quad +(1-\gamma)\left[\frac{\partial \overline{u_i}^F}{\partial x_k}\frac{\partial \overline{u_i}^F}{\partial x_k} + 2\frac{\partial \overline{u_i}^F}{\partial x_k}\left(\overline{\frac{\partial u_i}{\partial x_k}}^F - \frac{\partial \overline{u_i}^F}{\partial x_k}\right) + \overline{\frac{\partial u_i''}{\partial x_k}\frac{\partial u_i''}{\partial x_k}}^F\right].
\end{aligned} \tag{A.3}$$

The first term on the left-hand side of equation A.3 can be expressed as,

$$\begin{aligned}
\frac{\partial \overline{u_i}}{\partial x_k}\frac{\partial \overline{u_i}}{\partial x_k} &= \frac{\partial(\gamma\overline{u_i}^B + (1-\gamma)\overline{u_i}^F)}{\partial x_k}\frac{\partial(\gamma\overline{u_i}^B + (1-\gamma)\overline{u_i}^F)}{\partial x_k} \\
&= \frac{\partial \gamma\overline{u_i}^B}{\partial x_k}\frac{\partial \gamma\overline{u_i}^B}{\partial x_k} + \frac{\partial(1-\gamma)\overline{u_i}^F}{\partial x_k}\frac{\partial(1-\gamma)\overline{u_i}^F}{\partial x_k} + 2\frac{\partial \gamma\overline{u_i}^B}{\partial x_k}\frac{\partial(1-\gamma)\overline{u_i}^F}{\partial x_k}.
\end{aligned} \tag{A.4}$$

Substitution into equation (A.3) yields,

$$\begin{aligned}
Re\ \varepsilon \equiv \overline{\frac{\partial u_i'}{\partial x_k}\frac{\partial u_i'}{\partial x_k}} &= \gamma\overline{\frac{\partial u_i^*}{\partial x_k}\frac{\partial u_i^*}{\partial x_k}}^B + (1-\gamma)\overline{\frac{\partial u_i''}{\partial x_k}\frac{\partial u_i''}{\partial x_k}}^F \\
&\quad +\gamma\left[2\frac{\partial \overline{u_i}^B}{\partial x_k}\overline{\frac{\partial u_i}{\partial x_k}}^B - \frac{\partial \overline{u_i}^B}{\partial x_k}\frac{\partial \overline{u_i}^B}{\partial x_k}\right] \\
&\quad +(1-\gamma)\left[2\frac{\partial \overline{u_i}^F}{\partial x_k}\overline{\frac{\partial u_i}{\partial x_k}}^F - \frac{\partial \overline{u_i}^F}{\partial x_k}\frac{\partial \overline{u_i}^F}{\partial x_k}\right] \\
&\quad -\frac{\partial \gamma\overline{u_i}^B}{\partial x_k}\frac{\partial \gamma\overline{u_i}^B}{\partial x_k} - \frac{\partial(1-\gamma)\overline{u_i}^F}{\partial x_k}\frac{\partial(1-\gamma)\overline{u_i}^F}{\partial x_k} - 2\frac{\partial \gamma\overline{u_i}^B}{\partial x_k}\frac{\partial(1-\gamma)\overline{u_i}^F}{\partial x_k}
\end{aligned} \tag{A.5}$$

where the first and second terms on the right-hand side are regarded as the boundary-layer and free-stream contributions.

The starting point for deriving the production term is the expression,

$$\begin{aligned}
\overline{(\overline{u_k}+u_k')(\overline{u_i}+u_i')}\frac{\partial \overline{u_i}}{\partial x_k} &= \gamma\overline{(\overline{u_k}^B+u_k^*)(\overline{u_i}^B+u_i^*)}^B\left(\gamma\frac{\partial \overline{u_i}^B}{\partial x_k}+\overline{u_i}^B\frac{\partial \gamma}{\partial x_k}\right) \\
&+ (1-\gamma)\overline{(\overline{u_k}^F+u_k'')(\overline{u_i}^F+u_i'')}^F\left((1-\gamma)\frac{\partial \overline{u_i}^F}{\partial x_k}+\overline{u_i}^F\frac{\partial(1-\gamma)}{\partial x_k}\right) \\
&+ \gamma\overline{(\overline{u_k}^B+u_k^*)(\overline{u_i}^B+u_i^*)}^B\left((1-\gamma)\frac{\partial \overline{u_i}^F}{\partial x_k}+\overline{u_i}^F\frac{\partial(1-\gamma)}{\partial x_k}\right) \\
&+ (1-\gamma)\overline{(\overline{u_k}^F+u_k'')(\overline{u_i}^F+u_i'')}^F\left(\gamma\frac{\partial \overline{u_i}^B}{\partial x_k}+\overline{u_i}^B\frac{\partial \gamma}{\partial x_k}\right).
\end{aligned} \tag{A.6}$$

Using a similar procedure to the pseudo-dissipation, the following relation for $-\mathcal{P}$ is derived,

$$\begin{aligned}
\overline{u_k'u_i'}\frac{\partial \overline{u_i}}{\partial x_k} &= \gamma^2\overline{u_k^*u_i^*}^B\frac{\partial \overline{u_i}^B}{\partial x_k}+(1-\gamma)^2\overline{u_k''u_i''}^F\frac{\partial \overline{u_i}^F}{\partial x_k} \\
&+\gamma^2\overline{u_k}^B\overline{u_i}^B\frac{\partial \overline{u_i}^B}{\partial x_k}+(1-\gamma)^2\overline{u_k}^F\overline{u_i}^F\frac{\partial \overline{u_i}^F}{\partial x_k} \\
&+\gamma(1-\gamma)\left[\overline{u_k}^B\overline{u_i}^B\frac{\partial \overline{u_i}^F}{\partial x_k}+\overline{u_k^*u_i^*}^B\frac{\partial \overline{u_i}^F}{\partial x_k}\right] \\
&+\gamma(1-\gamma)\left[\overline{u_k}^F\overline{u_i}^F\frac{\partial \overline{u_i}^B}{\partial x_k}+\overline{u_k''u_i''}^F\frac{\partial \overline{u_i}^B}{\partial x_k}\right] \\
&+\gamma\left[\overline{u_k}^B\overline{u_i}^B\overline{u_i}^B\frac{\partial \gamma}{\partial x_k}+\overline{u_k^*u_i^*}^B\overline{u_i}^B\frac{\partial \gamma}{\partial x_k}\right] \\
&+(1-\gamma)\left[\overline{u_k}^F\overline{u_i}^F\overline{u_i}^F\frac{\partial(1-\gamma)}{\partial x_k}+\overline{u_k''u_i''}^F\overline{u_i}^F\frac{\partial(1-\gamma)}{\partial x_k}\right] \\
&+\gamma\left[\overline{u_k}^B\overline{u_i}^B\overline{u_i}^F\frac{\partial(1-\gamma)}{\partial x_k}+\overline{u_k^*u_i^*}^B\overline{u_i}^F\frac{\partial(1-\gamma)}{\partial x_k}\right] \\
&+(1-\gamma)\left[\overline{u_k}^F\overline{u_i}^F\overline{u_i}^B\frac{\partial \gamma}{\partial x_k}+\overline{u_k''u_i''}^F\overline{u_i}^B\frac{\partial \gamma}{\partial x_k}\right] \\
&-\{\gamma\overline{u_k}^B+(1-\gamma)\overline{u_k}^F\}\{\gamma\overline{u_i}^B+(1-\gamma)\overline{u_i}^F\}\left\{\frac{\partial}{\partial x_k}\left(\gamma\overline{u_i}^B+(1-\gamma)\overline{u_i}^F\right)\right\}.
\end{aligned} \tag{A.7}$$

Bibliography

[1] R. J. Adrian, C. D. Meinhart, and C. D. Tomkins. Vortex organization in the outer region of the turbulent boundary layers. *J. Fluid Mech.*, 422:1–54, 2000.

[2] F. E. Ames and R. J. Moffat. Heat transfer with high intensity, large scale turbulence: the flat plate turbulent boundary layer and the cylindrical stagnation point. *Stanford University Report*, pages HMT–44, 1990.

[3] S. K. Arolla and P. A. Durbin. LES of spatially developing turbulent boundary layer over a concave surface. *J. Turbul.*, 16(1):81–99, 2015.

[4] P. R. Bandyopadhyay and A. Ahmed. Turbulent boundary layers subjected to multiple curvatures and pressure gradients. *J. Fluid Mech.*, 246:503–527, 1993.

[5] R. S. Barlow and J. P. Johnston. Structure of a turbulent boundary layer on a concave surface. *J. Fluid Mech.*, 191:137–176, 1988a.

[6] R. S. Barlow and J. P. Johnston. Local effects of large-scale eddies on bursting in a concave boundary layer. *J. Fluid Mech.*, 191:177–195, 1988b.

BIBLIOGRAPHY

[7] G. K. Batchelor. *The theory of homogeneous turbulence*. Cambridge University Press, 1953.

[8] G. K. Batchelor and A. A. Townsend. Decay of isotropic turbulence in the initial period. *Proc. R. Soc. A*, 193:539–558, 1948.

[9] M. Bernardini and S. Pirozzoli. Inner/outer layer interactions in turbulent boundary layers: A refined measure for the large-scale amplitude modulation mechanism. *Phys. Fluids*, 23:061701, 2011.

[10] D. K. Bisset, J. C. R. Hunt, and M. M. Rogers. The turbulent/non-turbulent interface bounding a far wake. *J. Fluid Mech.*, 451:383–410, 2002.

[11] M. F. Blair. Influence of free-stream turbulence on turbulent boundary layer heat transfer and mean profile development: Part I. Experimental data. *Trans. ASME: J. Heat Transfer*, 105:33–40, 1983.

[12] G. Borrell. and J. Jiménez. Properties of the turbulent/non-turbulent interface in boundary layers. *J. Fluid Mech.*, 801:554–596, 2016.

[13] P. Bradshaw. Effects of streamline curvature on turbulent flow. *AGARDograph*, 169, 1973.

[14] B. Brzek, S. Torres-Nieves, J. LEBRÓN, R. Cal, C. Meneveau, and L. Castillo. Effects of free-stream turbulence on rough surface turbulent boundary layers. *J. Fluid Mech.*, 635:207–243, 2009.

[15] I. P. Castro. Effects of free-stream turbulence on low Reynolds number boundary layers. *Trans. ASME: J . Fluids Engng*, 106:298–306, 1984.

[16] L. C. Cheung and T. A. Zaki. Linear and nonlinear instability waves in spatially developing two-phase mixing layers. *Phys. Fluids*, 22:052103, 2010.

[17] L. C. Cheung and T. A. Zaki. A nonlinear PSE method for two-fluid shear flows with complex interfacial topology. *J. Comput. Phys.*, 230(17):6756–6777, 2011.

[18] C. B. da Silva, J. C. R. Hunt, I. Eames, and J. Westerweel. Interfacial layers between regions of different turbulence intensity. *Annu. Rev. Fluid Mech.*, 46: 567–590, 2014.

[19] O. Desjardins, V. Moureau, and H. Pitsch. An accurate conservative level set/ghost fluid method for simulating turbulent atomization. *J. Comput. Phys.*, 227:8395–8416, 2008.

[20] E. Dogan, R. E. Hanson, and B. Ganapathisubramani. Interactions of large-scale free-stream turbulence with turbulent boundary layers. *J. Fluid Mech.*, 802:79–107, 2016.

[21] E. Dogan, R. J. Hearst, and B. Ganapathisubramani. Modelling high Reynolds number wall-turbulence interactions in laboratory experiments using large-scale free-stream turbulence. *Phil. Trans. R. Soc. A*, 375(2089):20160091, 2017.

[22] L. Esteban, E. Dogan, E. Rodríguez-López, and B. Ganapathisubramani. Skin-friction measurements in a turbulent boundary layer under the influence of free-stream turbulence. *Exp. Fluids*, 58:115, 2017.

[23] J. M. Floryan. On the Görtler instability of boundary layers. *Progress in Aerospace Sciences*, 28(3):235–271, 1991.

[24] B. Ganapathisubramani, N. Hutchins, W. T. Hambleton, and E. K. Longmire. Investigation of large-scale coherence in a turbulent boundary layer using two-point correlations. *J. Fluid Mech.*, 524:57–80, 2005.

[25] J. C. Gillis and J. P. Johnston. Turbulent boundary-layer flow and structure on a convex wall and its redevelopment on a flat wall. *J. Fluid Mech.*, 135:123–153, 1983.

[26] A. G. Gungor, Y. Maciel, M. P. Simens, and J. Soria. Scaling and statistics of large-defect adverse pressure gradient turbulent boundary layers. *Int. J. Heat Fluid Flow*, 59:109–124, 2016.

[27] F. R. Hama, J. D. Long, and J. C. Hegarty. On transition from laminar to turbulent ow. *J. Appl. Phys.*, 28:388–394, 1957.

[28] P. E. Hancock and P. Bradshaw. The effect of free-stream turbulence on turbulent boundary layers. *Trans. ASME: J. Fluids Engng.*, 105:284–289, 1983.

[29] P. E. Hancock and P. Bradshaw. Turbulence structure of a boundary layer beneath a turbulent free stream. *J. Fluid Mech.*, 205:45–76, 1989.

[30] Z. Harun, J. P. Monty, R. Mathis, and I. Marusic. Pressure gradient effects on the large-scale structure of turbulent boundary layers. *J. Fluid Mech.*, 715: 477–498, 2013.

[31] R. J. Hearst, E. Dogan, and B. Ganapathisubramani. Robust features of a turbulent boundary layer subjected to high-intensity free-stream turbulence. *J. Fluid Mech.*, 851:416–435, 2018.

[32] S. Hickel and N. A. Adams. Implicit LES applied to zero-pressure-gradient and adverse-pressure-gradient boundary layer turbulence. *Int. J. Heat Fluid Flow*, 29:626–639, 2008.

[33] P. H. Hoffmann, K. C. Muck, and P. Bradshaw. The effect of concave surface curvature on turbulent boundary layers. *J. Fluid Mech.*, 161:371–403, 1985.

[34] J. C. R. Hunt and P. A. Durbin. Perturbed vortical layers and shear sheltering. *Fluid Dyn. Res.*, 24(6):375–404, 1999.

[35] N. Hutchins and I. Marusic. Evidence of very long meandering features in the logarithmic region of turbulent boundary layers. *J. Fluid Mech.*, 579:1–28, 2007.

[36] N. Hutchins, W. T. Hambleton, and I. Marusic. Inclined cross-stream stereo

particle image velocimetry measurements in turbulent boundary layers. *J. Fluid Mech.*, 541:21–54, 2005.

[37] J. Hwang, J. Lee, H. J. Sung, and T. A. Zaki. Inner-outer interactions of large-scale structures in turbulent channel flow. *J. Fluid Mech.*, 790:128–157, 2016.

[38] T. Ishida, P. A. Davidson, and Y. Kaneda. On the decay of isotropic turbulence. *J. Fluid Mech.*, 564:455–475, 2006.

[39] T. O. Jelly, S. Y. Jung, and T. A. Zaki. Turbulence and skin friction modification in channel flow with streamwise-aligned superhydrophobic surface texture. *Phys. Fluids*, 26:095102, 2014.

[40] J. Jiménez, S. Hoyas, M. P. Simens, and Y. Mizuno. Turbulent boundary layers and channels at moderate Reynolds numbers. *J. Fluid Mech.*, 657:335–360, 2010.

[41] S. Y. Jung and T. A. Zaki. The effect of a low-viscosity near-wall film on bypass transition in boundary layers. *J. Fluid Mech.*, 772:330–360, 2015.

[42] M. D. Kestoras and T. W. Simon. Effects of free-stream turbulence intensity on a boundary layer recovering from concave curvature effects. *Trans. ASME: Turbomachinery*, 117:240–247, 1995.

[43] M. D. Kestoras and T. W. Simon. Conditionally sampled measurements in a heated turbulent boundary layer: Curvature and free-stream turbulence effects. *Exp. Therm. Fluid Sci.*, 17:63–70, 1998.

[44] K. C. Kim and R. J. Adrian. Very large-scale motion in the outer layer. *Phys. Fluids*, 11:417, 1999.

[45] M. Kozul, R. J. Hearst, J. P. Monty, B. Ganapathisubramani, and D. Chung. Response of the temporal turbulent boundary layer to decaying free-stream turbulence. *J. Fluid Mech.*, 896:A11, 2020.

[46] T. Kurian and J. H. M. Fransson. Grid-generated turbulence revisited. *Fluid Dyn. Res.*, 41:021403, 2009.

[47] J. Lee, S. Y. Jung, H. J. Sung, and T. A. Zaki. Effect of wall heating on turbulent boundary layers with temperature-dependent viscosity. *J. Fluid Mech.*, 726:196–225, 2013.

[48] J. Lee, S. Y. Jung, H. J. Sung, and T. A. Zaki. Turbulent thermal boundary layers with temperature-dependent viscosity. *Int. J. Heat Fluid Flow*, 49:43–52, 2014.

[49] J. Lee, H. J. Sung, and T. A. Zaki. Signature of large-scale motions on turbulent/non-turbulent interface in boundary layers. *J. Fluid Mech.*, 819:165–187, 2017.

[50] Q. Li, P. Schlatter, and D. S. Henningson. Simulations of heat transfer in a boundary layer subject to free-stream turbulence. *J. Turbul.*, 11(45):1–33, 2010.

[51] Q. X. Lian. A visual study of the coherent structure of the turbulent boundary layer in flow with adverse pressure gradient. *J. Fluid Mech.*, 215:101–124, 1990.

[52] M. J. Lighthill. *Boundary Layer Theory.* Oxford University Pres, 1963.

[53] A. S. Lopes, U. Piomelli, and J. M. L. M. Palma. Large-eddy simulation of the flow in an s-duct. *J. Turbul.*, 7(11):1–24, 2006.

[54] T. S. Lund and P. Moin. Large-eddy simulation of a concave wall boundary layer. *Int. J. Heat Fluid Flow*, 17:290–295, 1996.

[55] P. K. Maciejewski and R. J. Moffat. Heat transfer with very high free-stream turbulence. i: Experimental data. *Trans. ASME J. Heat Transfer*, 114:827–833, 1992.

[56] A. C. Mandel and J. Dey. An experimental study of boundary layer transition induced by a cylinder wake. *J. Fluid Mech.*, 684:60–84, 2011.

[57] R. Mathis, N. Hutchins, and I. Marusic. Large-scale amplitude modulation of the small-scale structures in turbulent boundary layers. *J. Fluid Mech.*, 628: 311–337, 2009.

[58] K. C. Muck, P. H. Hoffmann, and P. Bradshaw. The effect of convex surface curvature on turbulent boundary layers. *J. Fluid Mech.*, 161:347–369, 1985.

[59] Y. Na and P. Moin. The structure of wall-pressure fluctuations in turbulent

boundary layers with adverse pressure gradient and separation. *J. Fluid Mech.*, 377:347–373, 1998.

[60] K. Nagata, Y. Sakai, and S. Komori. Effects of small-scale freestream turbulence on turbulent boundary layers with and without thermal convection. *Phys. Fluids*, 23:065111, 2011.

[61] H. M. Nagib, K. A. Chauhan, and P. A. Monkewitz. Approach to an asymptotic state for zero pressure gradient turbulent boundary layers. *Philos. Trans. R. Soc. A Math. Phys. Eng. Sci.*, 365:755–770, 2007.

[62] K. P. Nolan and T. A. Zaki. Conditional sampling of transitional boundary layers in pressure gradients. *J. Fluid Mech.*, 728:306–339, 2013.

[63] R. R. Nourgaliev and T. G. Theofanous. High-fidelity interface tracking in compressible flows: unlimited anchored adaptive level set. *J. Comput. Phys.*, 224: 836–866, 2007.

[64] S. Osher and J. A. Sethian. Fronts propagating with curvature-dependent speed: algorithms based on Hamilton–Jacobi formulations. *J. Comput. Phys.*, 79:12–49, 1988.

[65] V. C. Patel. The effects of curvature on the turbulent boundary layer. *Aeronautical Research Council, London*, page R&M 3599, 1969.

[66] V. C. Patel. Measurements of secondary flow in the boundary layer of a 180

degree curved channel. *Aeronautical Research Council, London*, page ARC CP No. 1043, 1969.

[67] V. C. Patel and F. Sotiropoulos. Longitudinal curvature effects in turbulent boundary layers. *Prog. Aerosp. Sci.*, 33:1–70, 1997.

[68] F. Péneau, H. C. Boisson, and N. Djilali. Large eddy simulation of the influence of high free-stream turbulence on a spatially evolving boundary layer. *Int. J. Heat Fluid Flow*, 21:640–647, 2000.

[69] D. Peng, B. Merriman, S. Osher, H. Zhao, and M. Kang. A PDE-based fast local level set method. *J. Comput. Phys.*, 155(2):410–438, 1999.

[70] S. B. Pope. *Turbulent Flows*. Cambridge University Press, 2000.

[71] N. Renard and S. Deck. A theoretical decomposition of mean skin friction generation into physical phenomena across the boundary layer. *J. Fluid Mech.*, 790: 339–367, 2016.

[72] M. Rosenfeld, D. Kwak, and M. Vinokur. A fractional step solution method for the unsteady incompressible navier-stokes equations in generalized coordinate systems. *J. Comput. Phys.*, 94:102–137, 1991.

[73] W. S. Saric. Görtler vortices. *Annual Review of Fluid Mechanics*, 26(1):379–409, 1994.

[74] P. Schlatter and R. Örlü. Assessment of direct numerical simulation data of turbulent boundary layers. *J. Fluid Mech.*, 659:116–126, 2010.

[75] P. Schlatter and R. Örlü. Turbulent boundary layers at moderate Reynolds numbers: inflow length and tripping effects. *J. Fluid Mech.*, 710:5–34, 2012.

[76] P. Schlatter, Q. Li, G. Brethouwer, A. V. Johansson, and D. S. Henningson. Simulations of spatially evolving turbulent boundary layers up to $Re_\theta = 4300$. *Int. J. Heat Fluid Flow*, 31:251–261, 2010.

[77] N. S. Sharp, S. Neuscamman, and Z. Warhaft. Effects of large-scale free stream turbulence on a turbulent boundary layer. *Phys. Fluids*, 21:095105, 2009.

[78] J. C. Simonich and P. Bradshaw. Effect of free-stream turbulence on heat transfer through a turbulent boundary layer. *Trans. ASME: J. Heat Transfer*, 100:671–677, 1978.

[79] R. M. C. So and G. L. Mellor. Experiment on convex curvature effects in turbulent boundary layers. *J. Fluid Mech.*, 60:43–62, 1973.

[80] K. A. Thole and D. G. Bogard. Enhanced heat transfer and shear stress due to high free-stream turbulence. *Trans. ASME: J. Turbomachinery*, 117:418–424, 1995.

[81] K. A. Thole and D. G. Bogard. High freestream turbulence effects on turbulent boundary layers. *Trans. ASME: J. Fluids Engng*, 118:276–284, 1996.

[82] J. F. Thompson, Z. U. A. Warsi, and C. W. Mastin. *Numerical Grid Generation: Foundations and Applications*. North Holland, 1985.

[83] J. M. Wallace. Quadrant analysis in turbulence research: History and evolution. *Annu. Rev. Fluid Mech.*, 48:131–158, 2016.

[84] J. M. Wallace, R. S. Brodkey, and H. Eckelmann. The wall region in turbulent shear flow. *J. Fluid Mech.*, 54:39–48, 1972.

[85] J. G. Wissink, T. A. Zaki, W. Rodi, and P. A. Durbin. The effect of wake turbulence intensity on transition in a compressor cascade. *Flow, Turbulence and Combustion*, pages 1–22, 2014.

[86] X. Wu, R. G. Jacobs, J. C. R. Hunt, and P. A. Durbin. Simulation of boundary layer transition induced by periodically passing wakes. *J. Fluid Mech.*, 398: 109–153, 1999.

[87] J. You and T. A. Zaki. Conditional statistics and flow structures in turbulent boundary layers buffeted by free-stream disturbances. *J. Fluid Mech.*, 866:526–566, 2019.

[88] T. A. Zaki and P. A. Durbin. Mode interaction and the bypass route to transition. *J. Fluid Mech.*, 531:85–111, 2005.

[89] T. A. Zaki and S. Saha. On shear sheltering and the structure of vortical modes in single- and two-fluid boundary layers. *J. Fluid Mech.*, 626:111–147, 2009.

[90] S. T. Zalesak. Fully multi-dimensional flux-corrected transport algorithms for fluids. *J. Comput. Phys.*, 31:335–362, 1979.

Vita

Jiho You received the B.S. in Mechanical Engineering from Korea University, Seoul, in 2009. After graduation, he served as a military officer in the Republic of Korea Army from 2009 to 2011. In 2013, he earned M.S. in Mechanical Engineering from Carnegie Mellon University. He enrolled in the Mechanical Engineering Ph.D. program at Johns Hopkins University in 2013 and obtained a doctoral degree in 2020. He received a five-year scholarship from the Kwanjeong Educational Foundation during the Ph.D. program, which supports the outstanding students in Korea. His research focuses on the effect of the free-stream turbulence on turbulent boundary layers.